Open Research Online

The Open University's repository of research publications
and other research outputs

The VLT-FLAMES Tarantula Survey XVIII. Classifications and radial velocities of the B-type stars

Journal Item

How to cite:

Evans, C. J.; Kennedy, M. B.; Dufton, P. L.; Howarth, I. D.; Walborn, N. R.; Markova, N.; Clark, J. S.; de Mink, S. E.; de Koter, A.; Dunstall, P. R.; Hénault-Brunet, V.; Maíz Apellániz, J.; McEvoy, C. M.; Sana, H.; Simón-Díaz, S.; Taylor, W. D. and Vink, J. S. (2015). The VLT-FLAMES Tarantula Survey XVIII. Classifications and radial velocities of the B-type stars. Astronomy & Astrophysics, 574, article no. A13.

For guidance on citations see FAQs.

© 2015 ESO

Version: Version of Record

Link(s) to article on publisher's website:
http://dx.doi.org/doi:10.1051/0004-6361/201424414

Copyright and Moral Rights for the articles on this site are retained by the individual authors and/or other copyright owners. For more information on Open Research Online's data policy on reuse of materials please consult the policies page.

oro.open.ac.uk

A&A 574, A13 (2015)
DOI: 10.1051/0004-6361/201424414
© ESO 2015

Astronomy & Astrophysics

The VLT-FLAMES Tarantula Survey

XVIII. Classifications and radial velocities of the B-type stars⋆

C. J. Evans[1], M. B. Kennedy[2], P. L. Dufton[2], I. D. Howarth[3], N. R. Walborn[4], N. Markova[5], J. S. Clark[6], S. E. de Mink[7,8,9,⋆⋆], A. de Koter[7,10], P. R. Dunstall[2], V. Hénault-Brunet[11], J. Maíz Apellániz[12,⋆⋆⋆], C. M. McEvoy[2], H. Sana[13], S. Simón-Díaz[14,15], W. D. Taylor[1], and J. S. Vink[16]

[1] UK Astronomy Technology Centre, Royal Observatory, Blackford Hill, EH9 3HJ, Edinburgh, UK
e-mail: chris.evans@stfc.ac.uk
[2] Department of Physics & Astronomy, Queen's University Belfast, Belfast BT7 1NN, Northern Ireland, UK
[3] Dept. of Physics & Astronomy, University College London, Gower Street, WC1E 6BT, London, UK
[4] Space Telescope Science Institute, 3700 San Martin Drive, Baltimore, MD 21218, USA
[5] Institute of Astronomy with NAO, Bulgarian Academy of Sciences, PO Box 136, 4700 Smoljan, Bulgaria
[6] Department of Physics & Astronomy, The Open University, Walton Hall, Milton Keynes, MK7 6AA, UK
[7] Astronomical Institute Anton Pannekoek, Amsterdam University, Science Park 904, 1098 XH, Amsterdam, The Netherlands
[8] Observatories of the Carnegie Institution for Science, 813 Santa Barbara St., Pasadena, CA 91101, USA
[9] Cahill Center for Astrophysics, California Institute of Technology, Pasadena, CA 91125, USA
[10] Institute voor Sterrenkunde, KU Leuven, Celestijnenlaan 200D, 3001, Leuven, Belgium
[11] Department of Physics, Faculty of Engineering & Physical Sciences, University of Surrey, Guildford, GU2 7XH, UK
[12] Instituto de Astrofísica de Andalucía-CSIC, Glorieta de la Astronomía s/n, 18008 Granada, Spain
[13] ESA/STScI, 3700 San Martin Drive, Baltimore, MD 21218, USA
[14] Instituto de Astrofísica de Canarias, 38200 La Laguna, Tenerife, Spain
[15] Departamento de Astrofísica, Universidad de La Laguna, 38205 La Laguna, Tenerife, Spain
[16] Armagh Observatory, College Hill, Armagh, BT61 9DG, UK

Received 17 June 2014 / Accepted 25 August 2014

ABSTRACT

We present spectral classifications for 438 B-type stars observed as part of the VLT-FLAMES Tarantula Survey (VFTS) in the 30 Doradus region of the Large Magellanic Cloud. Radial velocities are provided for 307 apparently single stars, and for 99 targets with radial-velocity variations which are consistent with them being spectroscopic binaries. We investigate the spatial distribution of the radial velocities across the 30 Dor region, and use the results to identify candidate runaway stars. Excluding potential runaways and members of two older clusters in the survey region (SL 639 and Hodge 301), we determine a systemic velocity for 30 Dor of 271.6 ± 12.2 km s^{-1} from 273 presumed single stars. Employing a 3σ criterion we identify nine candidate runaway stars (2.9% of the single stars with radial-velocity estimates). The projected rotational velocities of the candidate runaways appear to be significantly different to those of the full B-type sample, with a strong preference for either large ($\geq$345 km s^{-1}) or small ($\leq$65 km s^{-1}) rotational velocities. Of the candidate runaways, VFTS 358 (classified B0.5: V) has the largest differential radial velocity (-106.9 ± 16.2 km s^{-1}), and a preliminary atmospheric analysis finds a significantly enriched nitrogen abundance of $12 + \log(\mathrm{N/H}) \gtrsim 8.5$. Combined with a large rotational velocity ($v_e \sin i = 345 \pm 22$ km s^{-1}), this is suggestive of past binary interaction for this star.

Key words. stars: fundamental parameters – stars: early-type – open clusters and associations: individual: NGC 2060 – open clusters and associations: individual: NGC 2070 – open clusters and associations: individual: Hodge 301 – open clusters and associations: individual: SL 639

1. Introduction

The VLT-FLAMES Tarantula Survey (VFTS) is a European Southern Observatory (ESO) Large Programme that has obtained multi-epoch optical spectroscopy of over 800 massive stars in the 30 Doradus region of the Large Magellanic Cloud (LMC). An overview of the survey, including details of the stellar photometry, spectroscopic observations and data reduction, was given by Evans et al. (2011; hereafter Paper I).

The VFTS observations are the first optical spectroscopy for many of the targets, and provide a wealth of new morphological information on the high-mass population of 30 Dor, which will underpin quantitative analyses of the spectra in future papers. Detailed classifications for the 352 O-type spectra (with discussion of notable morphological groups) were presented by Walborn et al. (2014), while classifications for the smaller samples of Wolf–Rayet and late-type stars were given in Paper I. Here we present spectral classifications for 438 B-type objects from the survey. Of these, only 74 (17%) have previously published classifications based on digital data, many of which were obtained at a lower spectral resolving power.

⋆ Table 7 and Appendix A are available in electronic form at http://www.aanda.org
⋆⋆ Einstein Fellow.
⋆⋆⋆ *Current address*: Departamento de Astrofísica, Centro de Astrobiología (INTA-CSIC), Campus ESA, Apartado Postal 78, 28 691 Villanueva de la Cañada, Madrid, Spain.

To complement the spectral classifications, we also present estimates of radial velocities for the B-type sample. These estimates provide insights into the different populations within 30 Dor, and enable identification of candidate runaway stars that have been ejected from their birth sites. In the context of runaway stars, the size of the VFTS sample is unprecedented for a single, young star-forming region. The survey has revealed ~20 O-type runaway candidates (Evans et al. 2010, Sana et al., in prep.), with an apparent connection with rapid rotation (Walborn et al. 2014, Sana et al., in prep.). There are also a number of stars with moderate (projected) rotational velocities in the peripheral regions of 30 Dor, which could perhaps be very rapid rotators (but with low inclinations; see Walborn et al. 2014, for a discussion of their spectra). For completeness, we note that two additional O2-type stars near 30 Dor, Sk−68° 137 and BI 253 (=VFTS 072), were suggested as runaways by Walborn et al. (2002a) on the basis of their remote locations for their apparent youth.

In his pioneering study, Blaauw (1961) noted that the fractional incidence of Galactic runaways is larger among O stars than among B stars, a result substantiated by subsequent authors, and which also emerged in the simulations from Portegies Zwart (2000). In this paper we therefore complement the studies of the O-type runaways in the VFTS with analysis of the B-type stars. In particular, the number and mass spectrum of the ejected runaways from 30 Dor will provide important constraints on models of cluster formation and evolution (e.g. Fujii & Portegies Zwart 2011). The estimated radial velocities presented here, combined with those from the O-type stars (Sana et al. 2013), will also provide an important input for comparisons with theoretical predictions, e.g. in the context of simulations to investigate the initial conditions leading to the distinct clump identified to the north-east of R136 (Sabbi et al. 2012).

In Sect. 2 we summarise the relevant features of the VFTS data and their post-processing. Section 3 sets out the framework within which the spectra were classified and discusses notable objects. Section 4 details the methods we used to estimate radial velocities for each target, followed by a discussion of members of the two oldest clusters in the survey region (Hodge 301 and SL 639) in Sect. 5. Finally, in Sect. 6, we use our velocity estimates to identify candidate single-star and binary runaways and discuss their nature and potential origins. In parallel to this study, Dunstall et al. (in prep.) have exploited the multi-epoch VFTS observations to investigate the multiplicity properties of the B-type sample.

2. Observations and data processing

All of the VFTS data discussed here were obtained using the Medusa–Giraffe mode of the Fibre Large Array Multi-Element Spectrograph (FLAMES) instrument on the Very Large Telescope (VLT). The Medusa fibres (which subtend 1.″2 on the sky) were used to relay light from up to 130 targets simultaneously to the Giraffe spectrograph (see Pasquini et al. 2002).

Full details of the observational strategy and reduction of the data are given in Paper I. In brief, the ESO Common Pipeline Library FLAMES recipes were used to undertake bias subtraction, fibre location, summed extractions of each object, division by a normalised flat-field, and wavelength calibration. Subsequent processing included correction of the spectra to the heliocentric frame, sky subtraction, and rejection of significant cosmic rays.

The Medusa observations used three of the standard Giraffe settings (LR02, LR03, and HR15N), providing spectral coverage of λ3960−5071 Å (at resolving powers, R, of 7000 to 8500), and λ6442−6817 Å (at R = 16 000). These resolutions are greater than for most published standards so, for the purposes of classification, the data were degraded to an effective resolving power of R = 4000, ensuring consistency with the approach to the classification of the O-type stars by Walborn et al. (2014).

For stars that appear to be single (Dunstall et al., in prep.) the LR02 and LR03 spectra were normalised then merged, with the σ-clip levels for cosmic rejection and relative weightings based on the signal-to-noise (S/N) ratios of the individual spectra. Finally, for classification, the merged LR02 and LR03 spectra were combined, then smoothed and rebinned to R = 4000. For stars identified as having significant but relatively modest velocity variations ($\Delta v_r \leq 40$ km s^{-1}), the individual spectra were similarly co-added and degraded (as the variations were within the effective velocity resolution of the rebinned data). For single-lined binaries with $\Delta v_r > 40$ km s^{-1}, the single-epoch LR02 and LR03 spectra with the best S/N ratio were combined and then smoothed/rebinned. We were careful in these cases to ensure that any velocity offsets between features in the small overlap region between the LR02 and LR03 data were not misinterpreted. The small number of double-lined binaries were classified from inspection of the individual spectra.

3. Spectral classification

The spectra were classified by visual comparison to the B-type Galactic standards from Sota et al. (2011) and Sana et al. (in prep.), while also taking into account the effects of the reduced metallicity of the LMC compared to the Galaxy (which can affect the appearance of both the metal and helium absorption lines; e.g. Markova et al. 2009). This was achieved for the luminous, low-gravity objects by interpolating between the available Galactic standards and those for supergiants in the Small Magellanic Cloud (Lennon 1997), and with reference to the framework developed for the LMC by Fitzpatrick (1988, 1991). Classifications of the dwarfs and giants were also informed by comparisons with the standards from Walborn & Fitzpatrick (1990) and the LMC stars classified by Evans et al. (2006).

The primary diagnostic lines are the ionisation ratios of silicon, while also taking into account the appearance of the helium and magnesium (λ4481) lines. For reference, the primary temperature-sequence criteria used to classify the VFTS sample are summarised in Tables 1 and 2 (for supergiants and dwarfs, respectively). Example temperature sequences for supergiants, giants and dwarfs are shown in Figs. A.1−A.3, respectively. At a given spectral type, luminosity classes were assigned from the width of the Balmer lines and (at the earliest types) from the intensity of the silicon absorption lines, while also taking into account the possible effects of rotational broadening on the spectra. Example luminosity sequences for B0.2, B1, and B2.5 types are shown in Figs. A.4−A.6, respectively.

The supergiants and bright giants (i.e. class I and II objects) have rich absorption-line spectra. Given the importance of spectral peculiarities in the context of CNO abundances, and the influence of metallicity effects, these luminous objects were classified independently by three of the authors (CJE, NM, and NRW) with a typical consistency of 0.5 subtypes/luminosity class from the first pass; final types were adopted following discussion of individual objects as required. The larger sample of dwarfs and giants, which exhibited a considerable range in data quality, was classified by CJE. In many instances these classifications are less precise than those possible for the luminous objects, but they

Table 1. Primary temperature-sequence criteria for B-type supergiants.

Type	Criteria
B0	Si IV $\lambda\lambda$4089, 4116 $\gg$ Si III λ4553 > He II λ4542
B0.2	Si IV λ4089 > Si III λ4553 $\gg$ He II λ4542
B0.5	Si IV λ4089 > Si III λ4553; He II λ4542 absent/marginal
B0.7	Si IV λ4089 ~ Si III λ4553; He II λ4686 absent/marginal
B1	Marginal Si IV λ4116; Si III λ4553 > Si IV λ4089
B1.5	Weak/marginal Si IV λ4089, weak Mg II λ4481
B2	Si III λ4553 > Mg II λ4481; Si IV λ4089 absent
B2.5	Si III λ4553 ~ Mg II λ4481; weak Si II $\lambda\lambda$4128-32
B3	Si III λ4553 < Mg II λ4481; Si II $\lambda\lambda$4128-32 present
B5	He I λ4471 > Mg II λ4481; Si II $\lambda\lambda$4128-32 ~ He I λ4121
B8	He I λ4471 ~ Mg II λ4481; Si II $\lambda\lambda$4128-32 ~ He I λ4144
B9	He I λ4471 < Mg II λ4481; Si II $\lambda\lambda$4128-32 > He I λ4144

Notes. Example spectra are shown in Fig. A.1.

Table 2. Primary temperature-sequence criteria for B-type dwarfs.

Type	Criteria
B0	Si IV λ4089 > Si III λ4553> He II λ4542
B0.2	Si IV λ4089 > Si III λ4553; He II λ4542 marginal
B0.5	He II λ4542 absent; Si III λ4116 marginal/absent
B0.7	He II λ4686 marginal/absent; Si III λ4116 marginal/absent
B1	Si III λ4553 > Si IV λ4089; Si IV λ4116, He II λ4686 absent
B1.5	Si IV λ4089 absent; Si III λ4553 ~ Mg II λ4481
B2	Si III λ4553 < Mg II λ4481
B2.5	Si III λ4553 absent; Si II $\lambda\lambda$4128-32 marginal

Notes. Example spectra are shown in Fig. A.3.

should provide sufficient morphological information to enable robust subdivisions of the sample in future analyses.

Each merged spectrum was classified in the framework described above. After initial classification of all the spectra, careful checks were undertaken to ensure self-consistency within the sample. An overlapping sample of ten B0-type stars was classified independently (by NRW) for the study by Walborn et al. (2014), with excellent agreement (to within one luminosity class) in all instances.

The catalogue of classifications and radial-velocity estimates for the B-type objects from the VFTS is presented in Table 7 (available online). For convenience, supplementary information is also provided for each star on its binary status (from Dunstall et al., in prep.), Hα morphology (see Sect. 3.1), optical photometry (from Paper I), alternative identifications used in the literature, and previous spectral classifications.

The S/N ratios of the supergiant spectra were particularly good (typically >100 for both the LR02 and LR03 regions; see Fig. A.1). This allowed us to provide consistent indications of the nitrogen enhancement/deficiency compared to morphologically-normal stars (via Nstr and Nwk qualifiers), as diagnosed from the CNO absorption features in the $\lambda\lambda$4640−4650 region (Walborn 1976). The significant differences in CNO morphology are illustrated by the two B1.5 Ia spectra in Fig. 1. Atmospheric analysis of the supergiants, including estimates of nitrogen abundances and a thorough study of the line-broadening in their spectra, will be presented by McEvoy et al. (2014) and Simón-Díaz et al. (in prep.), respectively.

Given the wide range in quality of the dwarf and giant spectra, we do not comment on CNO morphologies in their classifications. Equally, while we employ the "n" and "(n)" indications

Table 3. Rest wavelengths used to estimate radial velocities (v_r) for the narrow- and broad-lined stars (Sets 1 and 2, respectively).

Ion	λ [Å]	Δ [km s^{-1}]
Set 1		
He I	4120.82	-0.8 ± 6.7
C II	4267.13	1.1 ± 5.1
He I	4437.55	-0.4 ± 5.4
Si III	4552.62	0.3 ± 6.1 (LR02)
		-1.6 ± 5.8 (LR03)
Si III	4567.84	-0.8 ± 6.4
Si III	4574.76	-1.7 ± 7.0
He I	4713.15	2.1 ± 4.5
Set 2		
He I	4009.26	-0.8 ± 11.3
He I	4143.76	0.1 ± 9.0
He I	4387.93	2.7 ± 9.1
He I	4713.15	2.8 ± 7.1
He I	4921.93	-3.5 ± 8.7

Notes. Values in the final column are average differences (Δ) between the velocity estimates for each line and the final velocity for each star. Wavelengths are taken from the NIST atomic spectra database (Kramida et al. 2012); the adopted value for C II is the average of the two stronger transitions.

of broadening (see e.g. Table 3 from Sota et al. 2011) at all luminosity classes, there are likely to be some lacunae (cf. the quantitative $v_e \sin i$ estimates from Dufton et al. 2013).

3.1. Emission-line objects

Where appropriate, spectra were initially classified as "Be+" on the basis of Fe II emission lines in the LR02 and LR03 spectra (see discussion by Evans et al. 2006); the Fe II lines were preferred over the blue-violet Balmer lines owing to the significant (and variable) contamination of the latter by nebular emission.

Independently of the blue-region classifications, we inspected the Hα profiles of every target to investigate their morphologies. The greater resolution of the Hα observations and the extended wings from disc emission made it easier to distinguish contributions from Be-type Balmer emission and nebular contamination than in the blue, but these classifications should still be treated with some caution. The Hα morphologies are encoded in the fourth column of Table 7 (with the notation explained in the corresponding footnote).

Objects classified as "Be+" from the LR02/LR03 spectra were seen to display Hα emission in all cases. Approximately 30 additional stars display Be-like Hα emission without Fe II emission. The Hα emission in luminous supergiants most likely arises from their stellar winds, but for less luminous objects such emission is the primary Be diagnostic. To preserve the distinction of the lines seen in emission, the standard "e" suffix is used in the classifications for the (non-supergiant) stars where only Hα is seen in emission.

The complex star-formation history of 30 Dor means that our sample will span a range of stellar ages, so we are unable to comment on the incidence of the Be-phenomenon for a single, co-eval population. Nonetheless, we note that the incidence of the Be-type classifications for the dwarf and giant stars is 18% (70/388 objects). This is in good agreement with the Galactic fraction (≥17%, Zorec & Briot 1997), and that reported for the field population near NGC 2004 in the LMC (of 16 and 17.5%, from Evans et al. 2006 and Martayan et al. 2006, respectively).

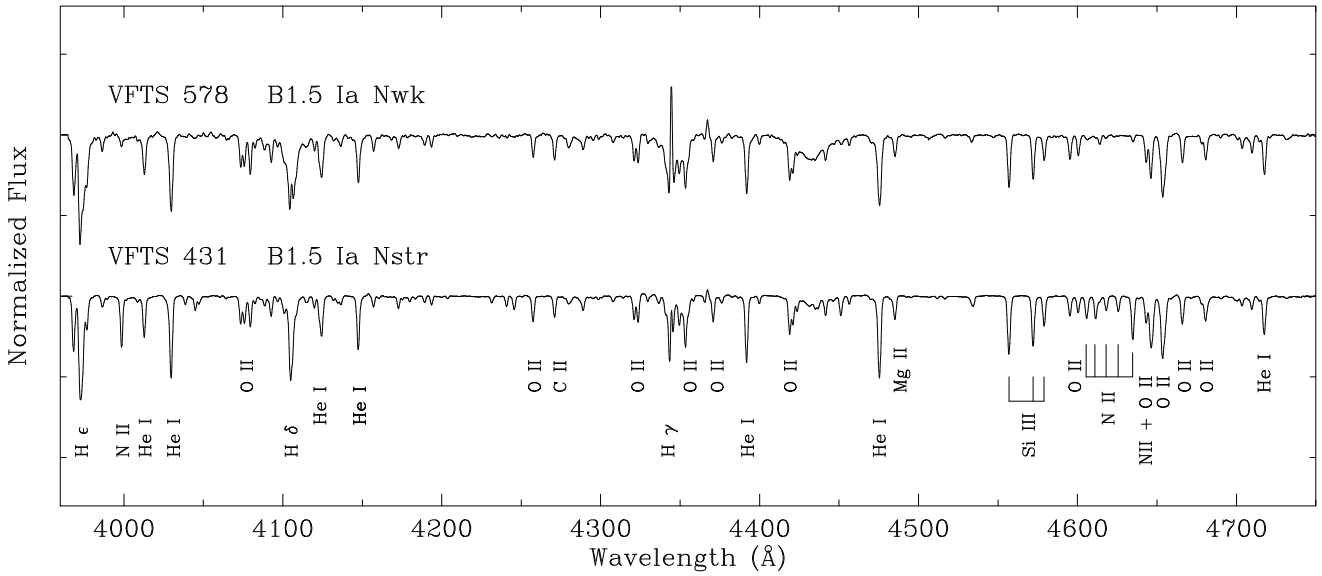

Fig. 1. Differing CNO morphologies in early B-type supergiants illustrated by VFTS 431 ("Nstr") and VFTS 578 ("Nwk"). In addition to the Balmer lines, the absorption features identified are: C II λ4267; He I $\lambda\lambda$4009, 4026, 4121, 4144, 4388, 4471, 4713; Mg II λ4481; N II $\lambda\lambda$3995, 4601-07-14-21-31, 4640-43 (blended with O II); O II $\lambda\lambda$4070, 4254, 4317-19, 4350, 4367, 4414-17, 4591-96, 4650, 4661, 4674-76; Si III $\lambda\lambda$4553-68-74.

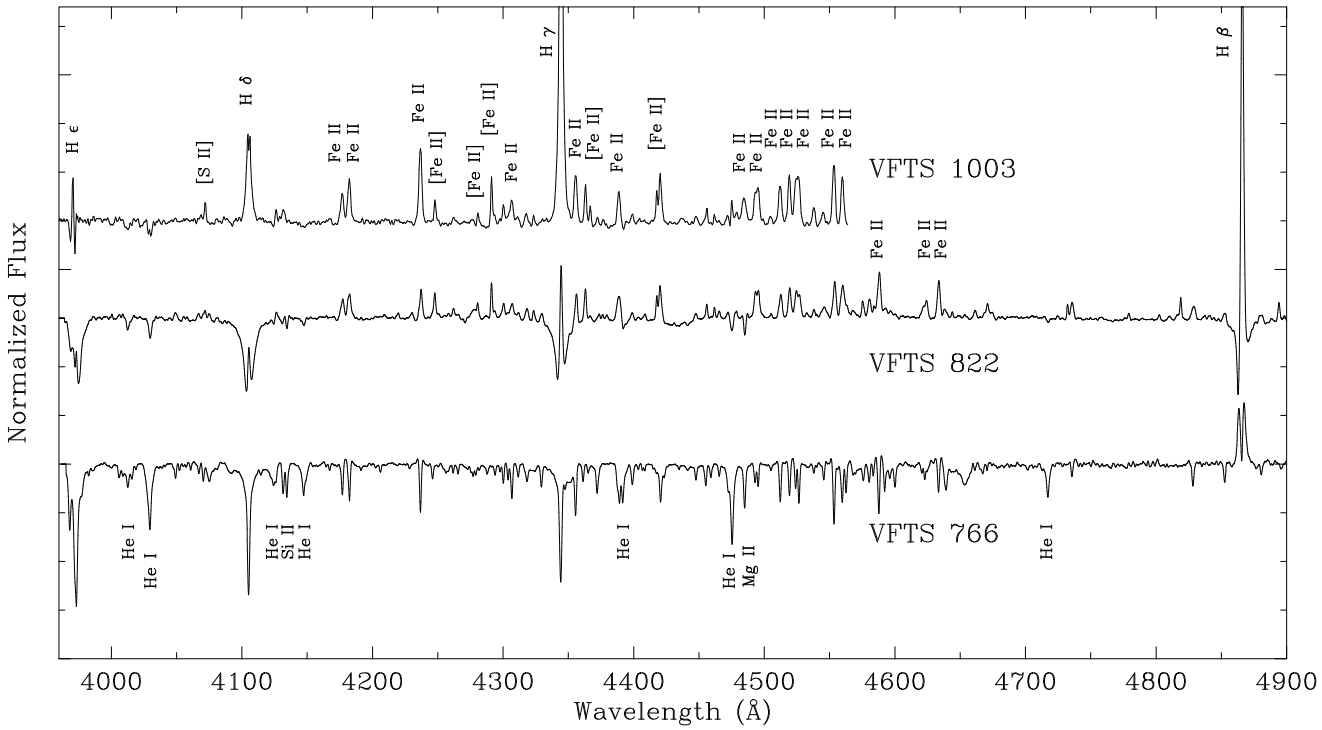

Fig. 2. Spectra of three peculiar Be-type stars from the VFTS, in which each spectrum has been smoothed and rebinned to $R = 4000$ for clarity. In addition to the Balmer lines, the emission lines identified in VFTS 1003 are [S II] λ4069; Fe II $\lambda\lambda$4173, 4179, 4233, 4303, 4352, 4385, 4481, 4491, 4508, 4515, 4520-23, 4549, 4556; [Fe II] $\lambda\lambda$4244, 4277, 4287, 4358-59, 4414-16. Emission lines identified in VFTS 822 are Fe II $\lambda\lambda$4584, 4620.5, 4629. Absorption lines identified in VFTS 766 are He I $\lambda\lambda$4009, 4026, 4121, 4144, 4388, 4471, 4713; Si II $\lambda\lambda$4128-32; Mg II λ4481.

3.1.1. B[e]-type spectra

Two targets in the Medusa–Giraffe sample show forbidden-line emission characteristic of the B[e] category. VFTS 698 is a double-lined binary system with a B[e]-like spectrum, comprising what appears to be an early B-type secondary in orbit around a veiled, more massive companion (see Dunstall et al. 2012). The second B[e] object is VFTS 822, shown in Fig. 2 together with VFTS 1003 (the B[e]-like object from Paper I). Given the intensity of its Si II $\lambda\lambda$4128-32 and Mg II λ4481 absorption, the spectrum of VFTS 822 was classified as mid-late B[e] (~B5-8); further discussion of its possible pre-main-sequence nature was given by Kalari et al. (2014).

Although the nature of VFTS 1003 remains uncertain at present, the number of evolved B[e] stars (at most two) in the VFTS is clearly small compared to the number of normal supergiants. This is in keeping with the small number of sgB[e] stars in Galactic clusters (see the appendix of Clark et al. 2013),

arguing that the B[e] phenomenon in evolved supergiants must be a relatively brief phase or originate from a rare process.

3.1.2. VFTS 766: A peculiar emission-line star

VFTS 766 displays strong Hα emission and inspection of its blue-region spectrum (see Fig. 2) revealed it as a peculiar object. At first glance its spectrum appears to be that of a mid-late B-type supergiant (B5-B8, as traced by e.g. Si II, Mg II), but with superimposed metallic absorption lines, which are consistent with a cooler component. This seemingly composite appearance can indicate a circumstellar shell or disc observed edge-on, and this hypothesis is supported by the twin-peaked Hβ shell-like emission profile. Its near- and mid-IR colours[1] place it in the region in the $J, J-[3.6]$ colour–magnitude diagram which is occupied by early-type stars associated with free-free/bound-free emission, and we find no evidence of hot dust (cf. Bonanos et al. 2009).

Similar emission profiles are observed in some low-luminosity supergiant B[e] stars (e.g. S59, Gummersbach et al. 1995), with examples that also appear to lack dusty discs (Graus et al. 2012, although none have yet been discovered in the edge-on orientation required to yield shell profiles). However, we speculate that VFTS 766 is a classical Be star, in which the twin-peaked emission in the wings of the Balmer profiles gives rise to the supergiant-like appearance. An example of this effect is the development of a circumstellar disc in the classical edge-on Be star o And, which conspires to yield a narrower absorption feature than the underlying photospheric profile (Clark et al. 2003). Another example is provided by the Be star 48 Lib (see Rivinius et al. 2013, and references therein), which has previously been classified as a supergiant (Houk & Smith-Moore 1988).

This possible explanation for the nature of VFTS 766 is supported by its magnitude relative to other stars in our sample. Spectroscopic monitoring to identify an episode of disc loss, during which the (uncontaminated) photospheric Balmer line profiles might be observed, would clarify its luminosity type and true evolutionary status.

3.1.3. Blue hypergiants

We identifed five blue hypergiants (BHGs) in our sample, namely: VFTS 003 (B1 Ia$^+$), 424 (B9 Ia$^+$p), 430 (B0.5 Ia$^+$((n)) Nwk), 458 (B5 Ia$^+$p) and 533 (B1.5 Ia$^+$p Nwk). Recent theoretical and observational studies suggest that early-type BHGs might be massive stars which have passed through a blue supergiant phase and are about to enter a luminous blue variable (LBV) phase (Clark et al. 2012; Groh et al. 2014). This suggests that VFTS 003, 430, and 533 might be on the verge of LBV-like behaviour, although we note that VFTS 430 appears somewhat subluminous compared to the blue supergiants in 30 Dor, and is significantly fainter than VFTS 533 (even accounting for its apparently greater line-of-sight extinction, see photometry in Table 7). Later-type BHGs have been observed to undergo LBV-like photometric and spectroscopic behaviour (e.g. Smith et al. 2004; Clark et al. 2012, with potential implications for VFTS 424 and 458 here), suggesting that these two evolutionary phases are essentially synonymous for such stars.

On further inspection of their spectra, broad emission wings were identified in the Hβ profiles of each of the BHGs, except for VFTS 430. This Hβ morphology is seen in some LBVs and other luminous supergiants (e.g. Walborn & Fitzpatrick 2000), and is also present in VFTS 739 in our sample (classified as A0 Ip but, given its omission from Paper I, included here in the B-type sample). The spectra and evolutionary status of these potential LBV precursors/candidates will be discussed in more depth by Walborn et al. (in prep.).

3.1.4. Comparisons with X-ray observations

We compared our sample with the point-source detections from observations in 30 Dor with the *Chandra* X-ray Observatory (Townsley et al. 2006, 2014); none of the VFTS B-type stars is detected in the extant X-ray data. A new X-ray Visionary Project is now underway, "The Tarantula Revealed by X-rays (T-ReX)", which will observe 30 Dor with *Chandra* for 2 Ms. This will push far deeper than the existing data, and we will revisit the VFTS sample once the T-ReX observations and analysis are complete.

4. Stellar radial velocities

4.1. Single stars

Radial-velocity estimates for the stars identified as apparently single by Dunstall et al. (in prep.) were obtained from Gaussian fits to selected absorption lines in the merged LR02 and LR03 spectra of each object (at the native resolution of the data, without the degrading applied for classification purposes). This approach is consistent with that used by Sana et al. (2013) for analysis of the O-type stars, albeit (necessarily) using a different subset of absorption lines. We note that the choice of Gaussian profiles may not be appropriate for fitting the wings of the lines in the presence of different broadening mechanisms, but they should suffice for robust estimates of the centres of our chosen lines.

We also considered a cross-correlation method to estimate the radial velocities. However, given the range in temperature and luminosity of the sample, as well as the varying data quality and problems of nebular contamination, the selection of suitable template spectra for cross-correlation was not trivial and would have introduced additional uncertainties (relating to e.g. the projected rotational velocities, $v_e \sin i$). Thus, we did not pursue this approach further.

4.1.1. Line selection

The large range in $v_e \sin i$ and effective temperature for the sample meant that it was not possible to use a single set of diagnostic lines for all stars. Moreover, the large intrinsic width and nebular contamination of the Balmer lines precluded their use; similarly, nebular emission affects some of the stronger He I lines. Following the approach taken by Dufton et al. (2013), we used different sets of diagnostic lines (as summarised in Table 3) depending on the $v_e \sin i$ of the star.

For narrow-lined spectra (defined as $v_e \sin i \lesssim 150\,\mathrm{km\,s^{-1}}$), we used three non-diffuse He I lines and four isolated metal lines listed as "Set 1" in Table 3. Where possible, radial velocities were estimated from Si III λ4553 in both the merged LR02 and LR03 spectra, giving up to eight individual estimates for the narrow-lined objects.

We note that He I λ4121 is potentially affected by blending with O II $\lambda\lambda$4120.28/54. In many instances these features could be resolved and a double Gaussian profile was fitted to estimate the He I and O II line centres; in cases where the O II lines

[1] VFTS 766: $J = 15.14$, $H = 15.01$, $K_s = 14.76$ (from Paper I); [3.6] = 14.28, [4.5] = 14.06, [5.8] = 13.64 (from Meixner et al. 2006).

were weaker or unresolved, they do not appear to have unduly influenced the results (see Table 3, in which the residual for He I λ4121 is consistent with the other lines).

Radial-velocity estimates for stars with broader lines were more difficult, particularly for spectra with significant nebular contamination. In these cases, velocities were estimated by fitting the five He I lines listed as "Set 2" in Table 3, for which the profiles are expected to be effectively symmetric[2].

Representative examples are shown in Fig. 3. The lower panel shows fits to the Si III triplet for two narrow-lined stars, VFTS 053 and 159, which have $v_e \sin i \leq 40$ (i.e. less than the velocity resolution of the data) and 96 ± 9 km s^{-1}, respectively (from Dufton et al. 2013). As an example of a spectrum of a rapidly-rotating star which also suffers nebular contamination, the upper panel of Fig. 3 shows the Gaussian fit to He I λ4388 for VFTS 636 ($v_e \sin i = 371 \pm 35$ km s^{-1}; Dufton et al. 2013).

For three stars with later/peculiar types – VFTS 272 (possible shell star), 739 (A0 Ip), and 766 (B5-8e, see Sect. 3.1.2) – we employed weak Fe II and Ti II absorption lines to estimate velocities, although we note that in VFTS 272 and 766 they might not be representative of the true (stellar) radial velocity, as these lines could trace cooler features associated with a disc of material (see e.g. the discussion of VFTS 698 by Dunstall et al. 2012).

4.1.2. Mean velocities

Radial-velocity estimates for the single stars were obtained by calculating an average of the n individual measurements (v_i), weighted by the estimated central depth (d_i) from the Gaussian fit of each line, i.e.

$$v_r = \frac{\sum_{i=1}^{n} v_i d_i}{\sum_{i=1}^{n} d_i}. \quad (1)$$

The sample standard deviation (σ) for each star was similarly calculated as a weighted average:

$$\sigma^2 = \frac{\sum_{i=1}^{n} (v_i - v_r)^2 d_i}{\sum_{i=1}^{n} d_i}. \quad (2)$$

In cases where the central depths of the absorption lines were less than twice the inverse of the continuum S/N ratio, the individual estimates were excluded from the above calculations (to avoid their larger uncertainties degrading the results from stronger lines). For stars with estimates from three (or more) absorption lines, we present their estimated mean velocities and standard deviations in Cols. 7 and 8 of Table 7. For completeness, the line-by-line estimates from Sets 1 and 2 for the single stars are detailed in Tables A.1 and A.2, respectively; the mean uncertainty of the estimates for the 307 (presumed) single stars is 7.8 km s^{-1} (and with a median uncertainty of 6.2 km s^{-1}).

As a check on our results, we used the methods described above to analyse a sample of the late O-type stars from the VFTS, finding excellent agreement between our velocity estimates and those from Sana et al. (2013, see discussion in Sect. A.2.1). We also investigated the internal consistency of our results from the selected lines by calculating the average difference (Δ) of the individual measurements for each line compared to the adopted mean velocity for each target. The means and standard deviations of these differences are given in Col. 3 of Table 3, with no significant shifts seen for any of the diagnostic lines compared to the adopted radial velocities.

[2] He I ^{3}P $\rightarrow$ ^{3}D transitions were excluded because of the presence of significant ^{3}P $\rightarrow$ ^{3}F components.

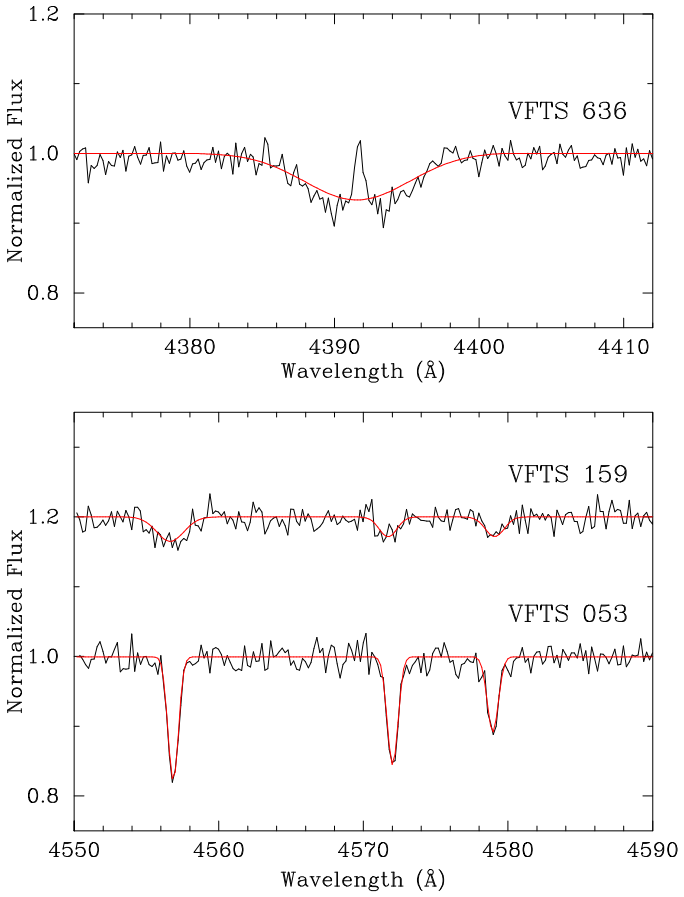

Fig. 3. Examples of Gaussian fits used to estimate radial velocities (v_r) for the B-type sample. *Upper panel*: fit to He I λ4388 in a rapidly-rotating object (VFTS 636) with nebular contamination. *Lower panel*: fits to the Si III triplets ($\lambda\lambda$4553-68-74) of VFTS 053 and 159.

4.2. Radial velocities of the binaries

To complement the analysis of the single stars, we also investigated the radial velocities of the single-lined binaries in the sample. We obtained single-epoch velocity estimates ($v_{\rm single}$) for each system using measurements from the best LR02 spectra (in terms of S/N ratio of the co-added exposures from a given night, which span three hours at most).

Given the reduced spectral coverage of the LR02 data compared to the full LR02 + LR03 range, we used all of the available lines from Table 3 to estimate $v_{\rm single}$ (except for He I λ4121, given the nearby O II feature and the lower S/N ratio of the single-epoch spectra compared to the quality of the co-added spectra of the single stars). Line-by-line estimates and the date for which they were measured are listed in Table A.3. Mean velocities and standard deviations for the selected epoch were then estimated using the same methods as for the single stars.

The mean single-epoch velocities serve as an absolute reference point for the inter-epoch differential velocities calculated by Dunstall et al. (in prep.) yielding absolute estimates for each epoch. We then calculated the mean and standard deviation of the multi-epoch estimates to obtain a velocity estimate for each single-lined binary. These values are presented in Table 7, and are flagged as "B" (binary) in the ninth column. We note that the typical uncertainty on the cross-correlation results from Dunstall et al. was less than 5 km s^{-1}, while the typical error on the absolute estimates determined here from the single-epoch data was

9 km s^{-1}; i.e. the uncertainties in our estimates will generally be dominated by the analysis presented here.

Full orbital solutions are presently unavailable for the B-type binaries, so we strongly caution the reader that the velocity estimates in Table 7 are not their centre-of-mass, systemic velocities (although, as discussed in the Appendix, in many instances they may provide reasonable estimates).

4.3. Spatial distribution

In addition to NGC 2070 (the main 30 Dor cluster, which includes R136 at its core) and NGC 2060 (the association to the south-west), there are two smaller clusters in the VFTS survey: Hodge 301 (Hodge 1988) and SL 693 (Shapley & Lindsay 1963); their relative locations are shown in Fig. 4. Both clusters appear older than NGC 2060 and 2070 as they contain evolved supergiants, from B- through to M-types.

We calculated weighted mean velocities ($\overline{v_r}$, and their standard deviations) for the full sample of single stars, for the subsamples associated with the four distinct stellar assocations in the survey region (NGC 2060, NGC 2070, Hodge 301, and SL 639, as defined in Table 4), and for the field population of stars outside the four clusters. These results, which exclude candidate runaway stars (see Sect. 6), are summarised in Table 4.

The results for the two younger star-forming regions (i.e. NGC 2060 and 2070) are in excellent agreement with the field population of B-type stars in the region, but the two older clusters (Hodge 301 and SL 639) appear at slightly lower recession velocities, suggesting that they are kinematically distinct from the rest of the sample. The weighted mean velocity for the 273 single stars excluding these two clusters (and potential runaways) is $\overline{v_r} = 271.6 \pm 12.2$ km s^{-1}.

5. Spectral content of the older clusters

The VFTS data comprise the first comprehensive spectroscopy in Hodge 301 and SL 639, so we briefly discuss these clusters in turn.

5.1. Hodge 301

There are 20 VFTS targets within a 20″ radius (chosen to conservatively identify likely members, and corresponding to ~4.9 pc, assuming a distance modulus of 18.5 mag). Fifteen of these were classified as B-type and their likely membership of the cluster is indicated in the final column of Table 7[3].

From analysis of *Hubble* Space Telescope (HST) imaging, Grebel & Chu (2000) estimated Hodge 301 to be 20–25 Myr old. From narrow-band imaging they also identified 19 Be-type stars, eight of which (VFTS 272, 276, 279, 282, 283, 287, 293, and 301) have spectroscopy from the VFTS. The Hα spectra of each of these contain significant nebular emission (with multiple components in all sightlines except towards VFTS 293). Nonetheless, broad Be-like Hα emission is present in each object, except for VFTS 276 (GC00-Be2).

Grebel & Chu (2000) noted two potential blue stragglers in the cluster, which they argued were too luminous for the main-sequence population (but less luminous than expected for supergiants). The first, VFTS 270 (WB97-2), is a seemingly unremarkable B3 Ib star. The second is VFTS 293 (WB97-9, GC00-Be1), classified here as B2 III-II(n)e. From two previous observations, Walborn & Blades (1997) noted small shifts of its absorption features (relative to superimposed nebular emission) and possible weak He II λ4686 emission at one epoch. If the He II emission were real, Walborn & Blades speculated that it might be an X-ray binary. There is no evidence of λ4686 emission in the LR03 FLAMES spectra (albeit all taken on the same night, see Paper I), but small line-profile variations are seen in the absorption features in the multi-epoch LR02 spectra.

More intriguing is VFTS 310 on the periphery of the cluster and classified as O9.7 V: (Walborn et al. 2014). With such a classification, VFTS 310 would be expected to be significantly younger than the other cluster members, as shown by its location in the Hertzsprung-Russell (H-R) diagram of the cluster (Fig. 5, see Sect. 5.3 for details). The star appears otherwise unremarkable, with a low projected rotational velocity ($v_e \sin i \leq 40$ km s^{-1}, Dufton et al. 2013) and a radial velocity ($v_r = 272.3 \pm 2.8$ km s^{-1}, Sana et al. 2013) which is consistent with those in NGC 2070 and the local field population. Moreover, it does not appear to be a runaway from Hodge 301 (see Sect. 6). Whether this is a true blue straggler or simply a line-of-sight coincidence remains uncertain at this time.

5.2. SL 639

Adopting a 20″ radius (~4.9 pc), sixteen of the VFTS targets are within SL 693. Fourteen are in the B-type sample, with their membership of SL 639 indicated in the final column of Table 7[4]. Ten of these stars are early-B dwarfs/giants, with six of them displaying Be-like Hα emission. The remaining four are comprised of two supergiants (VFTS 827, B1.5 Ib; VFTS 831, B5 Ia) and two bright giants (VFTS 826, B1 IIn; VFTS 829, B1.5-2 II).

There are previous age estimates for SL 693. From consideration of its main-sequence turn-off, Hodge (1983) estimated its age to be 18 Myr (although he noted a large uncertainty compared to the theoretical models of the time). A larger estimate of 30 Myr was given by Santos et al. (1995) from its reddening-corrected, integrated $(U - B)_0$ colour and adopting an empirical calibration of colour vs. age from Bica et al. (1990).

5.3. H-R diagram

Motivated by the apparent similarities of the two clusters in terms of their spectral content, we constructed an H-R diagram in order to compare the properties of their likely members. Ahead of detailed quantitative analysis of the VFTS spectra and pending extinction analysis of the whole sample, we adopted effective temperatures ($T_{\rm eff}$) on the basis of the spectral types in Table 3 using the calibrations of Trundle et al. (2007), and interpolating between the Galactic and SMC temperatures for A-type supergiants from Evans & Howarth (2003); cooler objects were omitted given the larger uncertainties in their spectral classifications. Stellar luminosities were estimated using the optical photometry from Paper I, intrinsic colours from Fitzgerald (1970), bolometric corrections from Balona (1994), and assuming $R_V = 3.5$ (see Appendix C of Doran et al. 2013).

[3] The five others are: VFTS 310 (O9.7 V: Walborn et al. 2014) and VFTS 271, 281, 289, and 294 (A7 II, Mid-late K, Late G/Early K, and A0 Ib, respectively, from Paper I). Three additional stars (VFTS 263, 291, and 317) are also nearby, at radii from the adopted centre of ~25″.

[4] The two others are VFTS 820 and 828 (A0 Ia and Early M, respectively, from Paper I). The only other VFTS target within a 35″ (8.5 pc) radius is VFTS 839 at ~25″ (6 pc), classified as G-type in Paper I. All three of these cooler objects have radial velocities consistent with membership of the LMC.

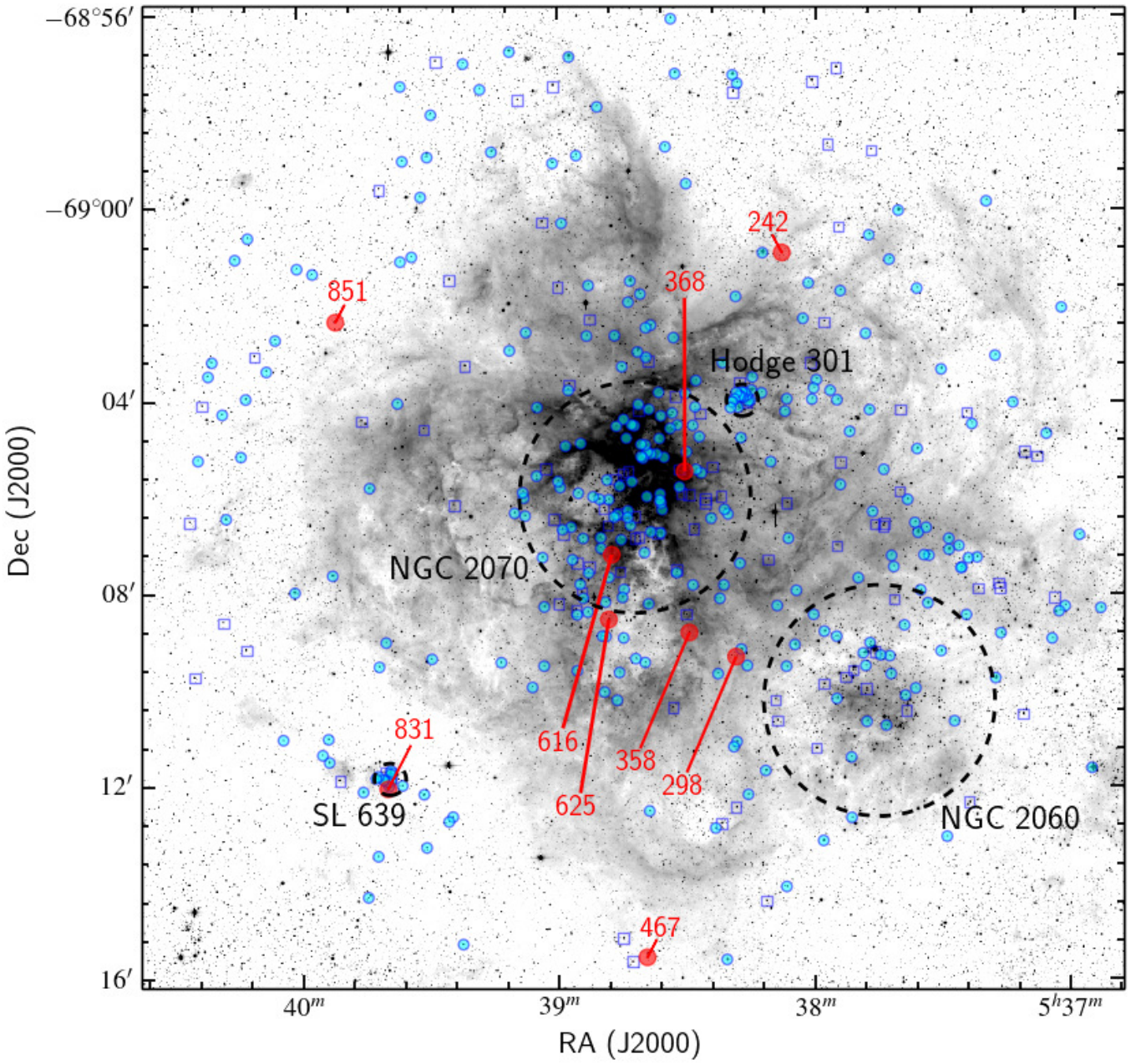

Fig. 4. Spatial distribution of the B-type single stars (cyan circles) and spectroscopic binaries (open blue squares) with radial-velocity estimates; the nine candidate runaways, labelled by their VFTS identifiers, are marked in red. The spatial extents of NGC 2070, NGC 2060, SL 639, and Hodge 301 (as defined in Table 4), are indicated by the overlaid dashed circles. The underlying image is from a *V*-band mosaic taken with ESO's Wide Field Imager on the 2.2 m telescope at La Silla.

The H-R diagram is shown in Fig. 5, with SL 639 and Hodge 301 members indicated by the filled black and open red circles, respectively. Evolutionary tracks and isochrones (for non-rotating models) from Brott et al. (2011) are also plotted for comparison. As noted earlier, the late O-type star in Hodge 301, VFTS 310, stands out as a blue straggler with $T_{\rm eff} > 30$ kK.

Tailored atmospheric and extinction analyses of these objects should help to provide further insight in due course. Nonetheless, the stars in SL 639 appear marginally younger than those in Hodge 301. From qualitative comparison with the isochrones, we estimate an age in the range of 10–15 Myr for SL 639, significantly younger than the estimate of 30 Myr from Santos et al. (1995). There is a larger spread in the inferred ages for the stars in Hodge 301 of 15 ± 5 Myr, overlapping with the lower estimate of 20 Myr from the photometric study of Grebel & Chu (2000). Adopting isochrones calculated for the rotating models from Brott et al. had little impact on these results; e.g. assuming an intial rotational velocity of 301 km s^{-1}, the inferred ages were only marginally younger (by ∼1 Myr).

6. Candidate runaways

6.1. Single stars

To identify candidate runaways in the B-type sample we compared the radial-velocity estimates for each star with the initial weighted mean and standard deviation calculated for the stars in NGC 2060, NGC 2070, and the surrounding field population

Table 4. Mean radial velocities ($\overline{v_r}$) and standard deviations (σ) of the stellar associations identified within 30 Doradus.

Region	No. of stars	Radius [′]	α [J2000.0]	δ [J2000.0]	$\overline{v_r} \pm \sigma$
All	298	...	...	...	270.4 ± 12.4
NGC 2070	78	2.40	05 38 42.0	−69 06 02.0	271.2 ± 12.4
NGC 2060	22	2.40	05 37 45.0	−69 10 15.0	273.7 ± 13.4
Hodge 301	14	0.33	05 38 17.0	−69 04 01.0	261.8 ± 5.5
SL 639	11	0.33	05 39 39.4	−69 11 52.1	253.5 ± 3.9
Field	173	...	...	...	271.3 ± 11.8
All (excl. H 301/SL 639)	273	...	...	...	271.6 ± 12.2

Notes. These statistics exclude the nine candidate runaways identified in Table 5. For consistency, the central positions adopted for NGC 2060 and NGC 2070 are those used by Sana et al. (2013). Approximate centres for Hodge 301 and SL 639 were adopted using the coordinates of WB97-5 (Walborn & Blades 1997) and VFTS 828, respectively.

Table 5. Candidate runaway stars identified from the radial-velocity analysis of the VFTS B-type spectra.

VFTS	Classification	v_r [km s^{-1}]	$(v_r - \overline{v}_r)$ [km s^{-1}]	$\lvert v_r - \overline{v}_r \rvert / \sigma$	$v_e \sin i$ [km s^{-1}]	r_d [′]	r_d [pc]
242	B0 V-IV	216.0 ± 3.6	−55.6 ± 12.7	4.6	≤40	5.96	86.6
298	B1-2 V-IIIe+	332.1 ± 4.0	60.5 ± 12.8	5.0	431 ± 15	3.92	57.1
358	B0.5: V	164.7 ± 10.7	−106.9 ± 16.2	8.8	345 ± 22	3.02	44.0
368	B1-3 V	229.6 ± 12.4	−42.0 ± 17.4	3.4	380:	1.20	17.5
467	B1-2 Ve+	322.3 ± 30.2	50.7 ± 32.6	4.2	355 ± 29	9.54	138.7
616	B0.5: V	227.4 ± 10.7	−44.2 ± 16.2	3.6	≤40	1.26	18.3
625	B1.5 V	310.7 ± 9.2	39.1 ± 15.3	3.2	64 ± 12	2.57	37.4
831	B5 Ia	210.4 ± 6.2	−61.2 ± 13.7	5.0	41	7.91	115.0
851	B2 III	229.4 ± 0.3	−42.2 ± 12.2	3.5	≤40	7.18	104.4

Notes. Estimates of $v_e \sin i$ are from Dufton et al. (2013) except for VFTS 831, which is taken from McEvoy et al. (2014). Projected distances from the core of R136 are from Paper I.

(i.e. excluding Hodge 301 and SL 639). Employing a threshold of $|\delta v_r| > 3\sigma$ we identified eight candidate runaways and then recalculated the mean velocities (and dispersions) excluding these objects. Reapplying a 3σ threshold provided one additional candidate, while a second iteration did not reduce the velocity dispersion further. The mean velocities and dispersions for the different spatial samples (excluding potential runaways) are presented in Table 4. The cumulative distribution of the velocity estimates for the 307 single stars is shown in Fig. 6, with the $\pm 3\sigma$ threshold (i.e. ± 36.6 km s^{-1}) for identification of runaway stars indicated by the vertical dotted lines.

Our adopted velocity threshold is comparable in magnitude to the limit used by Blaauw (1961), which was that candidate runaways have a *space velocity* which differs by more than 40 km s^{-1} from the systemic velocity of the region in which they formed. (In this context, our radial-velocity estimates should serve as lower limits to the 3D space velocities.) In contrast, Portegies Zwart (2000) adopted a lower threshold of 25 km s^{-1} in his theoretical study of the origins and characteristics of runaways. Given the limitations of the B-type data and the relatively small number of lines available for some objects, we did not consider a comparably low threshold.

Details of the nine candidate runaways are summarised in Table 5, and their locations are shown in Fig. 4. Four of the candidates have differential velocities in the range of $3.2-3.6\sigma$, thus their status as candidates will depend strongly on the adopted velocity criteria. Moreover, our adopted velocity threshold (the dispersion of the weighted mean velocities in the sample) was employed without consideration of the uncertainty on the radial-velocity estimate for a given star. Thus, VFTS 467, although formally with a radial velocity of 4.2σ from the systemic value, has a large uncertainty on its estimated velocity. Indeed, only three He I lines were available for this star and the λ4144 estimate (277.5 km s^{-1}) is comparable to the systemic value.

The choice to use weighted means to investigate the spatially-different samples in Sect. 4.3 was motivated by the fact that approximately 10% of our velocity estimates have uncertainties of ≥15 km s^{-1} (each of which is a broad-lined star, i.e. used the Set 2 lines from Table 3). To investigate the dependence of the number and identity of the candidate runaways on these adopted means, we repeated the above steps for both the (unweighted) mean and median velocities of the sample. The mean velocity for the 281 stars (not including those in Hodge 301 and SL 639) was 269.8 = 16.4 km s^{-1}, with a median value of 270.7 km s^{-1}. Adopting either of these systemic values and a 3σ threshold (taking the dispersion as 16.4 km s^{-1}) led to identification of the five most significant runaways from Table 5 (i.e. VFTS 242, 298, 358, 467, and 831), with a second iteration providing one additional candidate (VFTS 616). The final mean velocity from these calculations is 270.1 ± 13.9, in good agreement with the equivalent subsample in the final row of Table 4. From these checks we conclude that the four most significant candidates (VFTS 242, 298, 358, and 831) are secure as potential runaways, with five more tenative candidates as discussed above.

For the members of Hodge 301, VFTS 309 is a potential outlier (at 3.6σ) compared to the mean velocity for the cluster in Table 4. Indeed, excluding its v_r estimate from the calculated mean and dispersion for Hodge 301 gives $\overline{v_r} = 261.5 \pm 5.0$ km s^{-1}, such that VFTS 309 is then a 4.1σ outlier. However, its velocity is also in reasonable agreement with

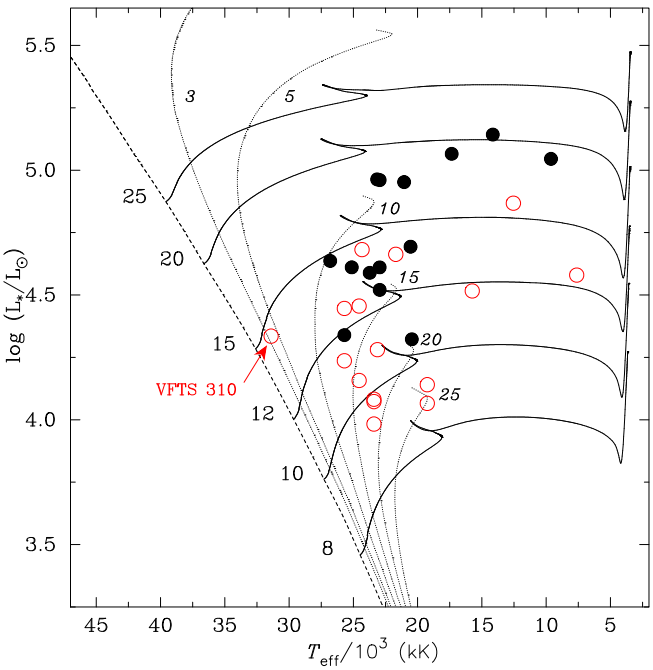

Fig. 5. Hertzsprung-Russell diagram for the VFTS objects observed in SL 639 (black circles) and Hodge 301 (red, open circles). Also plotted are evolutionary tracks for initial masses of 8, 10, 12, 15, 20, 25 $M_{\odot}$ (solid lines), the zero-age main sequence (dashed line), and isochrones (3, 5, 10, 15, 20, and 25 Myr, dotted lines) for the non-rotating models from Brott et al. (2011). The apparent blue straggler in Hodge 301 (VFTS 310) is a late O-type star.

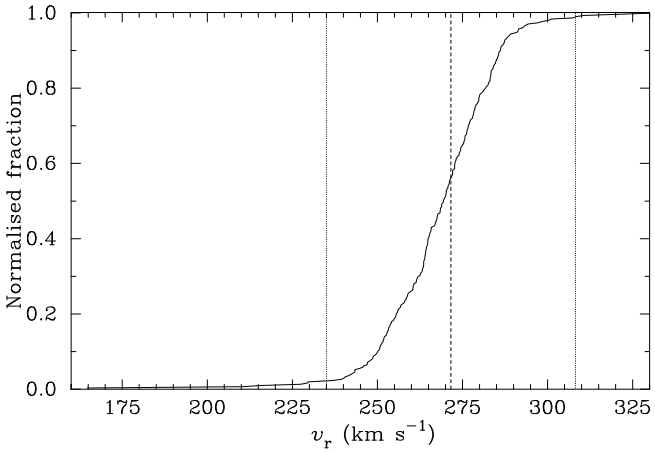

Fig. 6. Cumulative distribution of estimated radial velocities for the 307 single B-type stars. The dashed vertical line indicates the weighted mean velocity of the sample, $v_r = 271.6$ km s^{-1} (calculated excluding stars in the two older clusters and the candidate runaways). The vertical dotted lines are the 3σ thresholds adopted for identification of potential runways (± 36.6 km s^{-1}).

those for stars in NGC 2060 and NGC 2070, so we are unable to confirm it as a potential runaway from Hodge 301. Finally, we note that the velocity estimate for VFTS 310 is not significant as a potential runaway from Hodge 301.

With our adopted velocity criteria, the nine candidate runaways correspond to 2.9 % of the sample of 307 single stars with radial-velocity estimates. This lower fractional share of runaways compared to the O-type stars (Sana et al., in prep.) is in qualitative agreement with recent *N*-body predictions for the mass-spectrum of runaways (Banerjee et al. 2012; Banerjee & Kroupa 2012), although quantitative comparison with the predictions is complicated by the different criteria employed (e.g. Banerjee et al. used a radial distance threshold for a star to be considered a runaway). We note that the distribution in Fig. 6 is slightly asymmetric, with two thirds of the candidates having negative differential velocities. This could point to veiling of more distant runaways by the nebula, although this is not seen in the results for the O-type stars (in which a greater fraction are seen to have positive differential velocities, Sana et al., in prep.), suggesting that small-number statistics likely explain the asymmetry.

6.2. Rotational velocities of candidate runaways

Estimated projected rotational velocities (from Dufton et al. 2013; McEvoy et al. 2014) for our candidate B-type runaways are included in Table 5. There appears to be a dichotomy in their rotation rates, as highlighted by Fig. 7. Five stars have small rotational velocities, with the estimates for four stars effectively limited by the velocity resolution of the data (i.e. ~40 km s^{-1}) and the fifth with $v_e \sin i = 64 \pm 12$ km s^{-1}. Meanwhile, the remaining four stars each have estimates of $v_e \sin i \geq 345$ km s^{-1}. To investigate the significance of these results, we ran Monte Carlo simulations using the $v_e \sin i$ distributions from Dufton et al. (2013). We note that the results from Dufton et al. were for the unevolved B-type sample (i.e. dwarf and giant objects), so we exclude VFTS 831 from the following discussion.

We generated random rotational velocities for eight stars drawn from the distribution of Dufton et al., and repeated this 10^6 times to estimate the probability of recovering rotational velocities consistent with our eight (non-supergiant) runaway candidates (i.e. four stars with $v_e \sin i \leq 65$, and four with $v_e \sin i \geq 345$ km s^{-1}). We then repeated these runs 10^4 times to estimate the dispersion on the probabilities. In a second test we limited the low velocity subsample to the three stars with $v_e \sin i \leq 40$ km s^{-1} (i.e. excluding VFTS 625, which has the least significant runaway velocity), together with the four rapid rotators. We found low probabilities for recovering the observed $v_e \sin i$ values from both tests (as summarised in Table 6), with significance levels of 3.0 and 3.2σ, respectively.

We also investigated the probabilities compared to the cumulative distribution function of unprojected rotational velocities (v_e) from Dufton et al. (their Table 6). In this case we are limited by the unknown inclination angles of our targets but, assuming some relatively conservative lower-limits, we repeated tests similar to those above (in which we adopt the nearest available value from Dufton et al. for our upper limit, i.e. 340 km s^{-1}). These tests are formally less significant (Table 6), but provide further support that the rotational velocities of our candidate runaways do not appear to be randomly drawn from the distribution for the larger B-type sample. We note that this agrees with similar conclusions regarding the rotational velocities of the O-type runaways (Walborn et al. 2014; Sana et al., in prep.).

6.3. Atmospheric analysis of two candidate runaways

Atmospheric analysis of the B-type spectra is now underway within the VFTS project. In the context of the current study, we were particularly motivated to investigate the properties of the two most noteworthy runaway candidates, VFTS 358 and 831; we now comment briefly on our findings for these two objects.

Table 6. Probability tests to investigate the rotational velocities of the candidate runaway stars compared to those for the full (unevolved) B-type sample from Dufton et al. (2013).

Test (from 10^4 repeats of 10^6 runs)	n	P
$4 \times v_e \sin i \leq 65$ & $4 \times v_e \sin i \geq 345$ km s^{-1}	10 ± 3	0.0010
$3 \times v_e \sin i \leq 40$ & $4 \times v_e \sin i \geq 345$ km s^{-1}	6 ± 2	0.0006
$4 \times v_e \leq 100$ & $4 \times v_e \geq 340$ km s^{-1}	395 ± 20	0.0395
$3 \times v_e \leq 60$ & $4 \times v_e \geq 340$ km s^{-1}	181 ± 13	0.0181

Notes. "n": number of Monte Carlo runs (from 10^6 sets) for which the simulated rotational velocities are consistent with those of the candidate runaways (and translated into a fractional probability, P, in the final column); the quoted uncertainties are the standard deviations from 10^4 repeat runs.

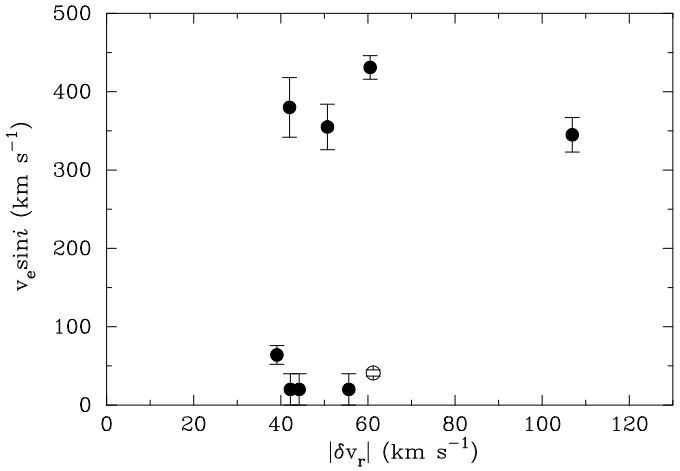

Fig. 7. Comparison of the projected rotational velocities ($v_e \sin i$) with the differential radial velocities (δv_r) compared to the mean systemic velocity of the B-type sample. Uncertainties on $v_e \sin i$ of ±10% are adopted for VFTS 368 and 831 (with the latter plotted as an open symbol given its supergiant classification).

6.3.1. VFTS 358

This star has the largest differential velocity from the estimated systemic value ($\delta v_r = -106.9 \pm 16.2$ km s^{-1}) and also has a relatively large projected rotational velocity ($v_e \sin i = 345 \pm 22$ km s^{-1}; Dufton et al. 2013). This prompted us to investigate its physical properties, in part to see if there was any evidence of past binary interaction (see e.g. de Mink et al. 2014).

Detailed analysis was complicated by the rapid rotation, which made estimation of the atmospheric parameters and element abundances difficult. However, using similar methods as those used by Hunter et al. (2007), we undertook a preliminary analysis using a grid of model atmospheres calculated using the TLUSTY and SYNSPEC codes (Hubeny 1988; Hubeny & Lanz 1995; Hubeny et al. 1998; Lanz & Hubeny 2007); further details of the grids are given by Ryans et al. (2003) and Dufton et al. (2005)[5].

We estimated the effective temperature ($T_{\rm eff}$) and gravity ($\log g$) of VFTS 358 by fitting rotationally-broadened profiles to the Hδ, Hγ and He II λ4686 lines, assuming solar helium abundances. This gave estimates of $T_{\rm eff} \simeq 29$ kK and $\log g \simeq 3.5$ dex, although we were unable to estimate the microturbulence because of the paucity of observable metal lines (which also precluded use of the silicon ionisation balance to estimate the temperature).

Absorption from N II λ3995 appears to be present in the spectrum (with an equivalent width of ~120 mÅ), although its identification is marginal, as shown in Fig. 8. Rotationally-broadened model spectra for our adopted physical parameters (and an assumed microturbulence of 5 km s^{-1}) are shown for three nitrogen abundances: $12 + \log({\rm N/H}) = 6.9$ (the approximate baseline N-abundance for the LMC, see discussion by Hunter et al. 2007), 7.7, and 8.5 dex plotted in red, green, and blue, respectively. This comparison suggests significant nitrogen enrichment, with an abundance of $\gtrsim$8.5 dex (the maximum abundance considered in our grid). Tests for theoretical profiles with a microturbulence of 20 km s^{-1} (which is larger than normally found for stars with this gravity, e.g. Hunter et al. 2007) implied a similarly large nitrogen abundance. Fitting a rotationally-broadened profile to the N II λ3995 line leads to $v_e \sin i = 342$ km s^{-1} (cf. 345 km s^{-1} from the helium lines) and a central wavelength of 3995.06 Å (cf. the laboratory wavelength of 3995.00 Å). This agreement provides some support that the feature is indeed from N II absorption.

The neutral helium lines in the observed spectrum appear somewhat stronger than those in the best-fitting model (e.g. the He I $\lambda\lambda$4009, 4026 lines in Fig. 8) suggesting that the helium abundance might also be enhanced. In turn, this would tend to decrease the $T_{\rm eff}$ estimated from the He II line (and the surface gravity). Tests using cooler models indicated that the change in nitrogen abundance would be modest. For example, a change in effective temperature of −2 kK leads to a change in $12 + \log({\rm N/H})$ of approximately −0.2 dex. Hence, the nitrogen abundance would still be significantly greater than the baseline value for the LMC.

At present we are limited by the quality of the VFTS spectrum but from this preliminary analysis there is evidence of significant nitrogen enrichment (and maybe also helium) in the photosphere of VFTS 358. Indeed, the estimated nitrogen abundance is the largest obtained so far from the VFTS survey (including results from the B-type supergiants from McEvoy et al. 2014). The large velocity offset, high rotation rate, enhanced nitrogen (and possibly helium) all fit, at least qualitatively, with a scenario in which VFTS 358 is the former secondary of an interacting binary that became unbound at the explosion of the primary star.

6.3.2. VFTS 831

VFTS 831 is remarkable in two regards. First as a luminous B-type supergiant, likely to be the evolved descendent of a formerly more massive O-type star, and secondly because, from the definition used in Table 4, it is located within SL 639 (≈12.″5 from the visual centre). With $v_r = 210.4 \pm 6.2$ km s^{-1} it also appears to be runaway compared to the other targets in SL639. A model-atmosphere analysis of the spectrum of VFTS 831 has been presented by McEvoy et al. (2014), who classified it as an apparently single star. It is one of the cooler objects in the supergiant sample, with $T_{\rm eff} = 14\,000$ K and $\log g = 2.1$.

Following the discussion in Sect. 6.2, VFTS 831 does not appear particularly remarkable in terms of stellar rotation. Indeed, it has a relatively low projected rotational velocity and a substantial contribution from macroturbulent broadening ($v_e \sin i$, $\Theta_{\rm RT}$) ~ (40, 65) km s^{-1}, as found in most B-type supergiants (see e.g. Markova et al. 2014; Simón-Díaz & Herrero 2014). From the intrinsically strong N II λ3995 singlet transition, McEvoy et al. (2014) estimated a nitrogen abundance of $12 + \log({\rm N/H}) = 7.94$.

[5] See also http://star.pst.qub.ac.uk

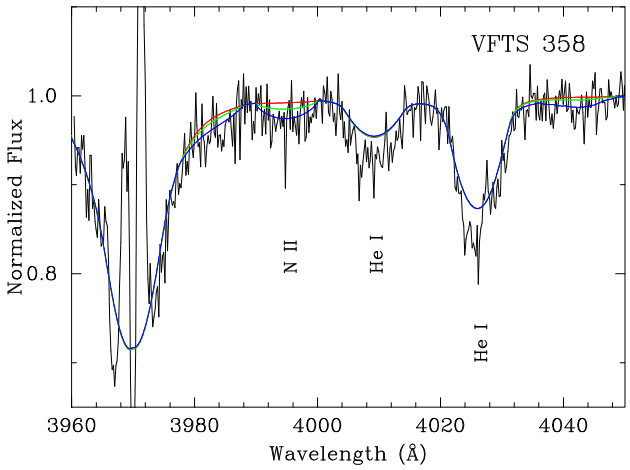

Fig. 8. Section of the VFTS 358 spectrum showing, from left-to-right, the Hϵ, N II λ3995, and He I $\lambda\lambda$4009, 4026 lines; we note that Hϵ is complicated by absorption from the interstellar Ca *H* line (as well as nebular emission). Model spectra for our adopted physical parameters and $12 + \log(\mathrm{N/H}) = 6.9$, 7.7, and 8.5, are overplotted in red, green, and blue, respectively.

Although large, this is consistent with the other single supergiants in the sample, which have abundances spanning approximately 6.8 to 8.1 dex.

6.4. Single-lined binaries

For completeness we also investigated the velocities of single-lined binaries for potential runaway systems. In the final column of Table A.3 we include the observed *range* of velocities, $\delta v_{\mathrm{r\,max}}$, from Dunstall et al. (in prep.). Following the arguments laid out in Sect. A.3 of the Appendix, we adopt an estimated error on the true systemic velocity compared to the single-epoch estimate of $0.15 \times \delta v_{\mathrm{r\,max}}$. For stars with v_{r} above (or below) the systemic velocity, we then subtract (or add) this estimated error, to give a corrected velocity estimate, v_{corr}. Using the same 3σ criteria discussed above we then looked for potential runaways.

Only one single-lined system, VFTS 730, was found to be a potential runaway, with $v_{\mathrm{corr}} = 324.0\,\mathrm{km\,s^{-1}}$ (a 4.3σ outlier cf. the adopted systemic velocity). Its range of observed velocities is relatively small ($\delta v_{\mathrm{r\,max}} = 16.6\,\mathrm{km\,s^{-1}}$, thus only just above the detection threshold employed by Dunstall et al.) but it could be, for example, a long-period system with an eccentric orbit. Indeed, inspection of its velocity estimates as a function of epoch show them to be monotonically decreasing from 332 to 316 $\mathrm{km\,s^{-1}}$, suggesting it as a long-period system. Further investigation of this (and other) binary systems will require comprehensive spectroscopic monitoring to determine their centre-of-mass velocities and other orbital parameters.

6.5. Origins of candidate runaways

The production of runaways is thought to be from one of two channels, with evidence in support of both mechanisms (Hoogerwerf et al. 2000). In the dynamical-ejection scenario the runaway is ejected via gravitational interaction between single-binary or binary-binary systems in a dense star cluster (Poveda et al. 1967). In the binary-ejection scenario, the primary star explodes as a supernova, leaving behind a neutron star or black hole. In most cases the compact object leaves the system depending on the magnitude and direction of the birth kick, and the companion is ejected with a velocity approximately equal to its orbital velocity (Blaauw 1961; Eldridge et al. 2011).

The complex star-formation history of 30 Dor makes it hard to cleanly attribute our candidate runaways to either of the two scenarios. R136 is sufficiently young (1–2 Myr; de Koter et al. 1998; Massey & Hunter 1998) that none of its members is thought to have undergone a supernova explosion. Thus, any runaways from R136 would have to be ejected via dynamical interactions. However, as noted above, the VFTS region contains several older subclusters and associations, including NGC 2060, which contains a supernova remnant (e.g. Chu et al. 1992), and Hodge 301 which was argued by Grebel & Chu (2000) as a likely site of tens of past supernovae from consideration of its mass function.

One of the important diagnostics might prove to be the connection with the observed rotational velocities (Fig. 7), in which the apparently rapid rotators could have a binary origin. For example, the theoretical discussions by de Mink et al. (2013), and the suggestion that the high-$v_{\mathrm{e}} \sin i$ tail of the distribution of the rotational velocities for the VFTS O-type stars could be accounted for by past binary interactions (Ramírez-Agudelo et al. 2013). Detailed dynamical analysis of the O-type stars in the survey has been underway in parallel to the current work, and the broader question of the origins of runaway stars from 30 Dor is discussed in more depth by Sana et al. (in prep.).

7. Summary

We have presented comprehensive spectral classifications and radial-velocity estimates for the B-type stars observed in the VFTS. We now briefly summarise our main findings:

- The members of the two older clusters, Hodge 301 and SL 639, appear kinematically distinct from those in the younger clusters and general field population.
- The preliminary H-R diagram for stars in Hodge 301 and SL 639 (Fig. 5) suggests an age of ~10–15 Myr for the population of SL 639, slightly younger than that of Hodge 301 (15 ± 5 Myr).
- The systemic velocity for 273 single stars, excluding those in the two older clusters and candidate runaways, is $\overline{v_{\mathrm{r}}} = 271.6 \pm 12.2$ (s.d.) $\mathrm{km\,s^{-1}}$.
- Employing a 3σ velocity threshold, we identify nine single stars as candidate runaways (2.9 % of the single stars with radial-velocity estimates). These are mostly unevolved, early B-type objects, but include a B5-type supergiant (VFTS 831).
- There appears to a bimodal distribution of rotation rates in the candidate runaways. Five stars have $v_{\mathrm{e}} \sin i \leq 65\,\mathrm{km\,s^{-1}}$, while the others have $v_{\mathrm{e}} \sin i \geq 345\,\mathrm{km\,s^{-1}}$.
- Excluding VFTS 831 (because of its evolved nature), there is a remarkably small probability (~0.001%) that the projected rotational velocities for our other eight candidate runaways could be randomly drawn from those for the full (unevolved) B-type sample.
- VFTS 358 has the largest velocity offset from the systemic velocity of 30 Dor ($\delta v_{\mathrm{r}} = -106.9 \pm 16.2\,\mathrm{km\,s^{-1}}$) and appears to be rotating rapidly ($v_{\mathrm{e}} \sin i = 345\,\mathrm{km\,s^{-1}}$). Preliminary spectral analysis suggests evidence of significant nitrogen enrichment, perhaps indicative of past binary interaction.

The classifications presented here will underpin the quantitative analyses in progress on this substantial part of the VFTS data. For example, they will enable investigation of the

mass/temperature dependence (if any) of the estimated $v_e \sin i$ results from Dufton et al. (2013), particularly when also combined with the results for the O-type stars from Ramírez-Agudelo et al. (2013). In the longer-term, the ongoing proper-motion studies using *HST* imaging (programme GO12499, P.I. Lennon) will add another dimension to our studies of the complex dynamics in this region, by providing tangential velocities (see Sabbi et al. 2013).

Our radial-velocity estimates should also lend themselves to detailed investigation of the structural properties of the VFTS sample (e.g. using the techniques discussed by Parker et al. 2014; Wright et al. 2014), particularly when combined with the results for the O-type stars from Sana et al. (2013); this should provide further insights into the formation and evolutionary history of the massive-star population in the region.

Finally, there is an ongoing monitoring programme of FLAMES spectroscopy to characterise a subset of the O-type binaries (PI: Sana); a similar monitoring programme for the ~100 binaries discussed here and by Dunstall et al. (in prep.) would be valuable to determine the full orbital parameters of the lower-mass population of binaries, while also providing robust estimates of centre-of-mass velocities to better explore their dynamics in the context of ejected runaways.

Acknowledgements. Based on observations at the European Southern Observatory Very Large Telescope in programme 182.D-0222. We thank Mark Gieles for helpful discussions regarding the candidate runaways, and the referee for their constructive comments. STScI is operated by AURA Inc., under NASA contract NAS 5-26555. S.d.M. acknowledges support for this work by NASA through an Einstein Fellowship grant, PF3-140105. J.M.A. acknowledges support by grants AYA2010-17631 and AYA2010-15081 of the Spanish Ministry of Economy and Competitiveness. S.S.-D. acknowledges funding from the Spanish Government Ministerio de Economía y Competitividad (MINECO) through grants AYA2010-21697-C05-04, AYA2012-39364-C02-01 and Severo Ochoa SEV-2011-0187, and the Canary Islands Government under grant PID2010119.

References

Andrews, A. D., & Lindsay, E. M. 1964, Irish AJ, 6, 241
Balona, L. A. 1994, MNRAS, 267, 1060
Banerjee, S., & Kroupa, P. 2012, A&A, 547, A23
Banerjee, S., Kroupa, P., & Oh, S. 2012, ApJ, 746, 15
Bica, E., Santos, Jr., J. F. C., & Alloin, D. 1990, A&A, 235, 103
Blaauw, A. 1961, Bull. Astron. Inst. Netherlands, 15, 265
Bohannan, B., & Epps, H. W. 1974, A&AS, 18, 47
Bonanos, A. Z., Massa, D. L., Sewiło, M., et al. 2009, AJ, 138, 1003
Bosch, G. L., Terlevich, R., Melnick, J., & Selman, F. 1999, A&AS, 137, 21
Brott, I., de Mink, S. E., Cantiello, M., et al. 2011, A&A, 530, A115
Brunet, J. P., Imbert, M., Martin, N., et al. 1975, A&AS, 21, 109
Chu, Y.-H., Kennicutt, R. C., Schommer, R. A., & Laff, J. 1992, AJ, 103, 1545
Clark, J. S., Tarasov, A. E., & Panko, E. A. 2003, A&A, 403, 239
Clark, J. S., Najarro, F., Negueruela, I., et al. 2012, A&A, 541, A145
Clark, J. S., Ritchie, B., & Negueruela, I. 2013, A&A, 560, A11
de Koter, A., Heap, S. R., & Hubeny, I. 1998, ApJ, 509, 879
de Mink, S., Langer, N., Izzard, R. G., Sana, H., & de Koter, A. 2013, ApJ, 764, 166
de Mink, S., Sana, H., Langer, N., Izzard, R. G., & Schneider, F. R. N. 2014, ApJ, 782, 7
Doran, E. I., Crowther, P. A., de Koter, A., et al. 2013, A&A, 558, A134
Dufton, P. L., Ryans, R. S. I., Trundle, C., et al. 2005, A&A, 434, 1125
Dufton, P. L., Langer, N., Dunstall, P. R., et al. 2013, A&A, 550, A109
Dunstall, P. R., Fraser, M., Clark, J. S., et al. 2012, A&A, 542, A50
Eldridge, J. J., Langer, N., & Tout, C. A. 2011, MNRAS, 414, 3501
Evans, C. J., & Howarth, I. D. 2003, MNRAS, 345, 1223
Evans, C. J., Lennon, D. J., Smartt, S. J., & Trundle, C. 2006, A&A, 456, 623
Evans, C. J., Walborn, N. R., Crowther, P. A., et al. 2010, ApJ, 715, L74
Evans, C. J., Taylor, W. D., Hénault-Brunet, V., et al. 2011, A&A, 530, A108 (Paper I)
Feast, M. W., Thackeray, A. D., & Wesselink, A. J. 1960, MNRAS, 121, 337
Fitzgerald, M. P. 1970, A&A, 4, 234
Fitzpatrick, E. L. 1988, ApJ, 335, 703
Fitzpatrick, E. L. 1991, PASP, 103, 1123
Fujii, M. S., & Portegies Zwart, S. 2011, Science, 334, 1380
Graus, A. S., Lamb, J. B., & Oey, M. S. 2012, ApJ, 759, 10
Grebel, E. K., & Chu, Y.-H. 2000, AJ, 119, 787
Groh, J., Meynet, G., Ekstrom, S., & Georgy, C. 2014, A&A, 564, A30
Gummersbach, C. A., Zickgraf, F.-J., & Wolf, B. 1995, A&A, 302, 409
Hodge, P. 1983, ApJ, 264, 470
Hodge, P. 1988, PASP, 100, 1051
Hoogerwerf, R., de Bruijne, J. H. J., & de Zeeuw, P. T. 2000, ApJ, 544, L133
Houk, N., & Smith-Moore, M. 1988, Michigan Catalogue of Two-dimensional Spectral Types for the HD Stars. Vol. 4, Declinations −26° to −12° (Department of Astronomy, University of Michigan)
Howarth, I. D. 2012, A&A, 548, A16
Howarth, I. D. 2013, A&A, 555, A141
Hubeny, I. 1988, Comput. Phys. Comm., 52, 103
Hubeny, I., & Lanz, T. 1995, ApJ, 439, 875
Hubeny, I., Heap, S. R., & Lanz, T. 1998, in Properties of Hot Luminous Stars, ed. I. Howarth, ASP Conf. Ser., 131, 108
Hunter, I., Dufton, P. L., Smartt, S. J., et al. 2007, A&A, 466, 277
Kalari, V. M., Vink, J. S., Dufton, P. L., et al. 2014, A&A, 564, L7
Kramida, A., Ralchenko, Y., Reader, J., & NIST ASD Team 2012, in NIST Atomic Spectra Database (v5.0); http:/physics.nist.gov/asd (National Institute of Standards and Technology, Gaithersburg, MD.)
Lanz, T., & Hubeny, I. 2007, ApJS, 169, 83
Lennon, D. J. 1997, A&A, 317, 871
Markova, N., Bianchi, L., Efremova, B., & Puls, J. 2009, Bulgar. Astron. J., 12, 21
Markova, N., Puls, J., Simón-Díaz, S., et al. 2014, A&A, 562, A37
Martayan, C., Hubert, A.-M., Floquet, M., et al. 2006, A&A, 445, 931
McEvoy, C. M., Dufton, P. L., Evans, C. J., et al. 2014, A&A, in press, DOI: 10.1051/0004-6361/201425202
Massey, P., & Hunter, D. A. 1998, ApJ, 493, 180
Meixner, M., Gordon, K. D., Indebetouw, R., et al. 2006, AJ, 132, 2268
Melnick, J. 1985, A&A, 153, 235
Parker, J. W. 1993, AJ, 106, 560
Parker, R. J., Wright, N. J., Goodwin, S. P., & Meyer, M. R. 2014, MNRAS, 438, 620
Pasquini, L., Avila, G., Blecha, A., et al. 2002, Msngr, 110, 1
Portegies Zwart, S. F. 2000, ApJ, 544, 437
Poveda, A., Ruiz, J., & Allen, C. 1967, Boletín de los Observatories to Tonantzintla y Tacubaya, 4, 86
Ramírez-Agudelo, O. H., Simón-Díaz, S., Sana, H., et al. 2013, A&A, 560, A29
Rivinius, T., Carciofi, A. C., & Martayan, C. 2013, A&ARv, 21, 69
Ryans, R. S. I., Dufton, P. L., Mooney, C. J., et al. 2003, A&A, 401, 1119
Sabbi, E., Lennon, D. J., Gieles, M., et al. 2012, ApJ, 754, L37
Sabbi, E., Anderson, J., Lennon, D. J., et al. 2013, AJ, 146, 53
Sana, H., de Koter, A., de Mink, S. E., et al. 2013, A&A, 550, A107
Sanduleak, N. 1970, Contrib. Cerro Tololo Inter-American Obs., No. 89
Santos, Jr., J. F. C., Bica, E., Claria, J. J., et al. 1995, MNRAS, 276, 1155
Schild, H., & Testor, G. 1992, A&AS, 92, 729
Shapley, H., & Lindsay, E. M. 1963, IrAJ, 6, 74
Simón-Díaz, S., & Herrero, A. 2014, A&A, 562, A135
Smith, N., Vink, J. S., & de Koter, A. 2004, ApJ, 615, 475
Sota, A., Maíz Apellániz, J., Walborn, N. R., et al. 2011, ApJS, 193, 24
Testor, G., Llebaria, A., & Debray, B. 1988, Msngr, 54, 43
Townsley, L. K., Broos, P. S., Feigelson, E. D., et al. 2006, AJ, 131, 2164
Townsley, L. K., Broos, P. S., Garmire, G. P., et al. 2014, ApJS, 213, 1
Trundle, C., Dufton, P. L., Hunter, I., et al. 2007, A&A, 471, 625
Walborn, N. R. 1976, ApJ, 205, 419
Walborn, N. R. 1984, in IAU Symp. 108, Structure and Evolution of the Magellanic Clouds, eds. S. van den Bergh, & K. S. de Boer (Dordrecht: Reidel), 243
Walborn, N. R. 1986, in IAU Symp. 116, Luminous Stars and Associations in Galaxies, eds. C. W. H. de Loore, A. J. Willis, & P. Laskarides (Dordrecht: Reidel), 185
Walborn, N. R., & Blades, J. C. 1997, ApJS, 112, 457
Walborn, N. R., & Fitzpatrick, E. L. 1990, PASP, 102, 379
Walborn, N. R., & Fitzpatrick, E. L. 2000, PASP, 112, 50
Walborn, N. R., Howarth, I. D., Lennon, D. J., et al. 2002a, AJ, 123, 2754
Walborn, N. R., Maíz-Apellániz, J., & Barbá, R. H. 2002b, AJ, 124, 1601
Walborn, N. R., Sana, H., Simón-Díaz, S., et al. 2014, A&A, 564, A40
Wright, N. J., Parker, R. J., Goodwin, S. P., & Drake, J. J. 2014, MNRAS, 438, 639
Zorec, J., & Briot, D. 1997, A&A, 318, 443

Pages 14 to 40 are available in the electronic edition of the journal at http://www.aanda.org

Table 7. Spectral classifications and radial velocities for B-type stars in the VFTS.

VFTS	Spectral type	Mult.?	Hα	V	$B-V$	v_r [km s^{-1}]	σ	Set	Alt. ID	Comments
001	B1.5: V	...	a	16.93	0.05	282.1	4.2	2	...	...
003	B1 Ia$^+$	...	q?	–	–	265.2	2.1	1	Sk−69° 224	...
004	B2 V	...	a	16.87	0.16	283.1	10.8	2	...	...
005	B2 V(n)	...	a	16.25	0.02	282.6	2.6	2	...	...
007	B1-2 V	...	a	16.74	0.03	281.1	1.6	2	...	...
008	B0.5: V(n)	...	a	16.92	0.07	271.3	6.9	2	...	...
009	B1-1.5 V	✓	a	16.18	0.11	293.2	21.6	B	...	...
010	B2 V	...	a	16.79	0.04	287.1	3.9	1	...	...
013	B1.5 V	...	a	16.36	0.13	290.9	4.3	2	...	...
015	B0.5 V	✓	a	16.20	0.04	278.0	30.5	B	...	...
017	B0 V	✓	a	–	–	280.9	31.0	B	...	Walborn et al. (2014)
018	B1.5 V	✓	a	16.62	0.17	279.2	11.9	B	...	...
020	B2.5: V(n)	...	a	16.70	0.06	258.8	16.3	2	...	...
022	B0-0.5 V-IIIe	...	e	16.67	0.55	...	...	...	...	Hα broad but weak
024	B0.2 III-II	...	f	16.02	0.37	285.7	4.4	1	...	...
025	B1-1.5 V	✓	a	16.18	0.06	290.3	11.3	B	...	...
027	B1 III-II	✓	a	14.71	0.09	273.1	42.5	B	...	...
028	B0.7 Ia Nwk	...	q?	13.48	0.24	273.5	4.4	1	...	Hα emission extends redwards
029	B1 V	...	a	16.73	−0.02	285.6	3.0	1	...	...
030	B3-5e (shell)	...	e	16.34	0.10	...	...	...	...	...
031	B1.5 V	...	?	16.41	0.00	280.0	8.4	1	...	...
033	B1-1.5 V	✓	a	16.20	0.07	270.2	22.8	B	...	...
034	B1.5 Ve	...	e	16.14	0.13	308.3	13.8	1	...	...
036	B1: Vn	...	a	16.61	0.10	270.8	18.4	2	...	...
037	B2 III:	✓	a	15.79	0.06	299.4	18.4	B	...	...
038	B1.5 V	...	a	16.54	0.06	278.0	4.1	2	...	...
039	B0:e	...	e	14.52	0.52	...	...	...	ST92 1-01	...
040	B1-2 Vn	...	a	16.85	0.10	291.4	12.6	2	ST92 1-02	B1 V [ST92]
041	B2: V	✓	a	16.94	0.14	287.0	19.0	B	...	...
043	B2 V(n)	...	a	16.49	−0.06	263.6	4.4	2	...	...
044	B2 V	...	a	16.62	−0.07	288.1	7.2	1	...	...
048	B1 V	...	a	16.72	0.14	274.1	3.3	2	...	...
050	B0 V	...	a	16.77	0.18	283.1	2.0	1	...	...
052	B0.2 III-II	...	a	14.55	−0.07	279.8	2.0	1	...	...
053	B1 III	...	f	15.28	0.09	276.4	2.0	1	...	...
054	B0 V	...	f	16.60	0.21	265.7	19.9	2	...	Si IV wk
060	B1.5 II-Ib((n))	...	a	16.12	0.62	284.2	14.3	1	...	...
062	B3 III	...	a	16.27	0.15	287.5	2.7	1	...	...

Notes. Column entries are: (1) VFTS identifier; (2) spectral classification; (3) binary status (from Dunstall et al., in prep.) (4) Hα morphology: "a" = (photospheric) absorption, "e" = (stellar) emission; "f" = flat, with no indication of the nature of the line profiles outside the region of nebular emission (i.e. no strong, broad emission); "q" = P-Cygni profile (used classically to distinguish from a "p" suffix, which simply indicates peculiar); (5) and (6) V and $B-V$ photometry from Paper I; (7) and (8) estimated radial velocity (v_r) and standard deviation (σ); (9) method/lines used to estimate v_r: "1" and "2" refer to the lines listed in Table 3, "3" indicates the three stars for which other metal lines were used, "B" indicates that the estimate is the mean value from the multi-epoch data available (see Sect. 4.2, with the limitations of these as estimates of the centre-of-mass velocities discussed in Sect. A.3); (10) alternative identifiers used in the literature; (11) previous classifications and other relevant comments. Aliases/past classifications are from: R/F60 (Feast et al. 1960); AL (Andrews & Lindsay 1964); Sk (Sanduleak 1970); BE74 (Bohannan & Epps 1974); BI (Brunet et al. 1975); W84 (Walborn 1984); Mk (Melnick 1985); W86 (Walborn 1986); T88 (Testor et al. 1988); ST92 (Schild & Testor 1992); P93 (Parker 1993); WB97 (Walborn & Blades 1997); B99 (Bosch et al. 1999). The crosschecks with the catalogues from Andrews & Lindsay (1964) and Bohannan & Epps (1974) employed the updated astrometry from Howarth (2012, 2013).

Table 7. continued.

VFTS	Spectral type	Mult.?	Hα	V	$B-V$	v_r [km s^{-1}]	σ	Set	Alt. ID	Comments
068	B1-1.5e	...	e	15.65	0.77	254.8	24.0	2	...	Composite spectrum?
069	B0.7 Ib-Iab	...	q?	13.59	0.17	280.7	1.7	1	ST92 1-17	B1 III [ST92]
071	B1: V	...	a	16.65	0.03	268.4	4.3	2	...	...
075	B1 V	...	a	16.93	0.03	297.2	10.5	1	...	...
078	B1 V	...	a	16.63	0.21	283.1	3.7	2	...	...
082	B0.5 Ib-Iab	...	a	13.61	−0.06	283.3	2.4	1	...	
083	B1.5 V	...	a	15.91	0.10	287.3	3.7	2	...	...
084	B1.5 V	...	a	16.84	0.18	276.2	3.8	2	...	...
085	B1.5 V	...	a	16.48	−0.08	285.3	3.6	2	...	...
088	B0: V-III(n)	...	e(?)	15.24	−0.06	284.0	7.4	2	...	Weak but broad Hα emission
095	B0.2 V	...	a	16.06	−0.02	294.3	3.8	1	...	...
097	B0 IV	✓	a	16.21	0.16	296.7	11.5	B	ST92 1-31	B0.5 V [ST92]; Walborn et al. (2014)
099	B2-2.5 V	...	a	16.78	−0.03	...	...	...	...	...
100	B1.5 V	...	a	16.68	0.22	257.6	1.4	2	...	...
101	B0.7: Vne	...	e	16.39	0.32	277.3	4.8	2	ST92 1-33	B1 V [ST92]
106	B0.2 V	✓	f	16.43	0.05	281.8	13.3	B	...	...
107	B1: V	✓	f	16.68	0.06	294.5	23.7	B	...	...
111	B2 III	...	a	14.40	−0.08	272.0	4.2	1	...	...
112	Early B + Early B	✓	a	16.19	0.08	...	...	...	...	...
118	B1 IV	✓	a	16.21	0.20	302.2	15.9	B	...	...
119	B0.7 V	...	a	16.36	0.07	275.8	3.9	1	...	...
121	B1 IV	...	a	15.96	0.06	283.4	2.8	1	...	...
122	B1.5 V	...	a	16.53	0.24	260.7	17.6	2	...	...
124	B2.5 III	...	a	16.61	0.24	289.4	2.2	1	ST92 1-46	B1 V [ST92]
126	B1 V	...	a	16.78	−0.07	254.1	2.6	1	...	...
127	B2: V(n)	...	a	16.93	0.07	243.3	5.5	2	...	...
133	B0.5 V	✓	a	16.03	−0.02	293.5	15.2	B	...	...
134	B1 V(n)	...	a	16.85	0.02	262.8	9.4	2	...	...
135	B1: V-IIIne	✓	e	16.01	0.01	270.9	52.5	B	...	Broad, weak Hα emission wings
137	B0.7 V	...	a	16.85	0.11	284.0	3.1	2	ST92 1-55	B1 V [ST92]
144	B0.7: V	✓	f	16.81	0.00	281.8	14.5	B	T88-10	...
146	B2: V	✓	a	16.24	0.25	259.6	12.6	B	...	...
152	B2 IIIe	...	e	15.32	0.25	274.3	2.9	1	...	B2 V [Paper I]; weak Hα emission wings
155	B0.7: V	✓	a	16.95	0.08	...	...	...	...	...
156	B1-1.5 V-IIIe+	...	e	16.26	0.44	283.8	18.3	2	T88-11, ST92 1-64	B1: [ST92]
157	B2 V	✓	a	16.69	−0.08	284.0	24.4	B	...	...
158	B1-1.5 Ve+	...	e	15.33	0.20	285.7	19.3	2	...	...
159	B2.5 III	...	a	15.61	−0.03	267.5	6.1	1	...	...
161	B1 V	...	a	16.69	0.24	262.6	7.9	1	...	...
162	B0.7 V	✓	a	16.49	0.07	283.7	14.8	B	...	...
164	B2: V-IIIe+	...	e	16.54	0.35	300.4	10.0	1	ST92 1-67	B1: [ST92]
166	B2: V-IIIe+	...	e	16.93	0.16	274.4	5.6	2	...	...
167	B1 V	...	a	16.07	0.01	286.9	5.0	2	...	...
170	B1 IV	...	a	16.03	0.15	278.7	2.7	1	...	...
179	B1 V	✓	a	16.93	0.09	294.5	6.4	B	...	...
181	B0.5 V	...	a	16.24	0.15	278.9	11.9	2	...	...
183	B0 IV-III	...	a	16.51	0.38	256.1	1.7	1	...	B0 IV (Walborn et al. 2014)

Table 7. continued.

VFTS	Spectral type	Mult.?	Hα	V	$B-V$	v_r [km s^{-1}]	σ	Set	Alt. ID	Comments
186	B1 IV	...	a	15.79	0.11	264.3	10.6	1	...	...
189	B0.7: V	✓	a	16.31	0.10	274.0	69.9	B	ST92 1-82	B2 V [ST92]
194	B2 V-IIIe+	...	e	16.08	0.12	277.9	13.0	2	...	...
195	B0.5 V	✓	a	16.86	0.06	268.1	12.9	B	...	...
196	B2 IIIe+	...	e	15.58	0.05	271.9	7.1	2	...	...
199	Early B + Early B	✓	a	16.91	−0.01	...	...	B	...	...
200	B1-1.5 IIIe+	...	e	14.83	0.09	253.6	8.0	1	ST92 1-89	B1 V [ST92]
202	B2 V	...	a	16.16	0.13	276.6	2.3	1	ST92 1-90	B2 V [ST92]
203	B1-1.5 V	...	f	16.77	−0.02	272.8	6.8	2	...	...
204	B2 III	✓	a	16.13	0.31	254.9	12.7	B	...	...
206	B3 III:	✓	a	14.99	0.15	257.3	36.8	B	...	...
209	B1 V	...	a	16.33	−0.06	273.1	2.6	1	...	...
211	B1 V	✓	f	16.56	−0.12	272.0	13.2	B	...	...
212	B1 III	...	a	15.18	0.02	286.2	2.5	2	ST92 1-95	B1 V [ST92]
213	B2 III:e	✓	e	15.50	0.04	276.4	12.8	B	ST92 1-96	...
214	B0 IV-III	...	a	15.84	0.27	275.4	1.7	1	...	...
215	B1.5 V	✓	f	16.58	−0.03	287.5	63.0	B	...	...
218	B1.5 V	✓	a	15.63	0.38	249.2	7.9	B	ST92 1-99	...
219	B3-5 V-III	...	f	16.93	0.04	282.5	12.6	2	...	...
220	B0.7 V	...	f	16.66	0.03	282.6	3.3	1	...	...
221	B1 V	...	f	16.27	−0.08	261.4	8.2	2	...	...
224	B1-2 V-IIIe+	...	e	16.02	0.11	263.9	25.8	2	...	...
225	B0.7-1 III-II	✓	e?	15.07	−0.01	289.2	15.8	B	...	Broad but weak Hα em. (poss. cross-contamination from VFTS 507)
227	B2 V	✓	f	16.51	−0.09	277.4	9.1	B	...	...
228	B0.7 V	...	f	16.46	−0.04	281.2	6.5	2	...	...
229	B1.5 Vn	...	f	16.48	0.00	272.8	11.0	2	...	...
230	B1.5 III	...	a	16.59	0.44	279.7	7.5	2	...	...
232	B3 Ia	...	a	14.52	0.50	288.6	2.5	1	ST92 1-104	B2: [ST92]
233	B1-2 V-IIIe	...	e	16.40	0.23	248.2	11.9	2	...	...
234	B1.5 V	...	a	16.22	0.11	247.0	10.3	2	...	...
237	B1-1.5 V-IVe	...	e	15.93	0.06	287.9	10.5	1	...	...
238	B2.5 V	...	f	16.84	−0.01	268.5	13.5	2	...	...
239	B1 V	...	a	16.41	0.02	274.7	6.5	2	...	...
240	B1-2 V (SB2)	✓	a	15.85	0.01	224.2	52.6	B	...	Weak secondary He I in some LR02 epochs
241	B0 V-IV	...	a	16.65	−0.03	267.6	8.7	1	...	B0 IV (Walborn et al. 2014)
242	B0 V-IV	...	f	16.82	0.04	216.0	3.6	1	...	B0 IV (Walborn et al. 2014)
246	B1 III	✓	a	16.83	0.45	275.8	28.8	B	...	...
247	B2 V	...	a	16.88	0.02	293.6	4.1	2	...	...
248	B2: V	✓	a	16.49	0.00	297.6	35.8	B	...	...
254	B1-2 Ve	...	e	16.90	0.03	250.7	5.6	2	...	...
255	B2: V	✓	a	16.68	0.02	268.5	65.4	B	...	...
257	B0.7-1.5 V	✓	a	16.70	−0.04	269.2	11.9	B	...	...
258	B1.5 V	...	a	16.34	0.10	287.3	5.9	1	...	...
261	B5 Ia	...	a?	12.33	0.03	285.0	2.2	1	...	Hα asymmetric, possible weak P-Cygni?
263	B2: V-IIIe+	...	e	16.80	0.05	270.1	16.8	2	...	...
268	B1.5 Ve+	...	e	16.65	0.11	272.1	14.5	1	...	...
269	B8 Ia	...	q?	12.90	0.05	266.9	2.1	1	R132, WB97-1	B0.5 Ia [Mk]; complex Hα profile, probable emission; member of H 301

Table 7. continued.

VFTS	Spectral type	Mult.?	Hα	V	$B-V$	v_r [km s^{-1}]	σ	Set	Alt. ID	Comments
270	B3 Ib	...	a	14.35	−0.07	264.9	2.3	1	WB97-2	Member of H 301
272	B3: IIIe+ (shell?)	...	e	16.00	−0.01	264.2	4.4	3	GC00-Be5	Member of H 301
273	B2.5 V	...	a	16.74	0.03	253.8	4.9	1	...	...
274	B1 V(n)	...	a	16.94	−0.01	252.9	14.1	2	...	...
276	B1.5 V	...	a	15.84	−0.13	256.8	5.9	1	GC00-Be2	Only nebular Hα emission?; member of H 301
278	B2.5 V	✓	f	16.82	−0.07	270.8	12.8	B	...	Member of H 301
279	B2: Ve+	...	e	16.73	0.05	262.6	14.1	2	GC00-Be8	Member of H 301
282	B3-5 III(n)e	...	e	16.11	−0.06	260.5	19.7	2	GC00-Be7	Str. Si II; member of H 301
283	B1.5 V-III(n)e	...	e	15.31	−0.01	252.1	6.0	2	WB97-6, GC00-Be4	B2 III [WB97]; known triple, inc. GC00-Be10; member of H 301
284	B1 V	...	a	16.84	−0.02	272.7	3.9	1	...	...
286	B0.7 V	...	f	15.83	−0.08	278.4	4.4	2	...	...
287	B2.5 Vne	...	e	16.58	−0.08	264.7	11.4	2	GC00-Be9	Member of H 301
288	B2.5 III:n	...	f	16.58	0.13	258.0	7.2	2	...	...
291	B5 II-Ib	✓	e	14.85	0.12	234.7	46.1	B	WB97-8	B5:p [WB97]
292	B2.5 V(n)	...	f	16.47	−0.14	263.6	4.9	2	...	Member of H 301
293	B2 III-II(n)e	...	e	14.95	−0.04	260.4	1.9	1	WB97-9, GC00-Be1	B2p?, B2 V var. [WB97]; member of H 301
295	B0-0.5 V	...	f	16.33	−0.07	307.7	12.0	2	...	...
296	B2 III	...	a	15.45	−0.01	250.0	7.8	1	...	...
297	B1.5 V	...	f	16.64	0.04	251.7	2.2	1	...	Member of H 301
298	B1-2 V-IIIe+	...	e	16.68	0.24	332.1	4.0	2	...	...
299	B0.5 V	✓	a	16.36	−0.05	288.9	45.8	B	...	...
300	B1-2 Vn	...	a	16.41	−0.03	276.7	12.1	2	...	...
301	B2: Ve+	...	e	–	–	268.4	9.0	2	GC00-Be3	GC00-Be6 is ∼1.″0 NW; member of H 301
302	B1.5 Ib	...	a	15.53	0.32	264.8	1.6	1	...	...
305	B2: V	✓	a	16.59	−0.10	321.7	50.4	B	...	...
307	B1 II-Ib	...	a	13.56	−0.06	272.7	2.0	1	Sk−68° 136	...
308	B2 V	...	a	15.88	−0.01	263.5	1.9	1	...	Member of H 301
309	B2 V-III	...	e(?)	16.19	0.00	281.8	7.6	2	...	Member of H 301
313	B0 V-IV	...	a	16.32	0.07	270.7	3.3	1	...	B0 IV (Walborn et al. 2014)
315	B1 Ib	...	a	14.81	0.03	261.6	1.5	1	...	...
320	B1-2 V-IIIe+	...	e	16.11	0.23	291.3	22.1	2	...	Be [Paper I]
321	B1: V	...	a	16.89	−0.03	258.6	5.6	2	P93-0003	...
322	B1.5-2 Ve+	...	e	16.76	0.17	276.9	11.1	2	P93-0006	...
324	B0.2 V	✓	a	15.53	−0.13	274.6	25.1	B	...	Poss. double-peaked core Hα em. in broad photospheric abs.
325	B1 V	✓	f	16.84	−0.03	287.4	46.0	B	P93-0009	...
326	B1-2 Vn	...	a	16.53	−0.06	250.1	8.8	2	P93-0014	...
330	B2 III(n)e	...	e	16.14	0.18	267.7	4.4	2	...	Broad, weak Hα emission shoulders
331	B1.5 V	...	a	16.71	−0.06	279.4	7.3	1	...	...
334	B0.7 V	✓	a	16.26	−0.06	266.2	17.3	B	P93-0050	...
335	B2.5 III	...	a	16.29	0.18	248.7	2.2	2	P93-0053	...
336	B1 V	✓	f	15.92	0.00	266.7	14.7	B	P93-0075	B1:: V: [P93]
337	B2: V-IIIe+	✓	e	16.72	0.14	278.6	11.1	B	P93-0076	O9:: V: [P93]
340	B0.7 V	...	f	16.89	0.24	251.7	16.2	2	P93-0088	...
342	B1 V	✓	a	16.94	−0.04	292.2	43.4	B	P93-0097	...
343	B1-1.5 V	...	f	16.45	0.04	240.5	9.3	2	P93-0099	...
347	B0 V	...	a	16.68	0.01	267.5	2.5	1	P93-0116	Walborn et al. (2014)
348	B0.7 V	...	a	16.27	0.04	267.8	4.0	2	P93-0118	...

Table 7. continued.

VFTS	Spectral type	Mult.?	Hα	V	$B-V$	v_r [km s^{-1}]	σ	Set	Alt. ID	Comments
349	B1 V	...	f	16.50	−0.03	269.4	7.7	2	P93-0125	...
351	B0.5 V	✓	a	15.98	0.08	246.8	24.9	B	P93-0136	...
353	B2 V-III	...	a	16.60	0.13	292.7	3.3	1	P93-0138	...
354	B0.5: Vn	...	a	15.91	0.00	250.7	12.3	2	P93-0141	...
358	B0.5: V	...	f	16.87	0.00	164.7	10.7	2	P93-0158	B0.2: III [B99]
359	B0.5 V	✓	f	16.30	0.03	295.0	10.5	B	...	...
362	B1-3 V-III	...	e?	16.98	0.44	...	...	...	P93-0176 (at ∼0.″5)	Poss. broad, weak Hα em. (but strong nebular)
363	B0.2 III-II	...	a	14.88	−0.07	264.1	2.9	1	Mk 60, P93-0195	B0 I [Mk]; O9.7 II [WB97]
364	B2.5: V	✓	f	16.82	0.03	266.6	29.9	B	P93-0193	...
365	B2 V	...	f	16.24	−0.02	270.0	10.9	2	...	...
366	B1-1.5 V	...	f	16.83	−0.02	...	...	...	P93-0202	...
367	B1-2 Vn	...	a	15.92	−0.04	269.4	6.0	2	P93-0207	B1 V [B99]
368	B1-3 V	...	f	16.68	0.01	229.6	12.4	2	...	...
374	B0 V(n)	✓	a	16.36	0.19	291.5	21.7	B	...	...
375	B0.5: V	✓	a	16.20	0.02	296.4	22.1	B	...	...
376	B1: V	...	f	16.33	0.04	271.6	7.2	1	P93-0260	B0.5: V [B99]
377	B0-0.5 V	✓	f	16.83	0.11	...	...	...	...	...
378	B1.5: V	...	f	16.98	0.26	...	...	...	P93-0271	...
381	B1.5 V	...	a	16.11	0.07	242.1	8.0	1	P93-0280	'Star 4' in P93-293/304 field from Walborn et al. (2002b)
383	B0.5: V	✓	a	16.10	0.20	224.5	64.2	B	...	...
384	B0 V-III	...	a	16.72	0.49	264.8	5.5	1	P93-0287	B2 V [B99]
387	B1-2 IIIe+	...	e	15.58	0.10	286.3	24.2	2	...	...
388	B0.5 V	✓	a	16.42	0.06	276.4	9.5	B	P93-0305	B0-0.5 V [B99]
391	B0.5: V	✓	f	16.32	−0.02	...	...	...	...	...
394	B0.7 V	...	f	16.93	−0.03	239.4	8.9	2	...	...
395	B1:e	...	e	16.95	−0.18	...	...	...	...	Cross-cont. of fibre (on-sky) by VFTS 402; prob. broad shallow Hα em.
396	B0.5 V	✓	a	16.32	0.11	270.9	17.7	B	...	...
397	B1-2 V	...	a	16.68	0.01	276.7	13.2	2	P93-0338	B0.5-1.5 V [B99]
401	B1-2 IIIe+	...	e	15.48	0.17	269.7	23.3	2	...	...
403	B1-2 V	...	f	17.12	0.19	251.2	3.4	2	P93-0364	...
407	B0.5: V	...	f	16.97	0.08	...	...	...	...	Strong, structured Hα nebular emission; poss. (not prob.) stellar em.
408	B2: V-IIIe+	...	e	16.32	0.02	...	...	...	P93-9011	...
411	B1-3 V-III	...	f	16.93	−0.09	...	...	...	...	Strong, structured Hα nebular emission; poss. (not prob.) stellar em.
413	B2 V	...	a	16.48	0.02	283.5	4.4	1	...	...
414	B1-3 V-III	...	f	16.89	0.03	264.2	11.6	2	...	...
417	B2 Ib	...	f	15.51	0.34	260.7	12.5	1	...	...
420	B0.5 Ia Nwk	...	f	13.02	0.25	273.1	3.4	1	Mk 54, P93-0488	B0.5 Ia [Mk & W86]; B0.5-0.7 Ia [WB97]
421	B2: V	...	f	16.42	−0.04	265.8	4.8	2	...	...
423	B1 Ia: Nwk	...	e?	13.51	0.43	278.3	4.3	1	Mk 52, P93-0493	B1 Ia [Mk & W86]; BC1 Ia [WB97]; prob. P-Cyg-like intrinsic emission
424	B9 I$^+$p	...	e?	11.74	0.33	263.2	2.6	1	R138	A0: I: [F60], A0 I [W84]; A0 Ia [Mk]; prob. intrinsic Hα emission
425	B0.5: V	...	f	16.50	0.06	276.2	13.6	2	...	...
426	B1.5 V	...	f	17.04	0.06	270.7	7.6	1	P93-0511	...
428	B0.5 V	...	f	16.19	0.01	286.5	8.5	2	P93-0525	B0-1: I [B99]
430	B0.5 Ia$^+$((n)) Nwk	✓	e	15.11	0.64	218.3	48.7	B	P93-0538	B0-1 III [WB97]; B0.2 III-I [B99]
431	B1.5 Ia Nstr	...	e?	12.05	0.11	270.2	2.4	1	R137, P93-0548	B0.5 Ia: [F60], B0.7-1.5 [W84]; B1 Ia [Mk]; poss. intrinsic Hα emission
433	B1-3 V-III	...	f	16.87	0.05	...	...	...	P93-0560	Strong, structured Hα nebular emission; poss. (not prob.) stellar em.
434	B1.5: V	✓	f	16.13	0.16	...	...	...	P93-0572	...

Table 7. continued.

VFTS	Spectral type	Mult.?	Hα	V	$B-V$	v_r [km s^{-1}]	σ	Set	Alt. ID	Comments
438	B1-3 V	...	f	16.99	0.07	...	...	...	P93-0591	...
442	B1-2 V	✓	a	16.66	0.08	...	...	...	P93-0616	...
447	B2 V	...	a	15.79	−0.15	264.6	5.8	2	...	...
448	B1-3 V	...	f	16.85	0.33	267.0	9.2	2	P93-0632	...
449	B1-2 V	...	f	16.91	0.03	265.8	12.3	2	...	...
452	B1-2 V	...	a	16.44	−0.04	265.4	4.0	1	...	...
453	B0.5 V	...	a	15.31	−0.03	264.4	1.3	2	P93-0668	B0 III [WB97]; B0.2 V [B99]
458	B5 Ia$^+$p	...	e?	12.67	0.60	276.3	2.1	1	Mk B, P93-0662	A0 Ia [Mk]; BN6 Iap [WB97]; poss. intrinsic Hα em.
459	B2 V	✓	a	16.39	0.01	260.5	10.9	B	P93-0684	B0: I [B99]
461	B1.5 V	...	a	16.83	−0.58	275.2	10.9	2	...	...
462	B0.5-0.7 V	...	a	16.27	−0.52	...	...	...	P93-9013	B2: V [P93]
463	B0.7-1.5 V	...	f	16.92	−0.03	279.8	4.7	2	...	...
467	B1-2 Ve+	...	e	16.91	0.38	322.3	30.2	2	...	...
469	B0 V	...	f?	16.09	0.00	275.6	2.6	1	P93-0714	Broad, shallow Hα em. (likely cross-contamination from VFTS 507)
471	B1 V	...	a	16.36	−0.10	267.0	11.2	1	...	...
473	B2: V	...	f	16.85	−0.02	257.1	19.3	2	...	...
474	B0.5: V(n)	...	a	16.67	0.07	264.1	14.0	2	...	...
478	B0.7 V-III	...	a	16.72	0.32	272.2	3.3	1	P93-0738	B2 Ia [B99]
480	B0.5: V	...	f	16.94	0.43	278.3	4.6	1	...	...
485	B1.5 V	...	f	16.90	−0.05	275.4	4.8	2	...	...
486	B1-2ne+	...	e	15.48	0.28	280.0	15.6	2	...	...
489	B1 Vn	...	f	16.54	−0.07	268.9	15.1	2	P93-9018	...
496	B0 Vn	✓	a	16.66	0.22	279.9	14.2	B	...	Walborn et al. (2014)
499	B0.7 V	...	f	16.77	0.06	293.1	10.1	2	P93-0848	O9-B0: V [B99]
501	B0.5 V	✓	a	15.74	0.08	287.2	68.8	B	P93-0849	O9-B0 V [B99]
504	B0.7 V	...	f	16.27	0.61	251.4	14.2	1	P93-0861	...
516	B1.5 V	...	a	16.61	0.03	256.8	10.9	1	...	...
520	B1: V (SB2?)	✓	a	16.69	0.08	278.2	73.5	B	...	...
523	B1-3 V-III	...	f	17.05	0.01	271.0	6.9	2	P93-0909	...
525	B0 Ia	✓	f	13.76	0.16	289.6	9.5	B	Mk 38, P93-0930	O9 I [Mk]; O9.7 Iab [W86]; OC9.7 Ib [WB97]; Walborn et al. (2014)
533	B1.5 Ia$^+$p Nwk	...	q	11.82	0.29	254.7	4.4	1	R142, P93-0987	B [F60]; B0.5-0.7 I [W84]; B0 Ia [Mk]
534	B0 IV	✓	a	15.66	0.21	278.2	23.1	B	...	...
535	B1-2 V-III	...	f	16.53	0.34	271.1	7.5	1	P93-0995	...
540	B0 V	...	f	16.55	0.23	247.0	2.7	1	...	Walborn et al. (2014)
541	B0.5 Ia Nwk	...	q	13.12	0.13	269.6	3.1	1	P93-9024	B0.5 Ia [P93]
547	B3-5 V-III	...	f	16.79	0.03	255.9	10.3	2	P93-9026	...
548	B0-0.5 V	✓	a	16.13	−0.02	279.9	8.5	B	...	...
551	B1 V	...	f	16.82	0.13	284.7	7.1	2	...	...
553	B1 V	...	a	17.00	0.06	276.3	4.6	1	...	...
556	B1.5-2 V	...	f	16.88	0.04	260.5	10.2	2	...	...
558	B3 III	...	a	16.69	0.01	...	...	...	P93-9028	B1:: V [P93]
567	B1 V(n)	...	f	16.29	0.24	272.1	13.3	2	P93-1155	B0.2 III [B99]
568	B0.5: V	...	f	16.79	0.15	280.3	6.9	2	P93-1172	...
572	B1 V	...	a	16.38	0.15	249.4	4.1	1	P93-1160	B1: III: [B99]
573	B0-0.5 V	...	f	16.94	0.03	...	...	...	...	...
575	B0.7 III	✓	ae?	15.11	0.02	263.4	24.9	B	P93-1191	B0.2-1 III-IV [B99]; broad Hα abs. with embedded double-peaked em.?
576	B1 Ia Nwk	✓	e?	15.67	0.78	262.0	34.9	B	...	Prob. intrinsic Hα emission

Table 7. continued.

VFTS	Spectral type	Mult.?	Hα	V	$B-V$	v_r [km s^{-1}]	σ	Set	Alt. ID	Comments
578	B1.5 Ia Nwk	...	f	14.52	0.40	274.5	4.9	1	P93-1184	B1 Ia [WB97]; B1: II-I [B99]
580	B0-0.5 Vn	...	a	16.62	0.05	283.3	2.6	2	P93-1217	O9.5-B0.5 V [B99]
584	B1.5 V	...	f	16.95	0.05	253.3	5.7	2	...	...
589	B0.5 V (SB2?)	✓	a	15.83	0.15	314.5	94.0	B	P93-1247	B2-3 III [WB97]; B0.5 IV [B99]
590	B0.7 Iab	...	q?	12.49	0.22	254.1	6.2	1	R141, P93-1253	B0.5: [F60]; B0.5 I [W86]; BN0.5 Ia [WB97]
591	B0.2 Ia	✓	q?	12.55	0.23	277.7	8.8	B	Mk 12, P93-1257	B0.5 Ia [Mk]; B0-0.5 Ia [W86]; B0 Ia [WB97]
593	B2.5 V	...	f	16.84	0.09	291.5	3.7	1	...	...
598	B0.2 V	...	f	16.94	0.34	259.4	3.0	1	...	...
600	B0.5 V(n)	...	a	16.40	−0.04	279.8	18.4	2	...	...
602	B0.7 V	...	f	16.71	0.09	301.0	1.6	2	P93-1326	...
605	B1-2 V	...	f	16.85	−0.13	278.6	26.3	2	...	...
606	B0-0.5 V(n)	✓	a	16.60	0.06	265.6	10.3	B	...	...
610	B0 Vn	...	a	16.73	0.17	245.8	8.4	2	P93-1354	B0-0.2 III [B99]
612	B0.5-0.7 V	...	a	16.53	0.20	...	...	...	...	...
616	B0.5: V	...	a	16.48	0.09	227.4	10.7	1	P93-1389	B1: V:: [B99]
618	B1-3 V	...	f	16.70	0.38	...	...	...	P93-1395	...
623	B0.2 V	...	a	16.10	0.14	268.5	1.9	1	P93-1419	B1 III [WB97]; B0-0.2 III-I [B99]
624	B0.2-0.5 Vn	...	f	16.98	0.11	265.3	4.9	2	...	...
625	B1.5 V	...	f	16.91	0.11	310.7	9.2	1	P93-1418	...
628	B0.5: V	✓	f	16.64	0.09	250.8	62.7	B	...	...
629	B1-2 Ve+	...	e	16.78	0.07	265.1	19.9	2	...	...
632	B2 Vn	...	a	15.97	0.12	284.7	11.1	2	P93-1460	B0-2 V [B99]
633	B1 V	...	a	16.50	0.19	274.0	7.2	2	P93-1464	...
636	B0 Vn	...	a	16.53	0.06	241.5	5.2	2	...	...
637	B1-2 V + Early B	✓	a	16.61	0.04	299.3	32.3	B	...	...
640	B2 V	...	f	16.82	0.16	256.0	5.0	2	P93-1489	...
641	B0.5: I	...	–	13.09	0.16	...	...	...	Mk 11; P93-1500	B0.5 Ia [Mk]; B0-0.5 Ia [W86]; B0 Ib [WB97]; B0.2 III [B99]; see discussion in Paper I
643	B1.5 V	...	a	16.41	0.13	250.9	8.2	2	P93-1508	...
644	B1-2 Ve	...	e	16.62	0.15	248.6	20.2	2	...	...
646	B0.5 III(n)	...	e?	14.94	0.14	263.9	4.8	2	P93-1527	B1 III [WB97]; B1 IV [B99]; prob. broad Hα em. shoulders
650	B1.5 V	...	f	16.98	−0.10	286.2	3.0	1	...	...
653	B0-0.5 V	...	a	16.63	0.22	...	...	...	P93-1554	O9: III:p [P93]
659	B0-0.5 V(n)	...	a	15.96	0.04	264.9	4.6	2	P93-1584	B0: V: [P93]; B0-1 V [B99]
662	B3-5 III:	✓	f	16.12	0.08	251.3	39.1	B	...	...
665	B0.5 V	✓	ae?	16.43	0.11	274.2	16.1	B	P93-1604	B1 V [B99]; broad Hα abs. with prob. embedded double-peaked em.
666	B0.5 V	...	a	16.42	−0.08	255.5	2.1	1	P93-9036	...
668	B0.7 V	...	a	16.60	0.10	269.2	2.3	1	P93-1611	...
670	B0.7 V	...	a	16.02	0.15	286.1	13.8	2	P93-1621	B0.5-1 III [WB97]; B0.2-0.5 III [B99]
671	B0.7 V	...	a	16.43	−0.11	255.3	13.3	2	...	...
672	B0.7 II Nwk?	...	e	14.59	0.23	279.5	3.2	1	P93-1661	B0.7 Ia [WB97]; B1 III [B99]
673	B1 V	...	f	16.98	0.03	277.1	1.5	1	P93-1664	...
675	B1 Iab Nwk	✓	f	14.48	0.28	276.7	23.8	B	P93-1674	B0.5-0.7 I [WB97]; B1 Ib [B99]
676	B0.7 V	...	a	16.52	0.07	272.1	18.7	2	P93-1686	...
678	B1: V	...	a	16.95	0.41	270.2	11.2	2	P93-1689	...
681	B0.7 V	...	f	16.55	0.06	264.0	14.5	1	P93-1714	...
683	B2 Ve	...	e	16.33	−0.10	271.1	15.7	2	...	Broad, shallow Hα em. shoulders

Table 7. continued.

VFTS	Spectral type	Mult.?	Hα	V	$B-V$	v_r [km s^{-1}]	σ	Set	Alt. ID	Comments
684	B1-1.5 V	...	f	16.91	0.13	278.6	13.1	2	P93-1722	...
685	B1-3 V-IIIe+	...	e	16.64	0.21	243.4	22.5	2	...	...
686	B0.7 III	✓	a	14.99	0.17	276.8	38.9	B	...	B0.5 III [WB97]; B1 II-III [B99]
687	B1.5 Ib((n)) Nwk	✓	a	14.29	0.28	295.8	23.0	B	P93-1737	B1 Iab [P93]; B1 Iab [WB97]; B1.5 III [B99]
689	B3:e (shell)	...	e	16.51	0.08	...	...	...	P93-1763	...
690	B0.2 V	...	a	16.46	0.09	272.7	14.7	1	P93-1772	...
692	B0.2 V	...	f	16.17	0.05	271.2	2.5	1	P93-1786	...
696	B0.7 Ib-Iab Nwk	...	q?	12.73	−0.02	265.8	2.3	1	Sk−68° 140; BE74-422	...
697	B1-2 Ve	✓	e	16.55	0.18	263.7	8.3	B	P93-1799	...
698	Mid B + Early B	✓	e	13.68	0.44	...	...	...	Mk 02, P93-1797; AL-377	Discussed in detail by Dunstall et al. (2012)
699	B0.2-0.5 Vn	...	f	16.19	−0.05	264.4	12.0	2	P93-1805	...
701	B0.7 V	...	f	16.60	0.26	266.6	10.1	2	P93-1820	...
705	B0.7 V	✓	a	16.43	0.07	268.3	80.8	B	P93-1834	...
707	B0.5 V	...	a	15.59	0.07	275.0	2.0	1	P93-1840	B1 V [P93]
709	B2.5: V	...	a	16.58	−0.07	265.5	6.5	2	P93-9041	...
712	B1 V	...	a	16.13	0.21	255.1	10.9	1	P93-1859	...
713	B2: V	✓	a	16.68	0.25	250.6	38.7	B	P93-1868	...
714	B1 Ia: Nwk	...	f	15.57	0.33	283.4	1.9	1	P93-1875	B0:: V: [P93]
715	B1 V	✓	f	16.64	−0.10	270.0	22.1	B	P93-9043	...
718	B2.5 III	✓	f	15.99	−0.06	306.8	16.2	B	...	...
719	B1 V	✓	f	17.00	0.08	265.0	18.9	B	P93-1898	...
720	B2 V	...	f	16.74	−0.06	298.4	4.8	2	...	...
723	B0.5 V	✓	a	16.19	0.16	239.2	26.3	B	P93-1955	...
725	B0.7 III	...	a	15.84	0.11	285.3	1.8	1	P93-1961	...
726	B1-2 V	...	a	16.40	0.03	249.7	12.1	2	...	...
727	B3 III	...	a	16.74	0.18	272.9	3.0	1	...	...
729	B0.2 III	...	a	14.97	0.25	268.6	10.9	1	P93-1969	O9-B0 III [WB97]; B0.7 IV [B99]
730	B1 IV(n)	✓	a	15.41	−0.10	326.5	6.8	B	P93-9045	B1.5 [P93]
732	B1.5 Iap Nwk	...	q?	13.03	0.19	267.3	1.4	1	Mk 01, P93-1987; BI 256	B1 Ia [Mk]; B2 I [B99]
734	B0.7 V	...	a	16.31	0.15	263.7	8.9	2	P93-1991	...
735	B1-2 IIIe+	...	e	16.30	0.43	268.9	4.9	1	...	...
738	B0.5 IIIe+	...	e	14.55	0.02	284.4	14.1	2	...	...
739	A0 Ip	...	e	12.26	0.31	250.5	1.9	3	Sk−69° 250	Weak double-peaked Hα em.
740	B0.7 III	...	a	16.50	0.35	267.3	1.9	1	...	...
741	B2 V	...	a	16.97	0.29	263.2	10.9	2	...	...
742	B2 V	✓	a	16.93	−0.02	...	...	...	...	...
745	B2.5 II-Ib	...	f	16.59	0.28	275.7	3.7	1	...	...
747	B0.5 V	...	e?	15.28	0.12	270.2	2.5	2	P93-2022	B0.5: V [P93]; prob. broad, shallow Hα em. shoulders
748	B0.7 V	...	a	16.78	0.16	260.4	3.6	1	P93-2023	...
749	B0.7 V	...	a	16.76	0.13	264.8	7.2	2	P93-2025	...
752	B2 V	✓	a	16.48	−0.12	258.8	40.3	B	...	...
754	B1.5 V	...	a	16.55	0.26	240.2	4.0	2	P93-2036	...
756	B0.5 IIIe+	...	e	14.59	0.06	281.6	13.5	1	AL-382; BE74-424	...
757	B3 III(n)	...	f	16.78	0.26	273.4	6.3	2	...	...
762	B1.5 V	...	a	16.46	0.22	259.0	12.6	1	...	...
766	B5-8e	...	e	15.34	−0.07	253.2	4.0	3	...	...
772	B3-5 V-III	...	a	16.89	−0.01	253.7	6.1	1	...	...

Table 7. continued.

VFTS	Spectral type	Mult.?	Hα	V	$B-V$	v_r [km s^{-1}]	σ	Set	Alt. ID	Comments
779	B1 II-Ib	✓	a	15.46	0.19	258.9	27.2	B	…	…
780	B1.5 V	…	f	16.73	−0.11	243.4	11.4	2	…	…
781	B0.7: V-IIIe+	…	e	15.66	0.32	272.7	11.5	2	…	…
784	B1: V	✓	f	16.83	0.19	312.4	27.6	B	P93-2151	…
786	B1-2 IIIe+	…	e	16.53	0.27	274.0	12.0	2	…	…
788	B1 III	✓	a	16.15	0.09	280.7	27.8	B	…	…
789	B0.5-2 V	…	a	16.88	0.21	263.6	15.5	2	…	…
792	B2 V	✓	a	15.96	−0.06	278.3	8.0	B	…	Poss. broad, weak Hα shoulders
794	B1-2 V-IIIe+	…	e	15.80	0.04	278.9	12.1	2	…	…
795	B1 III	…	a	16.35	0.41	270.1	9.0	1	…	…
796	B1-2 Ve+	…	e	16.89	0.00	284.9	6.9	2	…	…
798	B1 V	…	a	16.71	0.44	247.1	19.5	2	…	…
799	B0.5-0.7 V	✓	f	16.86	0.10	270.7	7.3	B	P93-2210	…
800	B1-2 IIIe+	…	e	15.89	0.24	268.9	17.2	2	…	…
801	B1.5 V	…	f	15.94	−0.07	278.0	9.7	1	…	…
804	B2: V	…	f	17.03	0.05	256.5	9.0	2	…	…
811	B2 V	…	a	16.56	−0.08	277.4	10.7	1	…	…
813	B2.5 Ve	…	e	16.54	−0.06	274.5	7.1	2	…	…
814	B2.5 V	…	a	16.81	0.05	271.6	9.1	1	…	…
815	B1.5 V	…	a	16.68	0.19	255.7	5.4	2	…	Member of SL 639
817	B1 III-II	…	a	15.53	0.17	251.9	11.8	1	P93-2252	B1.5 Ia [P93]
821	B0 V-IV	✓	f	16.03	−0.14	…	…	…	…	…
822	Mid-late B[e]	…	p	15.60	0.37	…	…	…	…	Discussed in detail by Kalari et al. (2014)
823	B2-3 III:e	…	e	16.06	0.17	262.0	8.2	2	…	Member of SL 639
824	B1.5-2 Ve	…	e	16.36	0.36	245.9	12.4	2	…	Member of SL 639
825	B1.5-2 V-IIIe	…	e	16.20	0.33	252.9	15.6	2	…	Member of SL 639
826	B1 IIn	…	e	14.85	0.17	242.8	9.0	2	…	Member of SL 639
827	B1.5 Ib	✓	f	15.34	0.31	254.3	14.4	B	…	Member of SL 639
829	B1.5-2 II	…	a	15.13	0.41	261.4	4.9	1	…	Member of SL 639
831	B5 Ia	…	q?	13.04	0.29	210.4	6.2	1	…	Member of SL 639; poss. Hα abs. plus nebular em.
832	B1 V	…	a	16.50	0.37	263.6	8.5	2	…	Member of SL 639
833	B1-3 V	…	a	16.96	0.22	277.0	5.9	2	…	…
834	B1.5 III	✓	a	15.19	0.33	240.3	22.1	B	…	Member of SL 639
835	B1 Ve	…	e	–	–	251.9	3.4	1	…	Member of SL 639
836	B1.5 IIIe	…	e	15.71	0.18	253.3	1.4	2	…	Member of SL 639
837	B1 V	✓	a	16.07	−0.09	282.5	27.0	B	…	…
838	B1: II(n)	…	a	15.81	0.28	263.4	4.5	2	…	…
840	B1.5: Ve	…	e	16.74	0.24	236.7	8.9	2	…	Member of SL 639; spurious Si II abs.?
841	B2.5 Ia	…	a	15.83	0.89	258.0	3.0	1	…	…
842	B1-2 IIIe+	…	e	16.29	0.33	244.8	34.7	2	…	Be [Paper I]; member of SL 639
845	B1 II	…	a	15.30	0.15	259.9	1.4	1	P93-2305	B1 III [P93]
846	B2.5 V	…	f	16.78	0.11	258.4	4.4	2	…	…
847	B0.7-1 IIIne	✓	e	15.48	−0.06	298.7	9.6	B	P93-2313	B0.5: V [P93]; broad Hα em. shoulders
848	B1.5 IIIe+	…	e	15.54	0.25	247.7	4.6	2	…	…
850	B1 III	✓	a	16.15	0.18	256.9	11.6	B	…	…
851	B2 III	…	f	15.83	−0.09	229.4	0.3	1	…	…
853	B1-2 Ve+	…	e	16.78	0.33	258.9	15.1	2	…	…

Table 7. continued.

VFTS	Spectral type	Mult.?	Hα	V	$B-V$	v_r [km s^{-1}]	σ	Set	Alt. ID	Comments
854	B1-3 V-IIIe+	...	e	16.28	0.10	...	...	...	...	...
855	B3 Ib	...	a	15.34	0.27	248.8	3.0	1	...	...
857	B1.5 V	...	a	16.26	0.17	255.4	3.8	2	...	...
860	B1.5 V	...	f	16.67	0.13	252.6	3.0	1	...	...
864	B1.5 V	...	f	16.64	−0.05	278.2	4.6	1	...	...
866	B1.5 V	...	a	16.24	−0.12	261.8	5.7	1	...	...
867	B1 Ib Nwk	...	a	14.63	0.13	275.7	2.7	1	BI 261	...
868	B2 V	...	a	16.65	0.27	261.5	2.3	1	...	...
869	B1-1.5 V	...	a	16.76	0.05	288.8	6.4	2	...	...
872	B0 V-IV	...	a	16.09	−0.07	285.5	6.9	1	...	...
874	B1.5 IIIe+	✓	e	15.37	0.02	274.9	8.3	B	...	...
875	B2 V	...	f	16.46	−0.02	252.7	8.3	2	...	...
876	B3-5 III(n)e	...	e	16.30	0.00	251.0	9.5	2	...	...
877	B1-3 V-IIIe+	✓	e	16.36	0.18	236.7	11.2	B	...	...
879	B3 V-III	...	f	16.73	0.11	275.7	4.9	1	...	...
880	B1-2 Ve (shell)	...	e	16.66	0.06	270.4	18.7	2	...	...
881	B0.5 III	...	a	15.66	−0.06	283.0	1.5	1	...	...
882	B0 V(n)	...	a	15.96	−0.10	283.3	9.4	2	...	...
883	B0.5 V	✓	a	16.49	0.13	...	...	B	...	...
885	B1.5 V	...	a	15.90	0.01	264.0	5.4	1	...	...
886	B1 V	...	f	16.82	−0.04	258.4	5.5	1	...	...
888	B0.5 V	✓	a	16.18	−0.07	238.3	50.8	B	...	...
889	B1-2 Ve	...	e	16.56	0.37	263.1	12.1	2	...	...
890	B2 V	✓	a	16.13	0.02	...	...	B	...	...
891	B2 V	✓	a	16.48	0.07	273.6	8.3	B	...	...

Appendix A: Ancillary material

A.1. Spectral montages

To illustrate the spectral sequences as a function of luminosity class, examples of VFTS B-type spectra are shown in Figs. A.1–A.3. The principal lines used in classification, as summarised in Tables 1 and 2 are indicated in each figure. Luminosity sequences at spectral types B0.2, B1 and B2.5 are shown in Figs. A.4–A.6, respectively. For clarity, the spectra in all six figures have been smoothed and rebinned to an effective resolving power of $R = 4000$.

A.2. Detailed velocity estimates

For completeness, we list the individual velocity estimates from each line, calculated using the rest wavelengths given in Table 3. Tables A.1 and A.2 present the results for stars using the Set 1 and Set 2 diagnostic lines, respectively; results for the binary stars (following the discussion outlined in Sect. 4.2) are given in Table A.3.

A.2.1. Comparison with published velocity estimates

The methods and line sets adopted to estimate radial velocities (v_r) for the B-type stars differ to those employed by Sana et al. (2013) for the O-type objects from the survey. As a consistency check between the two studies, we analysed 45 of the apparently-single, late O-type stars (with O9.5 and O9.7 types) and compared our velocity estimates with those from Sana et al. We find a mean and standard deviation between the two methods of $\Delta v = 0.5 \pm 6.2$ km s^{-1} (where $\Delta v = v_r - v_{\rm Sana}$).

The differential results (Δv) for the 45 stars are shown in Fig. A.7 (with the standard deviations added in quadrature). For the purposes of global analysis of the sample and identification of potential runaways, these results are in excellent agreement. As a further check of any systematic trends arising from the different methods, the lower panel of Fig. A.7 shows the same differential velocities, but now as a function of estimated $v_e \sin i$ (from Dufton et al. 2013); no obvious systematic difference is present.

A.3. Centre-of-mass velocities

We have investigated the expected differences between our mean values and centre-of-mass velocities using a Monte Carlo technique. We assumed a sinusoidal velocity curve (i.e. circular orbit) and, adopting the observational sampling of Field A of the survey (Table A.1 of Paper I), we calculated ranges of observed velocities (i.e. $\delta v_{\rm r\,max}$) and their resulting mean velocity. We assumed a random initial phase, and considered periods ranging from one day up to several years.

These simulated mean velocities provide us with an estimate of the expected error compared to the genuine centre-of-mass velocity. For a given period, we can then average these differences over the range of assumed phases to find a typical error. The ratio of this typical error to $\delta v_{\rm r\,max}$ is shown in Fig. A.8. For binaries with periods of $\lesssim$250 d, the expected error is approximately 12–15 % of $\delta v_{\rm r\,max}$, with this increasing for longer periods, and then tending to a value of ~25% for periods $\gtrsim$350 d (greater than the maximum time-sampling of the real data).

These simplistic simulations (e.g. not taking into account potential eccentric orbits) have probably underestimated the uncertainties but, given the observational cadence of the survey, they illustrate that the mean multi-epoch v_r values should provide reasonable estimates of the centre-of-mass velocities for short-period systems ($\lesssim$250 d), which display relatively small peak-to-peak variations.

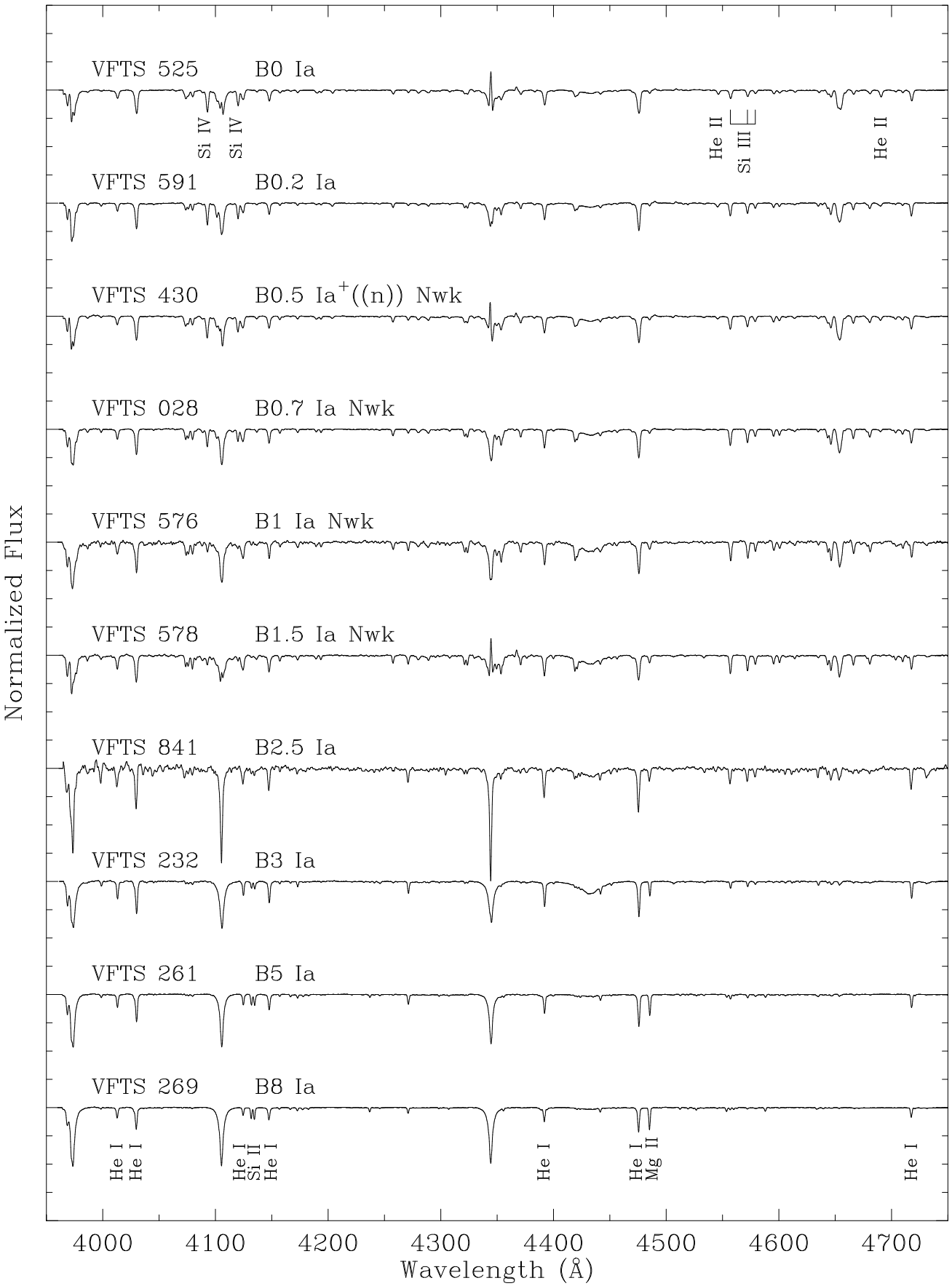

Fig. A.1. Example B-type supergiants (Class Ia). The primary diagnostic lines for spectral classification are identified. In the spectrum of VFTS 525 these are: He II $\lambda\lambda$4542, 4686; Si III $\lambda\lambda$4553-68-74; Si IV $\lambda\lambda$4089, 4116; those identified in VFTS 269 are: He I $\lambda\lambda$4009, 4026, 4121, 4144, 4388, 4471, 4713; Mg II λ4481; Si II $\lambda\lambda$4128-32. The broad λ4428 diffuse interstellar band is also evident in some sightlines.

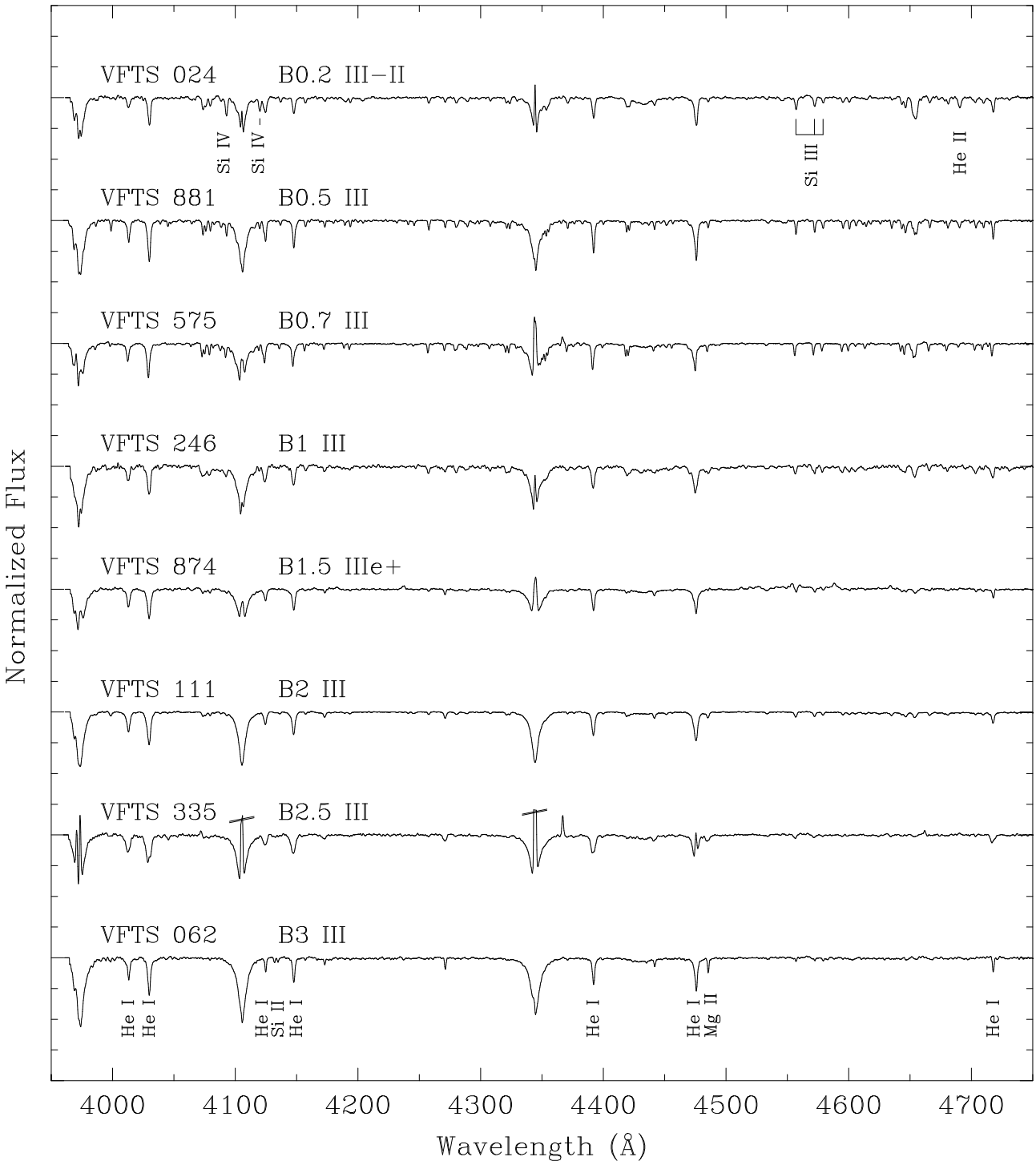

Fig. A.2. Example B-type giants (Class III). The identified lines are the same as those in Fig. A.1; nebular lines have been truncated in VFTS 335 as indicated.

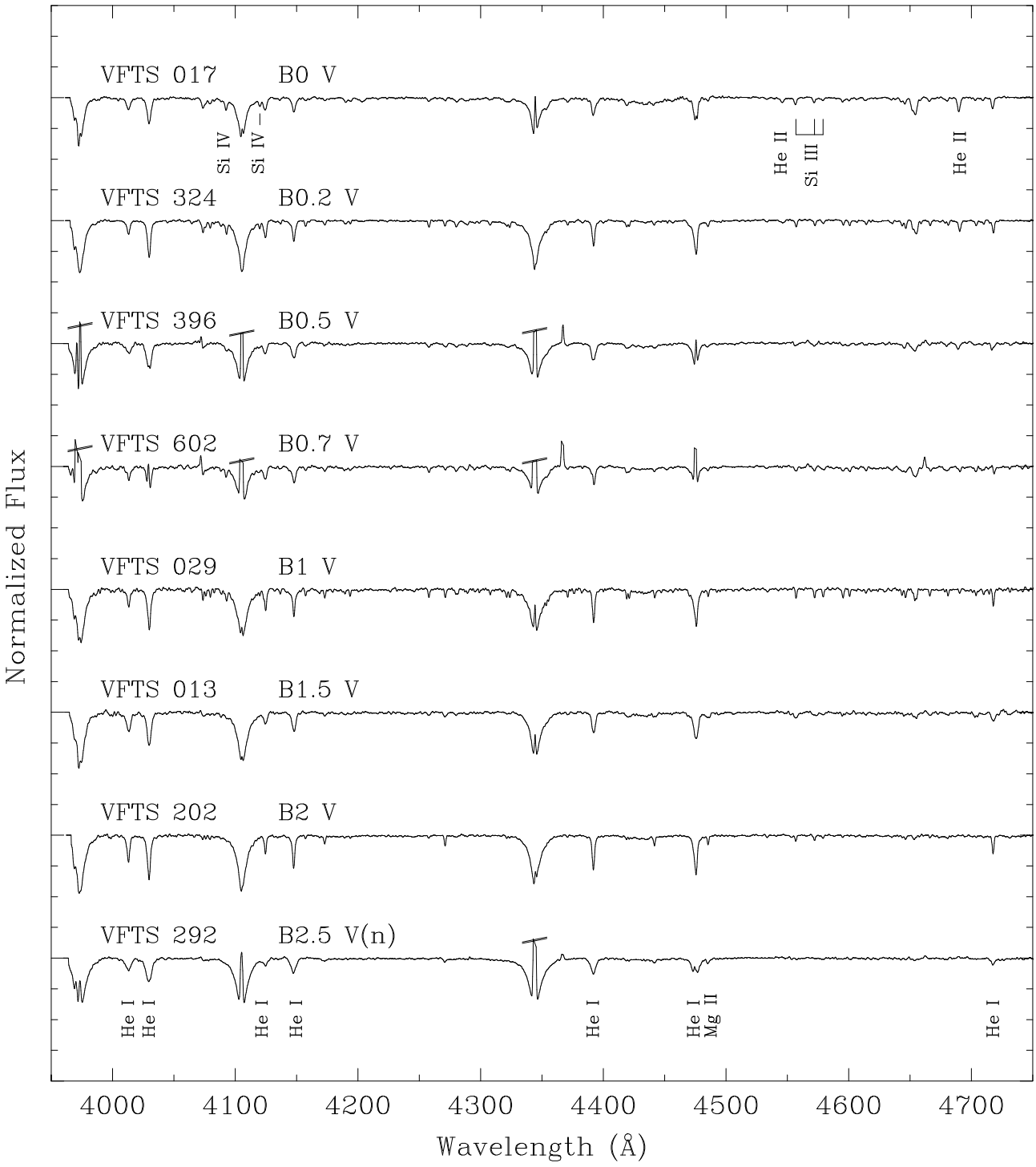

Fig. A.3. Example B-type dwarfs (Class V). The identified lines are the same as those in Fig. A.1; nebular lines have been truncated in three spectra as indicated.

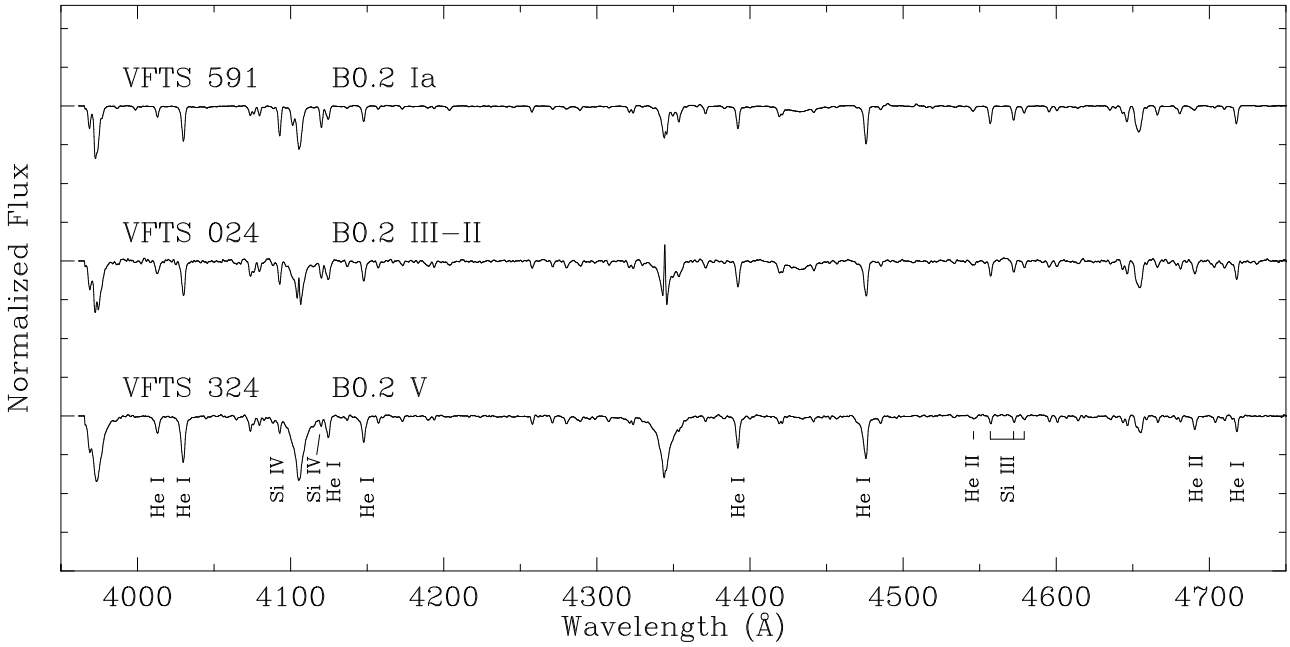

Fig. A.4. Example luminosity sequence at B0.2. The identified lines are the same as those in Fig. A.1; we note the greater intensity of the metallic lines with increasing luminosity (including the C III + O II features at $\sim\lambda$4650).

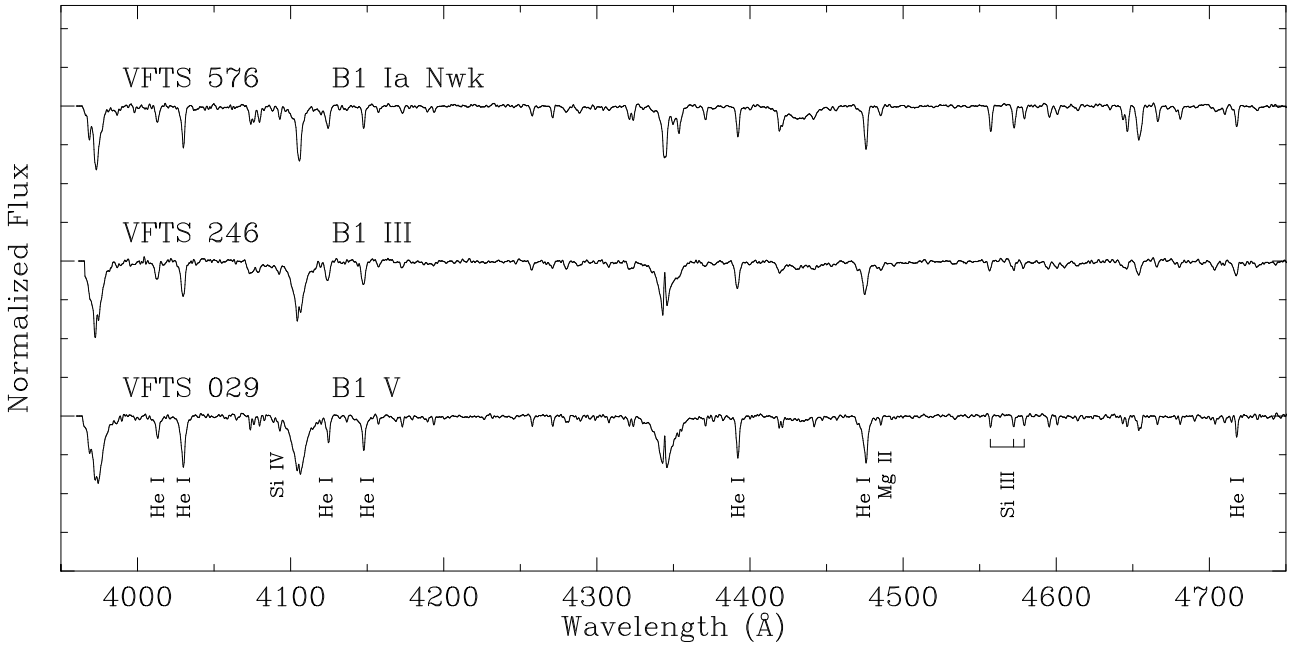

Fig. A.5. Example luminosity sequence at B1. The identified He and Si lines are the same as those in Fig. A.1.

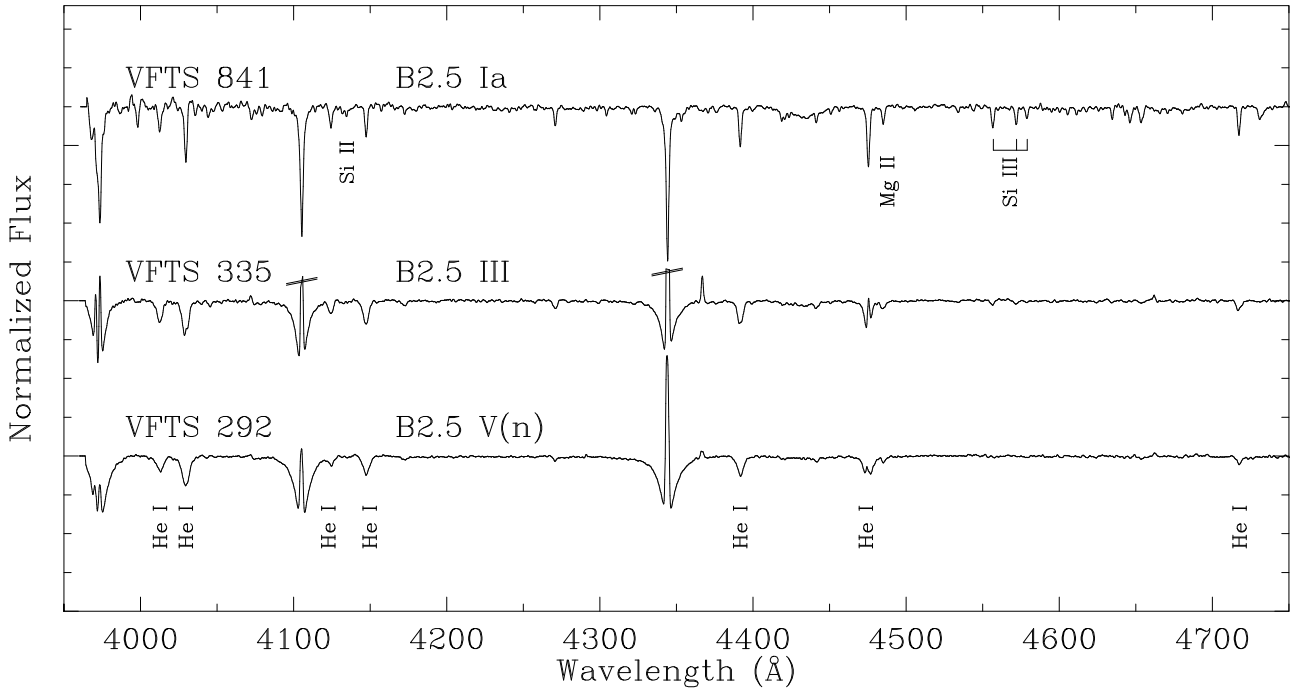

Fig. A.6. Example luminosity sequence at B2.5. The identified He and Si lines are the same as those in Fig. A.1 and the nebular lines have been truncated in VFTS 335 as indicated.

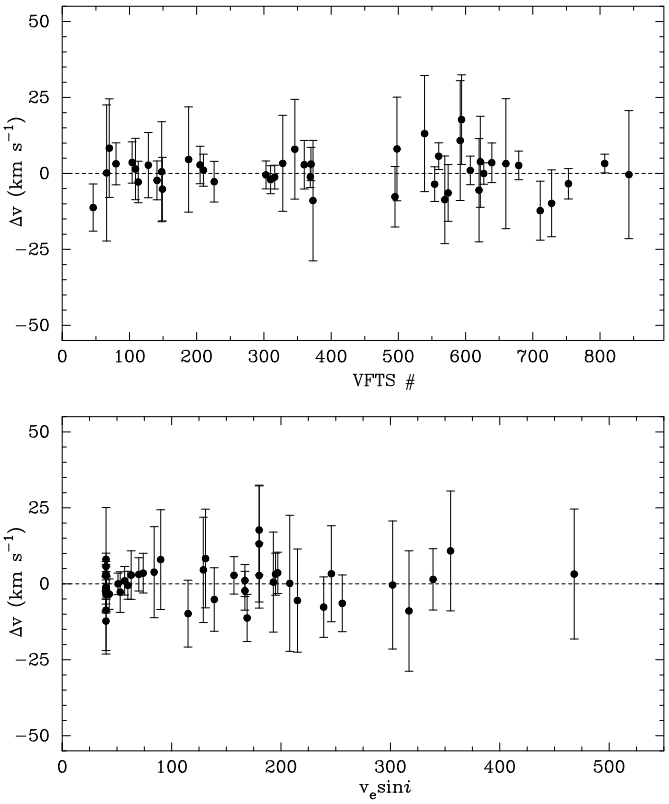

Fig. A.7. Comparison of radial velocities (v_r) estimated using the methods in this paper with results from Sana et al. (2013), in which $\Delta v = v_r - v_{Sana}$, and the plotted uncertainties are the standard deviations of both estimates added in quadrature. The upper panel shows the Δv results in the sequence of VFTS identifiers (i.e. increasing right ascension), while the lower panel shows Δv as a function of $v_e \sin i$.

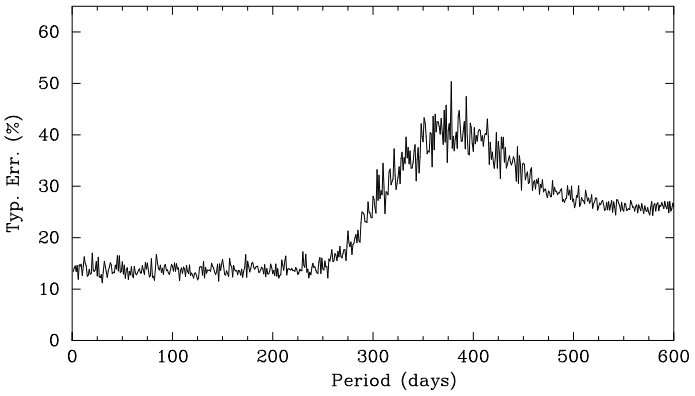

Fig. A.8. Typical errors in the average radial velocities (calculated for the observational sampling of Field A of the VFTS) for simulated binaries compared to their true centre-of-mass velocities (as a percentage of the expected range in radial velocities, δv_{rmax}, see text for details).

Table A.1. Line-by-line radial-velocity estimates for single stars using the Set 1 absorption lines.

VFTS	He I$_{\lambda4121}$	C II$_{\lambda4267}$	He I$_{\lambda4438}$	Si III$_{\lambda4553}$ (LR02)	Si III$_{\lambda4553}$ (LR03)	Si III$_{\lambda4568}$	Si III$_{\lambda4575}$	He I$_{\lambda4713}$	v_r	σ	n
003	268.3	271.3	269.2	265.8	263.9	264.0	264.8	262.8	265.2	2.1	8
010	289.9	...	...	...	281.2	291.5	...	283.7	287.1	3.9	4
024	...	282.8	284.2	279.7	291.2	281.5	285.9	289.7	285.7	4.4	7
028	263.3	280.0	268.0	277.7	273.9	274.2	271.2	275.4	273.5	4.4	8
029	288.0	284.5	289.5	282.7	284.6	280.6	283.0	288.6	285.6	3.0	8
031	275.0	292.6	292.9	271.4	...	...	...	275.5	280.0	8.4	5
034	...	296.6	...	308.7	329.1	297.7	...	...	308.3	13.8	4
044	292.9	285.3	287.6	284.6	271.9	...	...	295.5	288.1	7.2	6
046	242.3	248.5	230.1	238.7	236.0	261.0	...	239.8	242.2	7.6	7
050	282.3	283.8	282.7	279.4	281.4	284.5	282.2	285.7	283.1	2.0	8
052	276.4	278.7	280.7	...	280.5	279.0	279.0	282.4	279.8	2.0	7
053	275.1	277.0	279.2	274.3	278.6	274.4	274.8	278.9	276.4	2.0	8
060	254.9	286.1	299.4	287.5	298.6	295.2	287.9	284.4	284.2	14.3	8
062	289.8	286.1	288.2	282.5	281.6	289.1	285.5	289.5	287.5	2.7	8
069	280.2	285.7	280.1	...	280.1	279.7	278.5	282.6	280.7	1.7	7
075	303.9	292.7	284.1	...	...	278.5	...	307.0	297.2	10.5	5
082	280.1	288.9	282.7	283.8	283.6	281.2	281.5	286.2	283.3	2.4	8
095	293.1	296.5	296.1	...	294.7	284.5	297.7	296.7	294.3	3.8	7
111	268.1	276.7	273.4	269.0	265.4	273.3	270.0	277.4	272.0	4.2	8
113	277.7	276.1	277.0	...	277.5	281.9	...	285.4	280.2	3.7	6
119	...	277.8	281.9	...	272.8	270.3	272.0	278.0	275.8	3.9	6
121	282.5	282.3	285.8	281.3	279.8	282.2	283.5	288.4	283.4	2.8	8
124	289.0	290.1	289.9	285.3	287.1	287.4	287.4	292.6	289.4	2.2	8
126	252.8	252.0	255.3	251.0	251.2	254.0	256.8	258.1	254.1	2.6	8
152	276.7	278.2	274.5	271.5	271.7	268.0	268.7	275.1	274.3	2.9	8
159	265.4	274.9	265.3	264.0	265.0	253.6	283.3	267.7	267.5	6.1	8
161	...	268.5	...	269.1	252.6	...	...	...	262.6	7.9	3
164	...	296.7	...	316.2	292.7	...	...	...	300.4	10.0	3
170	281.6	275.6	280.5	277.3	276.6	275.1	275.8	281.8	278.7	2.7	8
178	287.9	293.5	285.0	286.8	281.9	281.0	279.4	284.6	284.5	3.2	8
183	257.9	...	253.9	255.4	257.0	257.8	251.9	255.6	256.1	1.7	7
186	256.8	280.0	274.5	265.4	254.2	267.7	271.1	268.5	264.3	10.6	8
200	248.6	247.7	...	...	...	...	...	265.6	253.6	8.0	3
202	276.5	274.3	274.9	273.1	275.8	277.5	275.7	280.3	276.6	2.3	8
209	275.7	273.6	275.2	...	268.1	271.3	269.3	274.4	273.1	2.6	7
214	276.6	272.2	275.8	274.9	274.2	273.8	273.7	277.6	275.4	1.7	8
220	...	276.1	...	286.5	282.9	281.2	...	...	282.6	3.3	4
226	...	197.1	182.9	196.6	185.2	186.0	178.6	196.4	191.2	6.5	7
232	290.3	291.0	283.8	287.5	287.2	287.1	282.2	290.1	288.6	2.5	8
234	244.5	...	259.4	246.6	...	285.1	295.5	255.3	260.9	17.3	7
235	266.0	269.5	269.0	262.5	264.3	263.0	262.0	267.4	265.6	2.4	8
237	306.5	279.3	278.6	291.1	279.9	287.8	281.4	282.6	287.9	10.5	8
241	257.0	275.3	268.4	283.7	268.2	260.8	259.0	273.3	267.6	8.7	8
242	215.8	...	218.4	220.6	214.5	217.0	206.0	217.2	216.0	3.6	7
253	272.4	...	269.1	265.3	270.7	...	...	271.8	270.7	2.1	5

Notes. Column entries are: (1) VFTS identifier; (2−10) estimated radial velocities from each line; (11) weighted mean velocity for each star (v_r, from Eq. (1)); (12) standard deviation (σ, from Eq. (2)); (13) number of lines (n) used in calculation of v_r and σ.

Table A.1. continued.

VFTS	He I$_{\lambda4121}$	C II$_{\lambda4267}$	He I$_{\lambda4438}$	Si III$_{\lambda4553}$ (LR02)	Si III$_{\lambda4553}$ (LR03)	Si III$_{\lambda4568}$	Si III$_{\lambda4575}$	He I$_{\lambda4713}$	v_r	σ	n
258	285.5	288.2	299.0	294.7	277.3	281.9	...	289.2	287.3	5.9	7
261	284.1	286.4	280.6	...	282.6	284.2	286.3	287.3	285.0	2.2	7
268	...	...	...	282.0	280.9	249.5	...	...	272.1	14.5	3
269	267.4	269.2	263.8	263.4	262.5	265.5	268.6	268.1	266.9	2.1	8
270	266.3	265.1	263.8	260.9	261.8	262.3	262.9	267.6	264.9	2.3	8
273	256.3	255.9	253.4	254.5	250.9	250.7	238.1	258.5	253.8	4.9	8
276	252.7	256.2	252.1	273.2	258.3	250.7	253.1	261.6	256.8	5.9	8
284	278.4	276.0	278.0	273.2	268.5	267.4	269.5	272.0	272.7	3.9	8
293	259.0	260.6	261.7	257.2	261.7	...	262.8	261.3	260.4	1.9	7
296	...	246.6	243.2	241.8	245.2	...	...	260.5	250.0	7.8	5
297	252.6	252.8	255.7	249.9	250.9	248.0	246.9	252.2	251.7	2.2	8
302	265.1	264.1	266.0	264.0	264.4	262.6	265.2	267.9	264.8	1.6	8
303	269.7	...	272.2	284.8	266.6	266.8	...	269.7	270.5	4.2	6
307	274.2	278.2	273.6	273.9	269.8	270.9	270.9	273.9	272.7	2.0	8
308	264.1	266.0	264.2	261.8	258.7	261.8	...	263.7	263.5	1.9	7
310	272.8	264.2	268.7	269.9	265.4	268.1	269.2	275.4	270.2	3.7	8
313	265.5	269.8	270.5	269.4	271.5	268.7	275.2	274.4	270.7	3.3	8
315	259.5	263.7	261.8	262.1	260.2	261.1	260.6	264.1	261.6	1.5	8
316	269.1	265.3	275.6	267.1	267.0	263.0	270.0	271.9	269.1	3.4	8
331	286.5	274.1	278.6	270.0	277.9	274.7	267.5	289.5	279.4	7.3	8
346	296.8	268.9	260.4	263.4	265.1	268.3	245.7	281.0	274.7	15.4	8
347	267.6	263.3	268.4	265.2	270.7	267.4	273.2	265.8	267.5	2.5	8
353	296.8	290.1	289.8	289.0	290.4	290.8	...	296.7	292.7	3.3	7
360	260.0	...	...	...	269.1	266.2	258.1	...	264.1	4.4	4
363	258.5	262.8	260.3	264.7	264.3	265.9	263.8	267.8	264.1	2.9	8
369	263.0	260.0	263.5	267.1	258.8	259.7	259.0	265.5	262.7	2.9	8
370	237.2	241.5	227.5	231.8	239.5	229.6	223.6	235.6	234.6	4.6	8
376	...	...	...	283.0	266.6	267.4	...	...	271.6	7.2	3
381	246.9	249.6	241.8	246.2	224.0	248.1	...	235.4	242.1	8.0	7
384	275.3	264.8	256.2	264.4	264.4	257.4	259.2	269.1	264.8	5.5	8
413	277.2	286.1	283.7	...	...	...	...	287.7	283.5	4.4	4
417	271.1	258.0	254.5	252.3	251.1	255.0	249.1	285.5	260.7	12.5	8
420	...	280.1	274.5	275.7	271.5	271.6	265.8	274.6	273.1	3.4	7
423	...	275.9	271.8	274.1	282.0	281.0	279.8	285.5	278.3	4.3	7
424	265.1	264.8	259.3	256.9	260.0	265.4	...	264.0	263.2	2.6	7
426	...	...	...	261.8	279.2	274.3	263.4	...	270.7	7.6	4
431	265.2	271.3	266.1	269.3	272.2	271.7	271.3	271.0	270.2	2.4	8
452	268.2	263.8	268.9	263.8	271.3	...	...	259.3	265.4	4.0	6
458	276.3	277.3	274.0	273.1	274.8	275.6	274.6	279.4	276.3	2.1	8
469	277.8	279.1	277.3	273.7	274.5	271.4	270.6	277.0	275.6	2.6	8
471	254.2	271.3	261.9	263.0	268.1	266.0	294.4	274.4	267.0	11.2	8
478	273.4	268.8	267.6	270.8	269.1	270.6	275.5	278.2	272.2	3.3	8
480	...	284.7	...	279.3	279.3	281.8	...	...	278.3	4.6	4
498	278.7	...	...	...	264.0	271.5	279.7	...	273.9	6.3	4
504	240.6	...	...	273.9	...	246.8	276.3	...	251.4	14.2	4
516	262.6	241.1	264.6	273.7	...	...	...	247.7	256.8	10.9	5
533	257.2	260.7	256.0	259.8	252.1	253.4	252.8	246.0	254.7	4.4	8

Table A.1. continued.

VFTS	He I$_{\lambda4121}$	C II$_{\lambda4267}$	He I$_{\lambda4438}$	Si III$_{\lambda4553}$ (LR02)	Si III$_{\lambda4553}$ (LR03)	Si III$_{\lambda4568}$	Si III$_{\lambda4575}$	He I$_{\lambda4713}$	v_r	σ	n
535	...	...	...	...	281.4	266.0	265.1	...	271.1	7.5	3
540	246.3	252.0	240.6	246.9	245.6	251.0	...	246.3	247.0	2.7	7
541	...	274.7	271.6	273.3	265.6	266.8	268.5	271.0	269.6	3.1	7
553	278.8	274.9	277.6	272.1	279.2	284.5	269.7	270.8	276.3	4.6	8
560	263.5	264.3	266.6	263.7	269.5	267.9	...	264.8	265.3	1.9	7
569	229.8	...	228.3	...	254.6	259.1	...	...	247.1	13.1	4
572	255.7	246.8	249.3	251.0	246.6	245.1	241.8	250.3	249.4	4.1	8
578	264.5	272.5	265.9	273.2	277.7	276.4	277.1	280.6	274.5	4.9	8
590	...	266.5	262.0	263.3	248.8	249.0	249.0	253.7	254.1	6.2	7
593	292.6	291.3	292.9	281.3	289.6	286.5	...	294.9	291.5	3.7	7
594	...	...	...	269.9	269.7	264.0	...	...	268.0	2.7	3
598	...	...	...	263.8	256.9	258.3	...	...	259.4	3.0	3
607	256.4	251.8	267.7	259.1	254.9	261.0	252.6	262.1	258.8	4.5	8
616	231.3	237.6	237.4	243.4	213.1	215.2	220.5	225.6	227.4	10.7	8
622	298.6	277.7	282.2	267.6	264.6	258.6	255.9	273.9	275.8	14.5	8
623	266.7	268.3	...	267.8	266.4	267.8	270.1	271.5	268.5	1.9	7
625	306.7	316.9	...	302.8	299.5	...	...	324.5	310.7	9.2	5
627	270.0	265.3	270.5	...	267.3	269.5	258.8	270.8	268.8	2.9	7
630	292.9	288.1	289.3	273.4	273.5	278.0	279.8	301.8	285.6	10.7	8
639	277.4	270.2	269.6	267.1	264.0	274.4	253.7	268.4	269.5	5.8	8
650	288.0	287.7	285.7	283.3	282.8	282.7	283.0	290.2	286.2	3.0	8
666	255.5	256.8	258.0	255.4	252.4	253.4	252.5	257.8	255.5	2.1	8
668	271.6	266.2	267.2	269.0	266.9	271.8	266.3	271.3	269.2	2.3	8
672	...	278.0	279.0	274.1	280.2	280.5	279.2	284.4	279.5	3.2	7
673	278.8	275.7	275.2	277.1	274.6	277.5	277.9	278.7	277.1	1.5	8
681	243.8	280.1	275.4	280.1	266.7	...	...	268.2	264.0	14.5	6
690	252.5	283.0	270.3	269.4	283.9	300.8	268.2	280.3	272.7	14.7	8
692	269.1	267.5	274.6	272.3	271.1	271.4	277.3	269.6	271.2	2.5	8
696	261.0	265.9	263.7	265.8	265.3	266.5	267.2	269.1	265.8	2.3	8
707	277.3	276.9	276.1	276.0	271.5	275.5	272.1	274.8	275.0	2.0	8
711	235.8	253.7	258.0	254.5	250.0	234.0	235.2	245.8	244.4	8.7	8
712	249.2	240.2	...	274.0	276.9	246.8	259.3	252.5	255.1	10.9	7
714	279.4	285.1	283.0	284.9	283.3	284.2	281.6	285.6	283.4	1.9	8
725	286.1	285.9	286.3	285.9	283.3	282.3	284.5	287.8	285.3	1.8	8
727	274.7	275.7	266.5	274.4	...	...	...	271.4	272.9	3.0	5
728	256.4	267.7	252.6	266.3	260.0	284.5	260.6	275.6	265.8	9.6	8
729	254.4	261.1	245.9	268.2	281.4	272.4	279.8	277.3	268.6	10.9	8
732	264.1	268.0	267.5	269.0	267.1	267.9	267.7	266.7	267.3	1.4	8
735	267.0	275.7	271.2	261.9	...	...	...	...	268.9	4.9	4
740	265.6	271.3	270.0	266.2	265.8	266.3	266.7	269.6	267.3	1.9	8
745	279.4	274.4	271.6	283.2	271.5	271.6	270.1	277.5	275.7	3.7	8
748	258.3	259.6	261.0	264.4	258.2	265.5	267.5	256.4	260.4	3.6	8
753	267.9	278.1	264.5	269.2	265.8	271.3	261.5	273.7	269.6	4.2	8
756	261.6	273.1	294.0	289.8	288.8	299.6	258.4	286.2	281.6	13.5	8
762	276.1	253.0	260.3	259.1	...	...	...	242.8	259.0	12.6	5
772	244.5	254.1	...	...	...	...	...	259.5	253.7	6.1	3
795	266.5	...	270.7	257.2	284.4	262.2	...	276.9	270.1	9.0	6

Table A.1. continued.

VFTS	He I$_{\lambda4121}$	C II$_{\lambda4267}$	He I$_{\lambda4438}$	Si III$_{\lambda4553}$ (LR02)	Si III$_{\lambda4553}$ (LR03)	Si III$_{\lambda4568}$	Si III$_{\lambda4575}$	He I$_{\lambda4713}$	v_r	σ	n
801	283.8	284.9	292.6	272.1	...	...	...	265.6	278.0	9.7	5
807	292.4	...	287.3	288.9	290.2	290.9	...	292.2	291.0	1.7	6
811	278.2	276.2	276.3	273.0	255.8	301.8	...	280.3	277.4	10.7	7
814	262.2	278.6	274.5	289.2	...	...	...	267.2	271.6	9.1	5
817	234.7	269.9	245.0	261.1	249.6	255.1	264.6	...	251.9	11.8	7
823	235.0	276.0	...	...	...	...	...	248.5	248.0	13.1	4
829	...	267.4	261.4	259.9	256.5	266.5	249.8	263.1	261.4	4.9	7
831	223.6	211.0	203.4	206.8	202.6	206.7	215.6	210.5	210.4	6.2	8
835	257.0	252.5	254.3	250.2	249.7	255.2	251.7	246.8	251.9	3.4	8
841	260.2	258.6	253.7	255.9	253.9	257.7	263.8	260.3	258.0	3.0	8
845	259.5	258.9	259.6	259.6	257.9	259.9	260.9	262.6	259.9	1.4	8
851	229.5	228.7	229.4	...	...	229.8	...	229.5	229.4	0.3	5
855	246.5	251.4	249.6	246.4	243.1	246.3	248.8	252.4	248.8	3.0	8
860	255.6	252.0	249.4	256.6	256.6	250.9	243.8	250.7	252.6	3.0	8
864	278.2	275.3	271.0	271.8	279.0	281.0	...	285.0	278.2	4.6	7
866	258.6	268.5	260.9	255.5	255.5	267.3	277.5	261.6	261.8	5.7	8
867	271.4	275.6	274.4	275.3	275.1	275.0	278.8	280.5	275.7	2.7	8
868	264.6	258.2	261.6	260.1	259.8	264.3	257.7	262.5	261.5	2.3	8
872	276.3	280.1	289.9	287.6	281.9	291.4	...	293.7	285.5	6.9	7
879	281.2	277.2	277.9	...	264.8	...	...	273.6	275.7	4.9	5
881	283.3	282.9	282.6	281.7	281.8	282.5	281.7	285.9	283.0	1.5	8
885	270.1	266.3	250.3	265.3	...	262.9	260.5	263.5	264.0	5.4	7
886	253.9	264.5	255.5	260.0	263.9	248.3	253.0	263.5	258.4	5.5	8

Table A.2. Line-by-line radial-velocity estimates for single stars using the Set 2 absorption lines.

VFTS	He I$_{\lambda 4009}$	He I$_{\lambda 4144}$	He I$_{\lambda 4388}$	He I$_{\lambda 4713}$	He I$_{\lambda 4922}$	v_r	σ	n
001	287.9	279.4	283.3	...	276.5	282.1	4.2	4
004	299.2	293.7	280.1	281.2	269.0	283.1	10.8	5
005	281.7	284.0	285.6	282.0	278.4	282.6	2.6	5
007	282.1	282.6	279.2	...	...	281.1	1.6	3
008	282.6	266.1	276.2	...	264.5	271.3	6.9	4
012	...	306.2	310.8	295.5	307.2	306.1	4.9	4
013	290.5	295.5	284.5	297.1	291.3	290.9	4.3	5
020	254.5	271.9	272.9	...	235.3	258.8	16.3	4
036	244.0	273.4	289.4	...	...	270.8	18.4	3
038	274.3	278.4	272.5	279.6	283.0	278.0	4.1	5
040	303.5	273.7	297.8	...	...	291.4	12.6	3
043	271.4	260.1	259.7	...	264.9	263.6	4.4	4
048	274.3	278.9	273.8	...	269.6	274.1	3.3	4
054	246.8	283.3	289.0	266.5	242.6	265.7	19.9	5
066	289.9	274.1	282.7	242.3	254.1	272.9	13.6	5
068	297.9	273.7	243.2	...	232.5	254.8	24.0	4
070	302.7	286.2	280.6	291.9	312.1	294.7	12.5	5
071	265.6	274.1	270.9	...	263.5	268.4	4.3	4
078	278.7	285.7	279.0	289.0	285.2	283.1	3.7	5
080	291.7	289.7	279.2	285.4	279.7	284.1	5.1	5
083	290.2	290.5	282.8	...	...	287.3	3.7	3
084	284.0	276.3	273.5	277.4	273.2	276.2	3.8	5
085	284.5	289.9	281.0	287.3	...	285.3	3.6	4
088	284.2	283.1	293.4	...	272.7	284.0	7.4	4
100	255.2	258.1	258.5	...	...	257.6	1.4	3
101	279.5	280.1	269.5	...	281.2	277.3	4.8	4
104	267.5	277.1	268.1	280.3	268.5	271.2	4.7	5
109	283.9	293.3	283.5	...	278.2	284.1	5.6	4
122	...	259.8	281.2	...	238.2	260.7	17.6	3
127	235.5	249.4	242.7	...	...	243.3	5.5	3
128	294.5	279.5	272.9	...	268.7	277.4	8.7	4
134	253.7	256.2	274.1	...	...	262.8	9.4	3
137	288.9	279.7	284.3	...	284.2	284.0	3.1	4
141	271.3	284.4	285.2	287.3	278.2	281.4	5.2	5
148	258.0	268.9	257.1	289.0	263.8	264.5	8.8	5
149	259.7	287.0	282.1	265.1	270.3	274.6	9.6	5
156	272.0	269.0	308.9	...	...	283.8	18.3	3
158	264.7	276.4	310.1	...	...	285.7	19.3	3
166	275.3	267.0	280.4	...	...	274.4	5.6	3
167	275.4	290.6	285.1	290.2	289.8	286.9	5.0	5
181	267.4	271.9	273.8	...	297.4	278.9	11.9	4
187	284.1	294.1	270.7	...	279.1	280.8	8.5	4
188	312.8	284.3	280.9	269.1	268.6	281.7	14.8	5
194	270.3	275.7	294.8	288.8	259.2	277.9	13.0	5
196	264.5	267.1	278.4	283.0	...	271.9	7.1	4
201	290.2	293.4	276.8	...	...	284.9	7.8	3

Notes. Column entries are: (1) VFTS identifier; (2−6) estimated radial velocity from each line; (7) weighted mean velocity for each star (v_r, from Eq. (1)); (8) standard deviation (σ, from Eq. (2))); (9) number of lines (n) used in calculation of v_r and σ.

Table A.2. continued.

VFTS	He I$_{\lambda4009}$	He I$_{\lambda4144}$	He I$_{\lambda4388}$	He I$_{\lambda4713}$	He I$_{\lambda4922}$	v_r	σ	n
203	278.5	272.8	275.7	251.7	272.7	272.8	6.8	5
205	286.0	278.1	279.6	280.4	273.9	278.7	3.7	5
207	285.8	287.4	283.2	265.9	265.0	277.9	9.7	5
210	286.3	296.1	289.4	282.6	292.6	290.5	4.3	5
212	284.6	288.0	284.1	292.4	285.5	286.2	2.5	5
219	278.4	298.5	270.2	...	...	282.5	12.6	3
221	249.6	266.9	263.3	276.7	254.6	261.4	8.2	5
224	235.1	258.4	299.2	...	...	263.9	25.8	3
228	273.9	285.7	279.2	297.2	277.9	281.2	6.5	5
229	256.5	283.6	276.4	...	...	272.8	11.0	3
230	282.1	286.4	271.3	267.4	285.7	279.7	7.5	5
233	257.3	251.1	256.3	...	227.9	248.2	11.9	4
234	244.4	256.9	247.5	262.3	229.9	247.0	10.3	5
238	254.8	292.5	269.4	261.7	258.9	268.5	13.5	5
239	267.2	279.2	282.1	...	268.4	274.7	6.5	4
247	293.9	289.5	291.6	304.5	296.5	293.6	4.1	5
254	251.6	256.3	252.2	...	240.8	250.7	5.6	4
263	250.0	267.8	291.8	...	...	270.1	16.8	3
274	278.8	256.3	251.3	...	235.6	252.9	14.1	4
279	242.1	266.4	278.5	256.7	...	262.6	14.1	4
282	241.5	253.5	242.3	265.8	289.3	260.5	19.7	5
283	260.0	248.2	257.3	241.7	248.6	252.1	6.0	5
286	277.0	279.6	272.9	...	284.5	278.4	4.4	4
287	282.5	254.0	262.4	...	...	264.7	11.4	3
288	264.2	246.4	261.0	269.5	257.6	258.0	7.2	5
292	256.9	261.9	264.5	275.3	264.7	263.6	4.9	5
295	...	295.8	300.2	...	322.7	307.7	12.0	3
298	334.0	327.3	336.2	...	...	332.1	4.0	3
300	280.6	259.7	285.5	294.4	268.0	276.7	12.1	5
301	267.7	258.9	280.9	262.6	...	268.4	9.0	4
309	288.2	281.0	282.4	294.1	269.2	281.8	7.6	5
320	290.0	265.7	318.1	...	...	291.3	22.1	3
321	263.4	251.2	262.3	...	...	258.6	5.6	3
322	284.0	262.5	277.9	297.7	...	276.9	11.1	4
326	236.0	244.0	256.1	...	258.9	250.1	8.8	4
328	297.8	320.2	307.5	328.2	316.5	313.7	8.8	5
330	261.1	269.3	272.9	272.3	264.7	267.7	4.4	5
335	250.2	247.2	251.8	245.2	247.1	248.7	2.2	5
340	254.2	265.0	258.9	...	221.4	251.7	16.2	4
343	238.1	254.0	241.0	...	227.7	240.5	9.3	4
348	261.8	267.5	272.0	...	...	267.8	4.0	3
349	258.2	280.0	272.3	259.2	268.4	269.4	7.7	5
354	250.1	265.1	259.5	...	234.8	250.7	12.3	4
358	148.3	165.1	175.4	...	...	164.7	10.7	3
365	273.1	266.0	262.9	301.9	265.4	270.0	10.9	5
367	275.8	271.7	272.7	268.6	259.1	269.4	6.0	5
368	249.2	215.7	227.1	...	...	229.6	12.4	3
373	262.5	274.2	275.1	...	...	271.4	5.4	3

Table A.2. continued.

VFTS	He I$_{\lambda 4009}$	He I$_{\lambda 4144}$	He I$_{\lambda 4388}$	He I$_{\lambda 4713}$	He I$_{\lambda 4922}$	v_r	σ	n
387	246.6	294.3	308.0	...	...	286.3	24.2	3
394	247.1	245.9	228.1	...	...	239.4	8.9	3
397	279.4	259.1	290.2	...	...	276.7	13.2	3
401	262.1	246.4	301.2	...	...	269.7	23.3	3
403	250.9	247.6	255.7	...	...	251.2	3.4	3
414	285.2	261.9	254.3	...	...	264.2	11.6	3
421	273.0	264.5	261.1	...	...	265.8	4.8	3
425	296.2	260.5	279.4	...	...	276.2	13.6	3
428	277.0	284.6	297.9	...	...	286.5	8.5	3
447	264.6	272.5	266.6	260.3	256.5	264.6	5.8	5
448	229.0	281.0	269.0	...	256.9	267.0	o9.2	4
449	276.0	269.6	275.1	...	246.7	265.8	12.3	4
452	262.9	261.5	258.0	258.9	252.7	258.6	3.6	5
453	263.2	266.0	263.6	...	...	264.4	1.3	3
461	252.8	283.9	279.7	...	276.7	275.2	10.9	4
463	276.8	286.0	275.9	...	...	279.8	4.7	3
467	331.7	277.5	355.6	...	...	322.3	30.2	3
473	225.4	264.1	276.4	...	254.5	257.1	19.3	4
474	244.9	248.8	274.3	...	276.2	264.1	14.0	4
485	282.5	269.7	275.7	...	...	275.4	4.8	3
486	276.4	264.0	300.7	...	...	280.0	15.6	3
489	282.6	247.2	277.2	...	...	268.9	15.1	3
495	277.7	273.4	280.7	254.9	265.6	272.6	7.8	5
499	308.2	288.8	284.5	...	...	293.1	10.1	3
523	281.8	269.5	264.7	...	...	271.0	6.9	3
530	313.5	276.0	289.2	...	...	290.3	14.2	3
539	294.8	258.7	269.2	...	...	271.5	11.4	3
543	249.6	257.5	251.2	...	...	253.1	3.3	3
547	265.9	259.6	240.9	...	...	255.9	10.3	3
551	294.9	282.5	277.6	...	...	284.7	7.1	3
554	266.9	274.9	272.5	...	...	272.1	2.9	3
556	251.9	268.7	268.4	...	245.0	260.5	10.2	4
563	...	247.3	278.6	...	271.2	267.5	12.4	3
567	283.5	277.7	279.4	...	250.2	272.1	13.3	4
568	...	280.9	287.8	...	270.3	280.3	6.9	3
570	253.9	261.7	322.8	...	...	279.4	30.4	3
574	268.2	267.9	269.5	240.6	265.3	264.7	8.4	5
580	279.1	285.7	284.0	...	...	283.3	2.6	3
584	250.8	248.3	261.3	...	...	253.3	5.7	3
592	234.4	268.0	261.2	...	...	257.4	13.2	3
600	246.4	277.0	290.7	...	297.9	279.8	18.4	4
602	300.0	299.4	302.9	...	...	301.0	1.6	3
605	316.7	293.6	287.9	...	243.2	278.6	26.3	4
610	245.3	249.6	254.4	...	232.8	245.8	8.4	4
615	246.9	275.6	254.6	...	266.9	262.7	10.0	4
620	286.9	276.1	292.2	279.0	261.0	278.0	11.8	5
624	260.9	266.9	259.9	...	271.9	265.3	4.9	4
629	280.4	237.7	278.9	...	...	265.1	19.9	3
632	285.4	281.4	282.9	312.9	274.7	284.7	11.1	5

Table A.2. continued.

VFTS	He I$_{\lambda 4009}$	He I$_{\lambda 4144}$	He I$_{\lambda 4388}$	He I$_{\lambda 4713}$	He I$_{\lambda 4922}$	v_r	σ	n
633	274.8	277.2	279.4	281.3	261.0	274.0	7.2	5
636	...	237.8	248.7	...	237.7	241.5	5.2	3
640	264.9	252.4	253.3	262.1	253.4	256.0	5.0	5
643	247.3	252.5	242.6	...	266.3	250.9	8.2	4
644	216.8	266.9	250.1	...	...	248.6	20.2	3
646	255.4	261.5	270.1	...	264.6	263.9	4.8	4
659	265.5	264.3	265.7	252.2	269.0	264.9	4.6	5
660	...	278.3	260.2	...	242.0	257.1	14.7	3
670	285.5	269.7	278.7	304.1	305.2	286.1	13.8	5
671	251.3	274.6	254.4	...	237.3	255.3	13.3	4
676	295.0	249.7	277.5	...	...	272.1	18.7	3
678	265.7	266.0	287.6	...	258.9	270.2	11.2	4
679	262.9	268.2	263.8	265.8	265.9	265.5	1.8	5
683	261.5	261.9	263.6	...	299.4	271.1	15.7	4
684	...	270.2	269.4	...	298.0	278.6	13.1	3
685	229.7	225.1	278.5	253.4	...	243.4	22.5	4
699	280.4	249.5	267.5	...	...	264.4	12.0	3
701	281.6	263.6	256.2	...	...	266.6	10.1	3
709	258.1	271.6	259.3	...	272.2	265.5	6.5	4
720	294.0	301.0	292.4	306.1	302.0	298.4	4.8	5
726	267.5	240.7	261.4	...	239.2	249.7	12.1	4
734	247.7	269.1	265.7	...	270.9	263.7	8.9	4
738	272.6	273.8	302.4	...	...	284.4	14.1	3
741	269.1	270.5	255.5	284.1	248.6	263.2	10.9	5
747	274.6	269.9	271.7	266.7	267.9	270.2	2.5	5
749	257.2	274.6	258.0	276.7	264.0	264.8	7.2	5
754	234.5	244.0	242.9	244.5	237.2	240.2	4.0	5
757	264.9	275.3	271.4	285.8	279.5	273.4	6.3	5
780	265.4	245.0	242.3	238.7	230.7	243.4	11.4	5
781	268.0	260.9	287.2	...	...	272.7	11.5	3
786	283.0	290.2	264.2	...	262.0	274.0	12.0	4
789	245.2	283.6	261.0	...	...	263.6	15.5	3
794	267.8	271.6	294.8	...	...	278.9	12.1	3
796	274.7	288.0	290.7	...	...	284.9	6.9	3
798	279.1	254.3	250.4	245.5	219.1	247.1	19.5	5
800	277.7	247.2	286.3	...	...	268.9	17.2	3
804	...	266.1	260.4	...	245.3	256.5	9.0	3
813	271.1	271.8	268.5	...	286.3	274.5	7.1	4
815	252.1	259.9	248.9	266.3	257.4	255.7	5.4	5
823	259.8	253.1	...	255.9	272.1	262.0	8.2	4
824	223.0	258.8	248.9	249.2	250.1	245.9	12.4	5
825	...	244.1	241.8	...	277.1	252.9	15.6	3
826	241.6	243.1	256.5	239.5	230.8	242.8	9.0	5
832	259.6	262.4	258.5	289.5	262.9	263.6	8.5	5
833	286.6	277.0	276.4	...	268.5	277.0	5.9	4
836	252.7	251.8	255.1	...	...	253.3	1.4	3
838	270.3	260.2	258.2	...	265.0	263.4	4.5	4
840	246.9	225.1	244.7	...	234.1	236.7	8.9	4
842	192.8	260.6	277.9	210.8	...	244.8	34.7	4

Table A.2. continued.

VFTS	He I$_{\lambda 4009}$	He I$_{\lambda 4144}$	He I$_{\lambda 4388}$	He I$_{\lambda 4713}$	He I$_{\lambda 4922}$	v_r	σ	n
843	295.3	281.0	275.2	...	269.0	277.9	8.8	4
846	...	260.4	262.7	...	252.7	258.4	4.4	3
848	242.5	246.4	249.9	257.2	...	247.7	4.6	4
853	237.0	264.5	272.8	...	...	258.9	15.1	3
857	253.6	256.7	260.5	257.3	250.3	255.4	3.8	5
869	298.0	283.1	283.1	...	294.0	288.8	6.4	4
875	245.8	242.8	259.1	...	261.7	252.7	8.3	4
876	254.1	261.1	235.9	...	254.4	251.0	9.5	4
880	...	285.1	280.6	...	242.4	270.4	18.7	3
882	280.1	296.1	287.0	...	271.2	283.3	9.4	4
889	284.5	255.1	265.9	...	251.8	263.1	12.1	4

Table A.3. Line-by-line radial-velocity estimates for single-lined binaries using absorption lines in the LR02 observations.

VFTS	MJD	He I$_{\lambda4009}$	He I$_{\lambda4144}$	He I$_{\lambda4169}$	C II$_{\lambda4267}$	He I$_{\lambda4388}$	He I$_{\lambda4438}$	Si III$_{\lambda4553}$	$v_{\rm single}$	σ	n	$v_{\rm r}$	$\delta v_{\rm r\,max}$
009	54 817	302.0	293.5	…	293.8	288.7	…	291.5	293.6	4.8	5	293.2 ± 21.6	52.6
015	54 817	289.3	310.7	…	…	309.9	…	…	305.3	9.0	3	278.0 ± 30.5	65.7
017	54 828	250.3	261.8	…	…	247.8	…	…	253.3	6.3	3	280.9 ± 31.0	72.1
018	54 860	292.8	295.5	…	288.8	295.6	287.7	288.5	292.9	3.2	6	279.2 ± 11.9	21.4
025	54 828	300.0	308.3	…	…	299.0	…	…	302.2	4.1	3	290.3 ± 11.3	28.4
027	54 748	327.1	335.3	340.5	347.0	329.8	…	374.6	343.3	18.0	6	273.1 ± 42.5	111.4
033	54 748	255.2	252.5	…	…	263.7	…	…	257.5	4.9	3	270.2 ± 22.8	51.2
037	54 828	297.7	288.2	…	…	303.3	…	…	297.0	6.1	3	299.4 ± 18.4	56.3
041	54 748	295.9	297.2	303.5	294.2	285.9	299.9	318.0	297.7	9.3	7	287.0 ± 19.0	40.1
097	54 748	…	291.6	…	…	303.6	…	318.1	308.7	10.6	3	296.7 ± 11.5	23.8
106	54 822	290.8	289.2	…	…	282.9	…	…	287.0	3.5	3	281.8 ± 13.3	32.4
107	54 822	289.0	282.0	…	…	281.2	…	…	283.2	3.0	3	294.5 ± 23.7	56.5
118	54 824	272.8	281.7	294.7	281.6	273.4	286.2	286.0	279.2	6.4	7	302.2 ± 15.9	39.7
133	54 824	294.8	302.8	…	292.5	299.2	…	290.8	298.2	4.0	5	293.5 ± 15.2	38.7
135	54 817	257.9	263.1	…	…	280.6	…	…	269.0	9.9	3	270.9 ± 52.5	136.6
144	54 815	277.8	274.6	…	270.6	273.2	…	…	274.3	2.2	4	281.8 ± 14.5	34.2
146	54 748	238.1	270.0	…	…	256.5	…	…	255.4	12.8	3	259.6 ± 12.6	34.0
157	54 828	256.4	243.8	…	…	290.5	…	…	266.5	20.7	3	284.0 ± 24.4	59.7
162	54 815	302.1	285.0	…	297.5	292.9	290.9	300.8	293.7	6.1	6	283.7 ± 14.8	32.5
179	54 824	324.7	302.2	304.1	296.8	299.1	294.3	291.7	303.1	10.1	7	294.5 ± 6.4	16.9
189	54 824	194.6	180.5	…	…	172.4	…	…	181.5	9.0	3	274.0 ± 69.9	185.9
195	54 824	277.1	281.5	…	275.5	279.6	283.7	270.7	279.0	3.7	6	268.1 ± 12.9	28.7
199	54 828	261.5	280.7	…	…	282.9	…	…	275.9	9.4	3	…	…
204	54 815	252.5	254.7	258.2	241.0	247.3	249.7	241.8	249.7	5.0	7	254.9 ± 12.7	31.0
206	54 815	259.2	283.1	…	…	266.4	291.7	…	272.1	11.5	4	257.3 ± 36.8	84.5
211	54 817	301.0	280.3	…	…	279.2	…	…	284.7	9.1	3	272.0 ± 13.2	33.6
213	54 804	270.7	273.4	264.4	279.9	273.2	…	268.5	272.4	3.3	6	276.4 ± 12.8	30.0
215	54 822	342.7	358.3	…	364.9	353.5	338.3	…	352.6	7.6	5	287.5 ± 63.0	121.7
218	54 815	265.4	264.9	233.0	255.6	253.6	253.1	247.3	257.6	8.5	7	249.2 ± 7.9	20.0
225	54 815	272.8	265.9	272.6	264.3	259.8	263.8	264.6	265.4	4.5	7	289.2 ± 15.8	32.0
227	54 804	284.9	274.8	…	…	280.4	270.8	267.9	277.4	5.2	5	277.4 ± 9.1	23.1
240	54 809	112.2	130.1	…	…	125.3	…	…	123.2	7.0	3	224.2 ± 52.6	152.1
246	54 809	269.6	254.3	…	…	239.3	…	279.2	255.1	14.5	4	275.8 ± 28.8	63.2
248	54 824	249.6	313.5	…	…	308.1	…	…	296.7	25.7	3	297.6 ± 35.8	89.5
255	54 804	276.3	255.7	…	…	238.6	…	…	257.7	14.8	3	268.5 ± 65.4	163.8
257	54 817	285.8	252.7	272.2	…	254.9	…	256.4	263.4	13.3	5	269.2 ± 11.9	27.8
278	54 828	291.6	269.0	284.4	270.6	269.0	…	…	275.5	9.5	5	270.8 ± 12.8	33.0
291	54 748	205.3	206.1	201.1	200.5	200.7	187.5	…	201.9	5.3	6	234.7 ± 46.1	103.5
299	54 822	346.1	357.3	374.6	362.5	357.5	367.1	355.6	357.8	7.9	7	288.9 ± 45.8	107.8
305	54 817	304.1	297.7	309.2	276.2	292.1	305.8	…	297.2	9.0	6	321.7 ± 50.4	123.3
324	54 815	296.0	297.7	317.0	301.5	295.7	307.1	305.6	299.7	5.9	7	274.6 ± 25.1	64.3
325	54 748	261.6	278.9	…	…	279.6	…	277.5	275.0	7.3	4	287.4 ± 46.0	118.0
334	54 817	244.2	273.3	…	233.2	281.6	…	309.6	268.7	21.5	5	266.2 ± 17.3	40.8
336	54 824	280.4	261.5	…	…	267.7	…	252.4	267.4	8.3	4	266.7 ± 14.7	36.7
337	54 809	287.4	297.1	…	…	260.4	…	…	282.2	15.6	3	278.6 ± 11.1	31.8
342	54 794	299.8	313.4	318.7	302.5	304.7	309.8	300.9	306.7	5.9	7	292.2 ± 43.4	103.6

Notes. Column entries are: (1) VFTS identifier; (2) Modified Julian Date (MJD) of the co-added observations used for these measurements (see Appendix of Paper I for details of exposures); (3−9) estimated radial velocity from each line; (10) weighted mean (single-epoch) velocity for each star ($v_{\rm single}$, from Eq. (1)); (11) standard deviation (σ, from Eq. (2)); (12) number of lines (n) used in calculation of $v_{\rm single}$ and σ; (13) estimated mean $v_{\rm r}$ (and standard deviation) calculated from the multi-epoch measurements from Dunstall et al. (in prep.); (14) maximum difference ($\delta v_{\rm r\,max}$) in the radial velocity estimates between the available epochs.

Table A.3. continued.

VFTS	MJD	He I$_{\lambda4009}$	He I$_{\lambda4144}$	He I$_{\lambda4169}$	C II$_{\lambda4267}$	He I$_{\lambda4388}$	He I$_{\lambda4438}$	Si III$_{\lambda4553}$	$v_{\rm single}$	σ	n	$v_{\rm r}$	$\delta v_{\rm r\,max}$
351	54 794	231.6	238.3	237.8	227.6	225.4	231.4	226.3	230.8	5.3	7	246.8 ± 24.9	57.8
359	54 824	295.8	295.4	301.1	…	286.6	276.5	275.3	288.6	8.6	6	295.0 ± 10.5	25.6
364	54 822	250.8	224.4	247.7	232.6	227.9	202.2	…	232.1	13.5	6	266.6 ± 29.9	67.5
374	54 809	293.2	248.9	…	…	236.6	…	…	254.8	22.2	3	291.5 ± 21.7	65.5
375	54 809	280.4	320.3	…	…	324.0	…	…	311.6	18.2	3	296.4 ± 22.1	58.5
383	54 809	315.9	325.0	…	…	319.9	…	…	320.5	3.7	3	224.5 ± 64.2	168.0
388	54 824	270.7	260.9	…	…	255.9	274.5	254.4	261.0	6.8	5	276.4 ± 9.5	25.4
396	54 809	224.2	281.6	…	…	257.4	…	…	258.0	21.5	3	270.9 ± 17.7	38.9
430	54 824	193.2	207.7	…	…	211.7	…	216.0	208.1	8.0	4	218.3 ± 48.7	120.8
459	54 828	265.7	249.9	…	…	247.8	…	…	252.9	7.3	3	260.5 ± 10.9	29.1
496	54 794	264.4	274.8	…	…	293.9	…	…	278.6	12.2	3	279.9 ± 14.2	35.5
501	54 815	…	303.9	327.9	…	328.5	313.5	297.8	317.0	12.7	5	287.2 ± 68.8	141.4
520	54 822	280.6	274.4	…	254.2	251.5	246.6	263.8	262.7	12.3	6	278.2 ± 73.5	180.0
525	54 748	299.7	293.9	304.2	296.9	289.0	291.0	288.9	293.0	4.8	7	289.6 ± 9.5	25.4
534	54 828	275.1	292.4	270.1	…	281.3	275.4	…	277.9	6.3	5	278.2 ± 23.1	58.7
548	54 822	262.4	292.5	…	…	299.4	…	295.7	288.4	14.4	4	279.9 ± 8.5	20.7
575	54 828	229.8	228.6	232.3	225.9	224.9	219.1	…	226.9	3.4	6	263.4 ± 24.9	55.5
576	54 815	285.4	287.6	288.5	282.1	284.9	274.9	289.8	285.7	3.8	7	262.0 ± 34.9	74.6
589	54 794	…	…	223.8	204.8	201.3	208.8	206.7	205.8	6.3	5	314.5 ± 94.0	178.7
591	54 804	285.6	288.1	285.8	294.3	286.9	278.7	…	286.8	2.8	6	277.7 ± 8.8	21.3
606	54 828	255.1	264.2	…	264.0	270.4	266.7	286.5	266.7	8.0	6	265.6 ± 10.3	28.8
628	54 824	236.6	265.7	…	…	263.7	…	…	257.9	11.9	3	250.8 ± 62.7	152.7
637	54 809	274.1	235.3	…	…	237.1	…	…	246.0	16.5	3	299.3 ± 32.3	103.1
662	54 804	235.9	287.1	…	…	253.2	…	…	256.3	20.3	3	251.3 ± 39.1	100.8
665	54 804	264.5	275.7	267.4	…	265.4	264.1	264.5	267.7	4.5	6	274.2 ± 16.1	37.2
675	54 748	260.0	267.4	273.9	261.2	262.6	265.0	270.7	266.0	4.5	7	276.7 ± 23.8	59.5
686	54 804	297.8	292.8	311.1	298.1	293.9	302.7	303.8	298.2	5.4	7	276.8 ± 38.9	90.0
687	54 748	316.7	312.1	285.6	319.0	315.2	293.2	321.6	314.0	8.8	7	295.8 ± 23.0	56.8
697	54 794	264.8	280.6	274.2	265.5	267.8	…	…	271.1	6.7	5	263.7 ± 8.3	20.8
705	54 809	168.6	183.5	…	…	172.1	…	163.7	173.8	7.0	4	268.3 ± 80.8	174.9
713	54 794	239.4	233.7	…	…	234.9	…	…	235.6	2.3	3	250.6 ± 38.7	100.9
715	54 809	262.6	283.0	…	292.5	268.0	299.3	271.7	275.5	11.6	6	270.0 ± 22.1	53.1
718	54 828	323.0	320.8	…	…	327.8	…	…	323.9	2.9	3	306.8 ± 16.2	39.4
719	54 804	230.7	253.5	…	239.9	226.9	232.5	240.1	237.0	10.4	6	265.0 ± 18.9	52.4
723	54 794	279.6	283.7	294.0	279.3	280.5	271.6	279.8	281.3	4.8	7	239.2 ± 26.3	62.1
730	54 822	326.8	333.0	…	377.0	326.4	…	…	332.1	12.6	4	326.5 ± 6.8	16.6
752	54 817	261.7	260.5	…	…	267.6	247.8	241.8	260.7	7.7	5	258.8 ± 40.3	87.4
779	54 809	248.0	248.7	244.2	246.7	245.2	249.4	250.8	247.7	2.1	7	258.9 ± 27.2	61.0
784	54 748	339.3	259.2	…	…	274.6	…	…	286.2	31.9	3	312.4 ± 27.6	70.7
788	54 824	295.6	314.4	…	…	292.9	…	308.1	302.0	9.4	4	280.7 ± 27.8	70.1
792	54 815	265.0	281.9	285.5	265.3	267.0	276.5	…	271.9	7.7	6	278.3 ± 8.0	18.0
799	54 809	281.3	276.6	281.6	270.2	263.3	271.2	265.3	271.6	7.0	7	270.7 ± 7.3	19.9
827	54 828	244.8	245.6	260.4	243.1	238.2	236.9	241.2	243.1	5.5	7	254.3 ± 14.4	34.7
834	54 809	211.0	207.1	…	219.4	219.3	…	214.9	213.8	5.0	5	240.3 ± 22.1	43.6
837	54 828	306.0	301.8	…	…	315.2	…	…	308.4	5.8	3	282.5 ± 27.0	66.0
847	54 822	317.6	299.9	…	…	300.7	…	288.6	302.0	9.6	4	298.7 ± 9.6	26.2
850	54 828	255.4	249.0	…	242.5	234.6	232.3	232.2	241.8	9.4	6	256.9 ± 11.6	27.1
874	54 828	277.5	277.4	247.9	265.2	280.4	…	283.4	274.8	9.5	6	274.9 ± 8.3	20.0
877	54 815	234.4	240.2	…	…	207.4	…	…	228.2	14.2	3	236.7 ± 11.2	26.6
883	54 828	254.6	301.7	…	…	295.5	…	…	289.9	17.3	3	…	…
888	54 815	317.6	326.7	334.2	316.7	314.2	…	330.5	321.4	7.1	6	238.3 ± 50.8	121.0
890	54 828	…	304.9	…	…	302.2	…	316.2	305.8	5.3	3	…	…
891	54 815	289.1	278.7	278.3	283.3	271.3	279.9	275.6	279.0	6.1	7	273.6 ± 8.3	20.5